NTNU
Norwegian University of
Science and Technology

An Experimental Investigation of Pore Pressure Generation in Moving Debris

Mingbo Yang

Geotechnics and Geohazards
Submission date: June 2016
Supervisor: Steinar Nordal, BAT
Co-supervisor: Vikas Thakur, BAT

Norwegian University of Science and Technology
Department of Civil and Transport Engineering

NORWEGIAN UNIVERSITY OF SCIENCE AND TECHNOLOGY

DEPARTMENT OF CIVIL AND TRANSPORT ENGINEERING`

Thesis Title: *An Experimental Investigation of Pore Pressure Generation in Moving Debris*	**Date:** 2016. 6. 17 **Number of pages (incl. appendices):** 106			
	Master Thesis	×	**Project Work**	
Name: Mingbo Yang				
Professor in charge/supervisor: Steinar Nordal				
Other external professional contacts/supervisors: Vikas Thakur				

Abstract

Debris flow is a typical type of landslide and has huge impact on human life. The moving debris in traditional numerical modeling is assumed as hydrostatic along the flow depth, which is not the actual case when the generation of excess pore pressure in the shear zone significantly influences the flow mobility. The thesis studies the excess pore pressure build-up in the shear zone of the moving debris by using a rotating drum apparatus, which can rotate itself to provide the shear rate and generate the shear stress on the basal layer of the debris material. Samples with different silt content were tested under different speeds, and the result shows the excess pore pressure build-up is highly considerable related to the fine grain content. Results were also verified by comparing with two other studies using coaxial cylinder (Kyoji Sassa & Gonghui Wang, 2003; Xiang Yu, 2015), proving the excess pore pressure in the shear zone of the moving debris is highly considerable.

Keywords:

1. rotating drum apparatus
2. moving debris
3. excess pore pressure build-up
4. fine grained content

Mingbo Yang

MASTER DEGREE THESIS

Spring 2016
Mingbo Yang

AN EXPERIMENTAL INVESTIGATION OF PORE PRESSURE GENERATION IN MOVING DEBRIS

BACKGROUND

Debris flow is a type of landslide, and it does considerable damage worldwide each year. Since 1970s, research has been focused on the moving mechanics of debris flow. In the traditional numerical modeling, the pore pressure profile of the moving debris is assumed to be hydrostatic. This is however, not true in the actual scene. In the shear zone of the moving debris, the grain size is much finer than other parts. During the motion, these fine grains can easily generate excess pore pressure. In certain conditions, the pore pressure profile can make a huge difference than the traditional assumed value. A rotating drum apparatus is therefore established to evaluate the actual pore pressure profile of the moving debris.

TASK DESCRIPTION

- Perform literature review on the basic concepts of debris flow. Pioneer physical modeling by using the rotating concept should be included.
- Develop a rotating drum apparatus for the moving debris simulation. Besides, a pore-pressure measuring system and a test program should be designed.
- Perform tests on samples of varying silt contents under increasing rotating speeds. Derive the empirical influence of the grain size distribution and rotating speed on the excess pore pressure development and dissipation.
- Evaluate the functionality of the apparatus and the representativeness of results.
- Verify the result with literature studies.
- Come up with proposals for apparatus improvement and test program for future study.

STEINAR NORDAL
Professor
Geotechnical Division, NTNU

Preface

This thesis is submitted in partial fulfillment of the requirement for Master's Degree (MSc) in Geotechnics and Geohazards at the Geotechnical Division of Civil and Transport Engineering Department, Norwegian University of Science and Technology (NTNU). It was carried out in the spring semester of 2016.

The idea for this thesis was raised by Professor Vikas Thakur which focuses on the laboratory investigation of pore pressure build-up in the basal layer of moving debris flow. It is a follow-up study of the master thesis '*Laboratory Investigation of the Pore Pressure Built-Up in Moving Debris*' (Xiang Yu, 2015) and the project thesis '*Pore water pressure distribution in the shear zone of debris flow*' (Mingbo Yang, 2015).

This study is supported by the Ferry free E-39 project of Norwegian Public Roads Administration. The main content of the thesis is contributed to the journal *Landslides*.

Mingbo Yang
Trondheim, June 2016

Acknowledgement

I wish to express my gratitude to my supervisor, Professor Vikas Thakur, for his patient guidance, enthusiastic encouragement and important feedback through the thesis.

I highly appreciate the inspiring discussion with Professor Steinar Nordal, Petter Fornes, Professor Gudmund Eiksund and Ashenafi Lulseged at the Geotechnical Division, NTNU. My thanks also go to Professor Gustav Grimstad who offered brilliant advice on my thesis presentation, and Djamalddine Boumezerane who has arranged so much for master students.

My sincere appreciation goes to Per Østensen and Frank Stæhli who have attributed a lot to my experiment apparatus. I also want to thank Helene Amundsen, Tonje Helle, Emilie Laache for all the help in the laboratory and sharing samples for my experiment.

Special thanks to my senior Xiang Yu at the Geotechnical Division, Statens Vegvesen Region Sør. Thank you for your previous effort and your advice for my topic.

I thank my colleagues and friends Anuj Magar, Amanuel Petros, Astrid Øveraas, Bigyan Sherchan, Bård Gjengstø, Egil Behrens, Helena Dang, Kjetil Kildal, Lars Botnen, Xiaoou Liu for the amazing two years we have at the Geotechnical Division, NTNU. I would like to thank my parents, my brother Chongbo Yang and my close friends Yingqi Liu, Xiang Chen and Kun Xie who has accompanied me all along this.

Summary

This thesis studies the pore pressure generation in the shear zone of moving debris by using a rotating drum apparatus. A pore pressure sensor is installed in the base of a sensor bar, and the sensor bar is inserted into the debris material for pore pressure measurement. Samples of varying percentage of silt content (0, 20%, 33%, 40%, 50%, 80% and 100%) are tested under increasing rotating speeds (0 – 80cm/s), and pore pressure is measured during and after the debris' motion. Results are analyzed in terms of floating ratio and dissipation, based on the assumption that the change of the flow depth during motion is neglectable. Analysis shows the fine-grained content is crucial to the excess pore pressure build-up, which is in coherent with two pioneer studies *(Wang and Sassa 2003, Yu 2015)*. The rotating drum apparatus is also proved to be able to provide more steady flow than the coaxial cylinder in relatively high velocity (40~80cm/s).

Contents

List of figures

List of tables

List of symbols

Roman Letters

c	Concentration of the sediment by volume
e	The shift of the center of the gravity
g	Gravity acceleration
h	Assumed flow depth
h_w	Height of static water level
k_f	The ratio between shape parameters for the sediment particle and the pore space
l	The distance to the fixed point
n	Herschel-Bulkley exponent
p_f	Reynolds stress from turbulent mixing
R	Radius of rotating drum apparatus
T	The total shear force
u	Pore pressure measured
u_s	Static water pressure
W	Weight of the apparatus
W_S	Weight of the mixture
z	Total flow depth

Greek Letters

γ_w	Unit weight of water
γ_s	Unit weight of mixture
γ_f	Floating ratio
$\dot{\gamma}$	Shearing rate
θ	Deviation angle to the center of the gravity
ρ	Density of interstitial fluid
ρ_d	Dynamic pressure due to inelastic collisions of interparticle contacts
ρ_s	Density of solid particles
ρ_m	Density of sediment
ρ_w	Hydrostatic pressure of interstitial water
σ_t	Total normal stress
τ	Shear stress
τ_y	Yield strength
φ	Internal friction angle
φ_s	Interparticle friction angle
ω	Rotational velocity

1. Introduction

1.1. Background

Debris flow is a type of landslide. The flow consists of sediments with a wide range of grain size, and it is usually triggered by intense rainfall or snow melting. Under the influence of gravity, a mature debris flow can move in a very high speed. The considerable speed together with the growing volume along the slope makes debris flow very dangerous.

Debris flow causes considerable damage worldwide. In Japan, about 90 lives a year on the average are lost by debris flows back to 1980s (Takahashi 1981). In US, debris flows occurs frequently in the mountainous regions of the central and eastern United States (Highland, Ellen et al. 1997). In Norway, the threat to the lives of human by debris flow is less significant due to the low population density in influenced areas. However, the damage on properties and infrastructures caused by debris flow is non - neglectable. Figure 1-1 shows a typical debris flow happened in Manndalen in Kåfjord in 2011. The debris flow spread to a large area, bringing huge threats to the local inhabitants and causing considerable damage on properties.

Figure 1-1 Flaumskred, Manndalen i Kåfjord, Norway 2010 (Taurisano/NVE. 2011)

With increasing frequency and intensity of the extreme rainfall and rapid snow melting, landslides hazards such as debris flow is predicted to take place more frequently (NIFS. 2014). Figure 1-2 shows the assumption of increased landslides and avalanche hazards affected by the change of the weather (NVE. 2011). To prevent the damage from the potential hazards, administrations such as Norwegian Public Roads Administration (Statens vegvesen, SVV), Norwegian Water and Energy Directorate (Norges vassdrags- og energidirektorat, NVE) and Norwegian National Rail Administration (Jernbaneverket) have started to collaborate. In 2012, a collaboration project called “NATURFARE – infrastruktur, flom og skred (NIFS)” is funded with over 42 million NOK to deal with natural hazards, and debris flow is one of the research topics of the landslides. Figure 1-2 shows a susceptibility map for debris flows (NVE. 2014). This is proposed by NVE for initial hazard evaluation. As a starting stage, the susceptible map does not provide any information about risk level in terms of probability or frequency of debris flow.

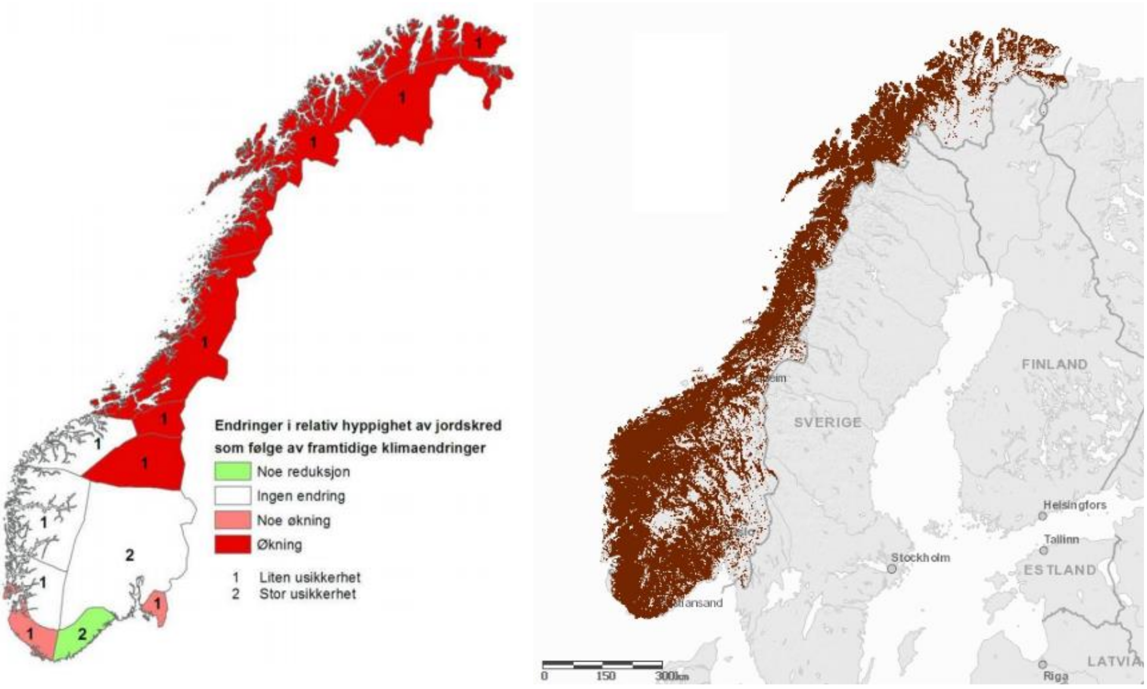

Figure 1-2 Assumption of increased landslides (NVE. 2011); Susceptibility map of debris flows (NVE. 2014)

To study the moving debris, the excess pore-pressure generation in the shear zone may be the key. Since the pore-pressure build-up contributes to the solid-fluid interaction during the motion of the debris, it dominates the physical properties such as effective normal stress and friction along the shearing interface. These physical properties further influence the mobility and stability of the flow. However, in the traditional numerical modeling of the moving debris, the pore pressure profile is assumed to be hydrostatic (Leonardi 2015). This is not true in the actual profile. In the shear zone of the moving debris, the grain size is much finer than other parts. These finer grains can easily generate excess pore pressure during the motion, and in some conditions the pore pressure profile can make a huge difference than the traditional assumed value. Figure 1-3 shows the difference. In the actual profile, the excess pore pressure is very considerable in the shear zone, which has a strong influence on the mobility of the moving debris.

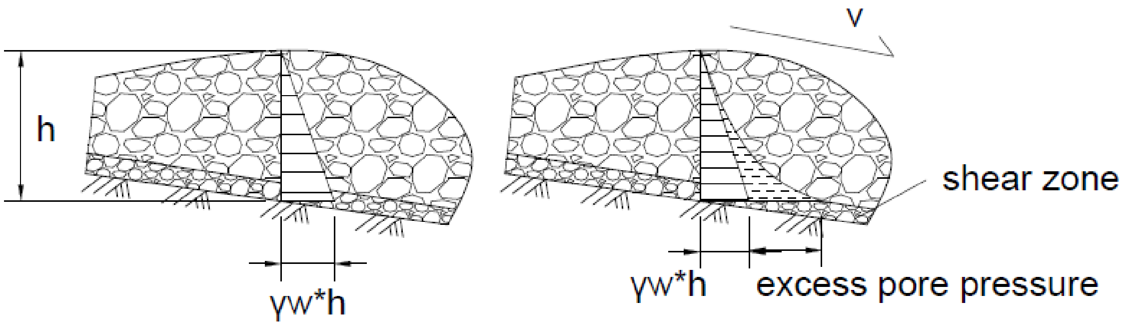

Figure 1-3 Assumed pore pressure profile (left) & Actual pore pressure profile (right)

In this thesis, a rotating drum apparatus was developed to study several factors that influence the generation of the excess pore pressure. Factors such the velocity (shear rate), grain size distribution and dissipation time of the excess pore pressure were put into discussion. Figure 1-4 shows the simple sketch of the apparatus. The rotating drum can rotate to provide different steady shear rate, and therefore generates the shear stress on the basal layer of the debris material. In the experiment, samples with different silt content were tested under different speeds. The pore pressure was recorded, and the dissipation time of the excess pore pressure was measured. Results were also compared with two other studies (Wang and Sassa 2003, Yu 2015); which performed experiments with coaxial cylinder.

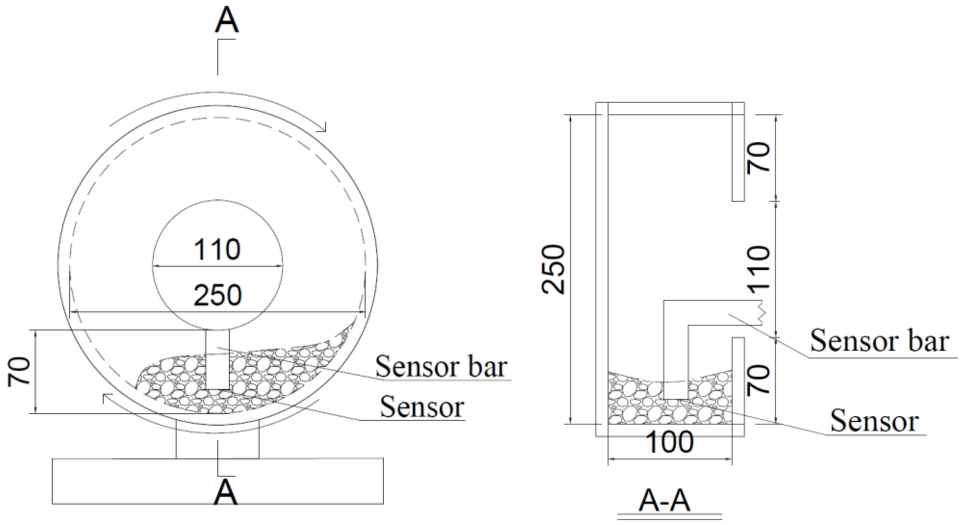

Figure 1-4 Rotating drum apparatus

Besides the rotating drum, the whole apparatus system includes the relevant motor and gear, data acquisition system, controlling program, signal amplifier and power supply. A pore pressure measurement sensor was placed in the base of the sensor bar which is installed into the cross section of the debris material.

1.2. Objective

The objective of the thesis is to study pore-pressure generation in the shear zone of the moving debris by using a rotating drum apparatus. For this purpose, a rotating drum apparatus is developed and a test program is performed. Samples of varying silt content are tested under different speeds, and pore pressure is measured during the motion and dissipation. Results are analyzed and compared with pioneer studies, proving the excess pore pressure build-up is closely related to the fine-grained content.

1.3. Scope

Chapter two introduces the basic concepts and typical physical modeling of debris flow. Basic concept such as definition, classification, sediment and composites, causes, constitutive relations are introduced. Two studies on the pore pressure generation of the moving debris by using coaxial cylinder were discussed, followed with the development of rotating drum apparatus and its modeling of granular debris flow.

Chapter three introduces the development of a rotating drum apparatus. The configuration of the apparatus and the measuring system is introduced. The methodology of the physical modeling is discussed. A test program is determined for the physical modeling with the chosen test material.

Chapter four examines the functionality of the apparatus, interprets the test result and further compares it with literature study. Floating ratio and dissipation process are analyzed, and the influence of the fine-grained content and rotating speeds are discussed.

The final chapter concludes the main outcome of the physical modeling with the rotating drum apparatus. Some recommendations for future work are also listed.

2. Literature review of debris flow

2.1. Background

The term debris flow was first introduced as a type of landslide (Stiny 1910) and the definition of debris flow has been classified and distinguished over time. Nowadays, it is widely accepted that debris flow is a gravity-driven mixture of loosen grains with considerable water moving along unstable slope or mountainsides. Debris flow is a worldwide hazard. Figure 2-1 shows the locations for which rainfall characteristic triggers shallow landslide or debris flow. The figure reveals debris flow is a great challenge not only in Norway, but also in the southern part of Europe, the western coast of United States, the whole of Japan and the southeast of China.

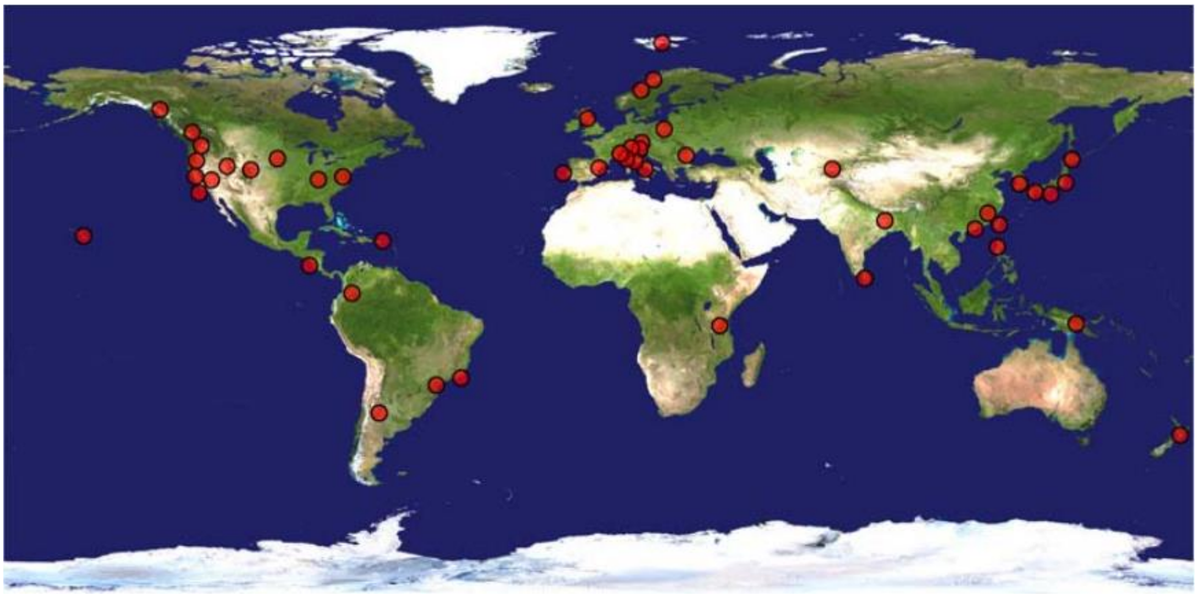

Figure 2-1 Locations for which rainfall triggered shallow landslides or debris flows (Guzzetti, Peruccacci et al. 2008)

Debris flow presents a variation of composition and kinetics depending on the topography and sediment conditions. It has a considerable volumetric sediment concentration. The moving debris flow can reach a very high speed where rainfall is intense and the slope is steep, especially with loose bulk of fragmented rock and intense water seepage. These days, numerical models are available to model the physics of debris flow. However, the accuracy of the models could be troubled by limited knowledge of soil grains properties, and therefore many debris flow hazards are still assessed in empirical methods (Iverson 2014).

2.2. Definition

Debris flow is a type of landslide. A simplified classification of landslide could be referred to Table 2-1. By having classified the type of movement and the type of the predominant composites of landslide, debris flows are defined as a flow type with the debris as the predominant composites.

Table 2-1 Simplified classification of landslide (Cruden and Varnes 1996)

Distinct Movement	Description
Fall	Detachment of soil or rock from slope along a surface on which little shear displacement takes place.
Topple	Forward rotation out of the slope of a mass of soil and rock.
Slide	The downslope movement of a soil or rock mass occurring on the failure surface with intense shear strain.
Flow	Spatially continuous movement in which shear surfaces are short lived, closely spaced and usually not preserved after the event.
Spread	An extension of a cohesive soil or rock mass with a general subsidence of the fractured cohesive material into softer underlying material.

For a broad definition of debris, it generally refers to a mixture consisting of a considerable amount of fine grained material meanwhile with at least 20% coarse material (such as gravel, boulders and even bigger) with a significant of organic objects (such as tress or logs). The grain size distribution of debris flow varies considerably from different section of its flow, and recently a study considers the grain size distribution follow a universal rule (Li, Wang et al. 2015). Debris flow shares the characteristics from both avalanche and flood that both solid and fluid forces affect the motion, which distinguishes it from similar phenomenon such as rock avalanches or sediment floods (Iverson 1997). Additionally, there are approaches defining debris flows focused on sediment concentrations, grain size distributions, flow speeds and shear strength (Beverage and Culbertson 1964, Pierson and Costa 1987). These approaches, however, do not necessarily explain the core mechanism of the debris flow that the interacting solid and fluid force distinguished it from any other types of similar flows.

Because debris flow consists of fine grained sediments and also very coarse materials, it has a relatively high percentage of sediment concentration by volume (50% could be a common value (Takahashi 2014)). The degree of the fine grained content such as silt and clay can also characterize debris flow as viscous, greatly influenced by water condition.

2.3. Composite

The composite of debris flow is a mixture of materials of high density (Nettleton, Martin et al. 2005). Figure 2-2 shows debris flow composites. These materials have a very broad range of grain size distribution, from fine materials such as clay, silt, sand and coarse materials even cobbles and boulders. Besides, a considerable quantity of water is involved, and therefore the mixtures have the viscous behavior as the debris flow flows down (Hutchinson 1988). Debris flow can be sometimes mistaken as mud flow; however, more than 50% of a debris flow is made up of large grain size while the mud flow only contains mud (a semi-liquid mixture, typically of fine particles of soils and water (Hungr, Evans et al. 2001)). In this way, mud flow can be viewed as the soil overloaded with water, and debris flow consists of other materials besides the mud with a broad range of grain size.

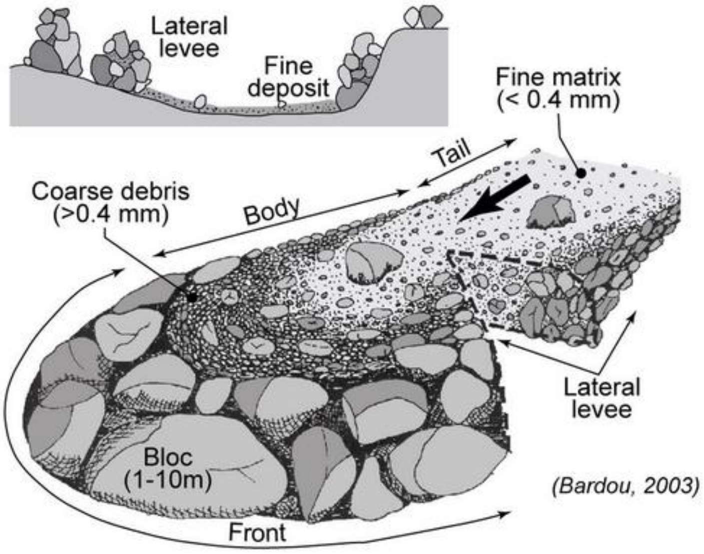

Figure 2-2 Debris flow composite (Devoli 2013)

A general structure of the moving debris is also summarized by Takahashi as Figure 2-3 (Takahashi 2009). The figure illustrates the velocity, solid concentration by grains and the excess water pressure distribution along the depth of the moving debris.

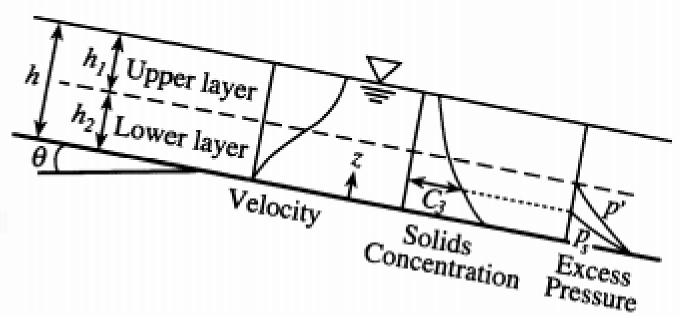

Figure 2-3 Structure of moving debris (Takahashi 2009)

In the figure, the hybrid flow is characterized by two distinct properties and two layers are defined. The upper layer is of turbulent suspension. This layer contains mainly turbulent water with very low percentage of grain materials, moving in fast speed with no excess water pressure development. The other layer is of considerable particle interaction. This lead to higher solid concentration, lower velocity and excess pore-pressure build-up along with the depth. The depth of each layer is according to the relatively solid concentration, and the ratio of the depths determines the behavior of the moving debris into two types. If the ratio is relatively small and the particle interaction dominates the mechanism, it is defined as stony debris flow; if the ratio is relatively large and the turbulent water layer is considered to cover the whole debris, it is a turbulent debris flow.

2.4. Classification

Debris flow could be classified based on the solid concentration and fine grain content of the whole mass (Schatzmann 2005). In this classification, debris flow is classified into granular flow, viscous flow and mud flow. The difference between these types is the difference of the dominant stress. To be more exact, the granular type is referred to those for which stress is dominated by particle collision; the viscous type is dominated by viscoplastic stress, and the turbulent-muddy type is dominated by turbulent mixing stress.

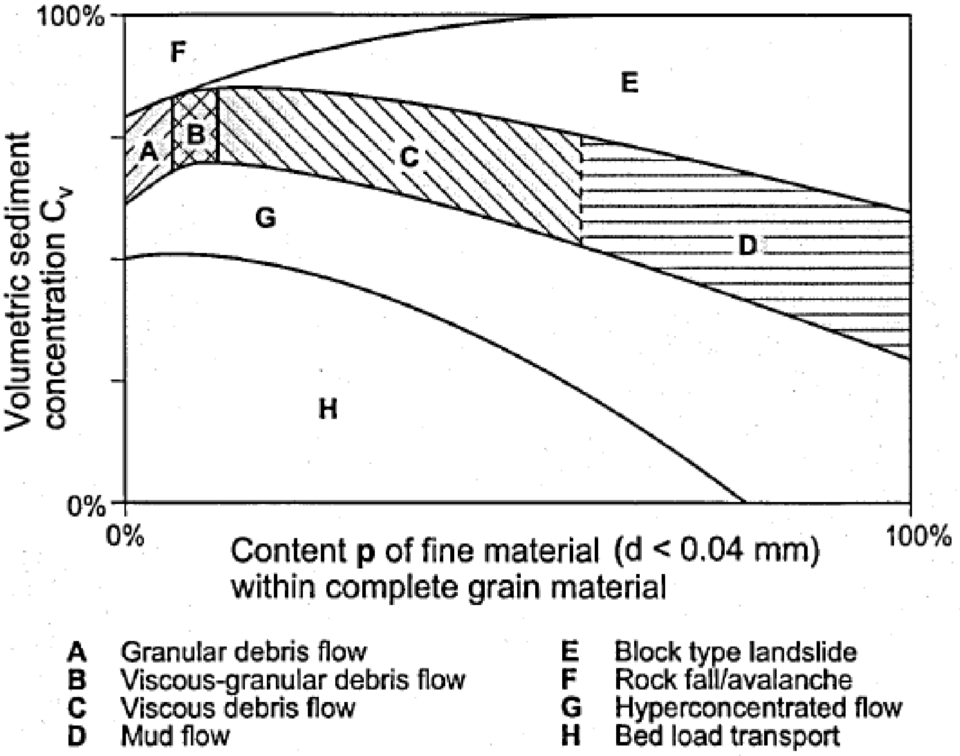

Figure 2-4 Adapted classification of debris flows (Coussot and Meunier 1996, Schatzmann 2005)

In Figure 2-4, debris flow is classified in to A-D four types. The granular debris flow consists of very limited fine grained material. It is usually further divided into a fluid phase and a solid phase depending on the grading of the flow structure. By contrast, the viscous debris flow behaves more or less as one homogeneous viscous phase. The flow is more laminar since the interstitial pore is filled with fine materials. In the mud flow, the fine grains are so dense in the pore space that interactions between coarse particles are assumed to be negligible. Depending on the sediment concentration and the flow geometry properties, the mudflow can exhibit either laminar or turbulent behavior. The classification also shows E-H types, which are other common types of natural mass movements (Schatzmann 2005).

Figure 2-5 also gives an example of the conclusion (Takahashi 2014) based on real events. The figure concludes the stony debris flow (Kamikamihorzawa) consists of much coarser materials and viscous debris flow (Jiangjia Gully) is relatively much finer. The turbulent-muddy debris flow has a coarser composite for the deposit and a finer one for the flow, showing good agreement with the viscous debris flow that is approximately in the middle.

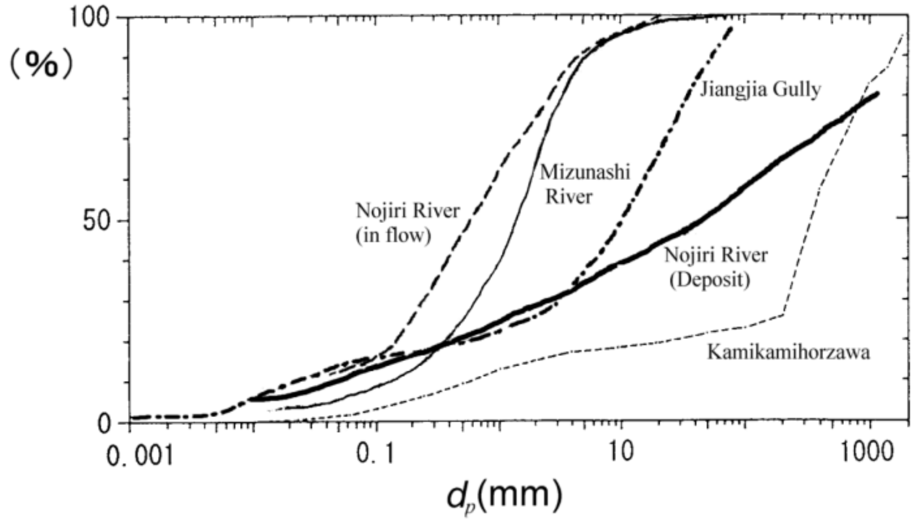

Figure 2-5 Distributions of grain size in stony, viscous and turbulent-muddy rivers (Takahashi 2014) Kamikamihorzawa: stony debris flow; Nojiri River: turbulent-muddy debris flow; Jiangjia Gully: viscous debris flow

Debris flow could also be classified based on the topographic and geological characteristics of their locations (Cruden and Varnes 1996). In this classification, debris flow is classified into hill-slope and channelized. Figure 2-6 shows the difference.

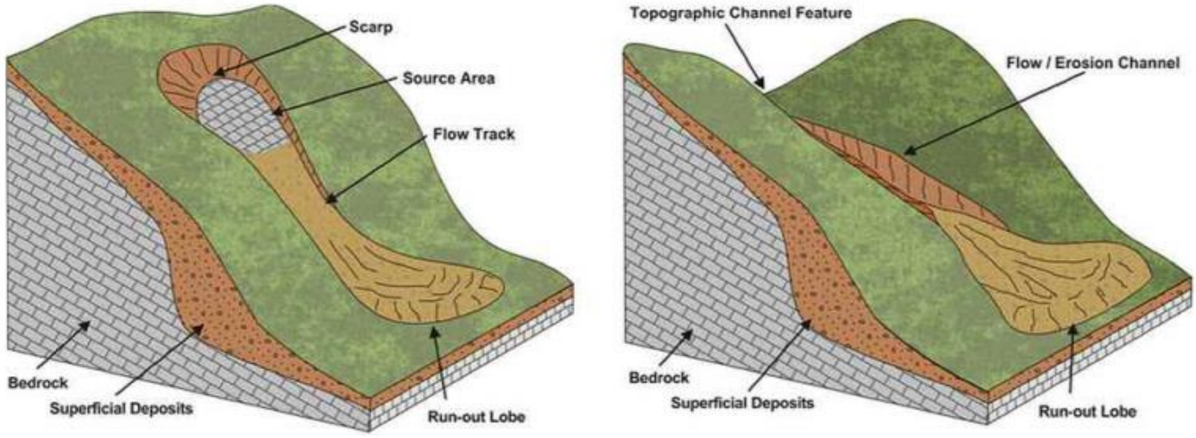

Figure 2-6 Hill-slope (left) and channelized (right) debris flow (Winter, Macgregor et al. 2005)

From the figure, the hill-slope type debris flow forms its own path down the valley slope before depositing material on lower locations with softer slope gradients, and the channelized type debris flow follows nature channel with the capacity to transport even large size of soil materials (boulders). Since these two types of debris flow depends on geological and topographic conditions, they are not isolated in some cases. For example, with given geological conditions, some debris flow start from the hill-slope form and turn into the channelized as the flow enter into channels.

2.5. Causes

The causes of debris flow could be defined in many aspects, but in principal there are two factors that trigger the debris flow. First, the instability of the individual or several slopes leads to completely failure because of the liquefaction process triggered by considerable water conditions such as heavy rainfall. Second, the strong forces from the extreme flows push the sediments and entrainment within the stream valleys. Both principal factors are strongly related to the water condition.

In general, the causes of landslides that are related to timing, two types are factors are introduced, preparatory factors and triggering factors (Mark, Nelson et al. 1994). Preparatory factors are indirect factors that affecting the slope or water condition to be less and less susceptible without triggering it, and triggering factors are the factors that turn the slope to become failure given with certain conditions. The interrelationship between them is bringing the debris flow on scene in both long and short term influence.

Preparatory factors involve a variety of aspects. For mountainside that is generally steep, it promotes gravity condition that is available for slope failure. For slope with specifically weak joint sets, the weakening of rock strength makes the slope vulnerable to the slope failure. For the weathering soil in bad weather or unfavorable moisture conditions, the weakening of soil strength would make it unfavorable for the slope stability. For the decreasing of the vegetation on the slope, the loosing of the soil makes the slope vulnerable. Additionally, for the topography with insufficient drainage system, the increasing surface water and the liquefaction process renders the slope to be vulnerable. For mountains under extreme weather conditions, the instability of potential slope failure is decreasing from time to time.

In regard to the source of the causes, the factors can be divided into internal and external. In the case of the trigger of debris flow, the internal factors are those causing reduction in the shear strength (shear resistance) and the external factors are those which lead to an increase of shear stress (Winter, Macgregor et al. 2005).

Table 2-2 Internal Causes (Winter, Macgregor et al. 2005)

Internal Causes	Description
Material	Unfavorable geological factors such as joints and faults. Weathering factors which decrease shear strength as a time matter.
Weathering	The soil strength parameters decreased because of the weathering process in both physical and chemical aspects. Slope ripening and soil development.
Pore-water pressure	Intense rainfall or unfavorable drainage system leads to a high degree of excess pore-pressure, results in decreasing effective stress and shear strength.

Table 2-2 shows the detailed internal causes. Causes due to material, weathering and pore-water pressure attributes to the loss of shear resistance within the slope, but the pore-water pressure is predominant cause in most cases. The increase of excess pore-pressure directly results in the decrease of effective stress, usually in a short term period. This applies to all the internal causes. Intense rainfall, poor drainage, sudden change of seepage would trigger the change of the pore-pressure condition in relatively a short time period. To summarize, the change of pore-water pressure is the principal internal cause for the initiation of debris flow.

Table 2-3 External Causes (Winter, Macgregor et al. 2005)

External Causes	Description
Removal of slope support	Construction effects such as excavation. Groundwater and streams erosion.
Increased loading	Intense rainfall with poor seepage, snow, etc. Construction events.
Transient effects	Earthquakes, vibrations or other factors that would trigger huge dynamic energy into the slope

Table 2-3 shows the external causes for debris flow. The main influence of external factors is to increase the shear stress. Increased loading and transient effects are positive to this factor. The removal of slope support decreases the effective stress, which is negative to the positive factor of the factor of safety, making the debris flow is more likely to happen.

2.6. Constitutive equations

Constitutive equations of debris flow are fundamental for debris flow study and numerical modeling (Egashira 1997, Takahashi 2014). It is based on the constitutive relations of the viscosity in the inertial regime, that shear stress and normal stress were found to depend on the square of the shear rate (Bagnold 1954). Constitutive equations have been evolved over time, and this chapter will introduce the basic of the concept.

Figure 2-7 shows the sketch of a uniform, one dimensional granular debris flow. By using momentum conservation, the shear stress and the isotropic pressure can be illustrated as:

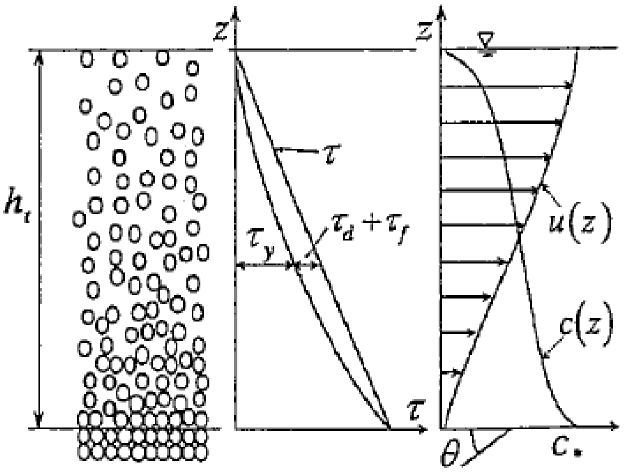

Figure 2-7 Sketch of a uniform granular debris flow (Egashira 1997)

$$0 = \int_z^{h_1} \rho_m \, g \sin\theta d_z - \tau(z) \qquad (2.1)$$

$$0 = \int_z^{h_1} \rho_m \, g \cos\theta d_z - p(z) \qquad (2.2)$$

$$\rho_m = (\sigma - \rho)c + \rho \qquad (2.3)$$

In which:

h_l : the flow depth;
g : the gravity acceleration;
θ : inclination of the bed;
τ : shear stress;
p : isotropic pressure;
ρ_m : mass density of the sediment;
ρ : mass density of the water
c : sediment concentration by volume of the mixture

Specifically, the expressions for the isotropic pressure and shear stress component in the granular debris have been proposed as: (Miyamoto 1985, Egashira, Ashida et al. 1989, Egashira and Ashida 1992)

$$\mathrm{p} = p_s + p_d + p_w \quad (2.4)$$

$$\tau = \tau_y + \tau_d + \tau_f \quad (2.5)$$

In which:

p_s : pressure of static interparticle contacts;

p_d : dynamic pressure due to inelastic collisions of interparticle contacts,

$$p_d = \rho k_d(\sigma/\rho)e^2c^{1/3}d^2(\partial_u/\,\partial_z)^2\,; \quad (2.6)$$

p_w : hydrostatic pressure of interstitial water;

$$p_w = \rho g(h_l - z)\cos\theta \quad (2.7)$$

τ_y : yield shear stress;

$$\tau_y = p_s \tan\phi_s \quad (2.8)$$

τ_d : shear stress due to inelastic collisions of interparticle contacts;

$$\tau_d = \rho\, k_d(1-e^2)(\sigma/\rho)c^{1/3}d^2(\partial_u/\,\partial_z)^2 \quad (2.9)$$

τ_f : shear stress supported by the interstitial water;

$$\tau_f = \rho k_f(1-c)^{5/3}\,/c^{2/3}d^2(\partial_u/\,\partial_z)^2 \quad (2.10)$$

k_d : a semitheoretical coefficient (Egashira, Ashida et al. 1989);

$$k_d = 0.0828 \quad (2.11)$$

k_f : empirical constant of the ratio between shape parameters for sediment particle and the pore space in the range of 0.16-0.25 (Ashida, Egashira et al. 1985);

$$k_f = 0.16 \quad (2.12)$$

ϕ_s : interparticle friction angle

$(\partial_u/\,\partial_z)^2$: the square of the shear rate (Bagnold 1954)

By substituting all equations into (2.1) and (2.2), yields:

$$p_s\tan\phi_s + \rho {f_d}^2(\partial_u/\,\partial_z)^2 + \rho {f_f}^2(\partial_u/\,\partial_z)^2 = \rho g\sin\theta\int_z^{h_1}\left\{\left(\frac{\sigma}{\rho}-1\right)c+1\right\}d_z \quad (2.13)$$

$$p_s + \rho f_{pd}d^2(\partial_u/\,\partial_z)^2 = \rho g\cos\theta\int_z^{h_1}\left\{\left(\frac{\sigma}{\rho}-1\right)\right\}cd_z \quad (2.14)$$

In which f_d, f_f and f_{pd} are defined as:

$$f_d = k_d(1 - e^2)\ (\sigma/\rho)c^{1/3} \tag{2.15}$$

$$f_f = k_f(1 - c)^{5/3}\ /c^{2/3} \tag{2.16}$$

$$f_{pd} = k_d(\sigma/\rho)e^2c^{1/3} \tag{2.17}$$

In the final equations (2.13) and (2.14), only three unknown variables (p_s, c, u) are left, and p_s is modeled to close the governing equations. At the bottom boundary (z = 0), τ_d and τ_f decrease to zero. The external driving stress is left to τ_f. Since p_s is depending on the sediment concentration in the flow field, and it is asymptotically equal to $\mathrm{p} - p_w$ as the c becomes c_o (the sediment concentration at the non-flowing layer), p_s can be expressed as:

$$\frac{p_s}{\mathrm{p}-p_w} = f(c, c_o) = (c/c_o)^{1/n} \tag{2.18}$$

In which n is a positive integer.

Then the whole equations only have two variables left, the concentration c and the flow velocity u. Depending on the roughness of the bed, the concentration c can be assumed, and the velocity flow field profile can be derived.

2.7. Physical modeling of rotating concept

2.7.1. The work of Sassa, Kyoji

Sassa studied the rainfall induced landslide by performing a small scaled flume test (Wang and Sassa 2003). It aims to study the effects of grain size on pore-pressure generation and the landslide failure behavior. Figure 2-8 shows the flume test concept.

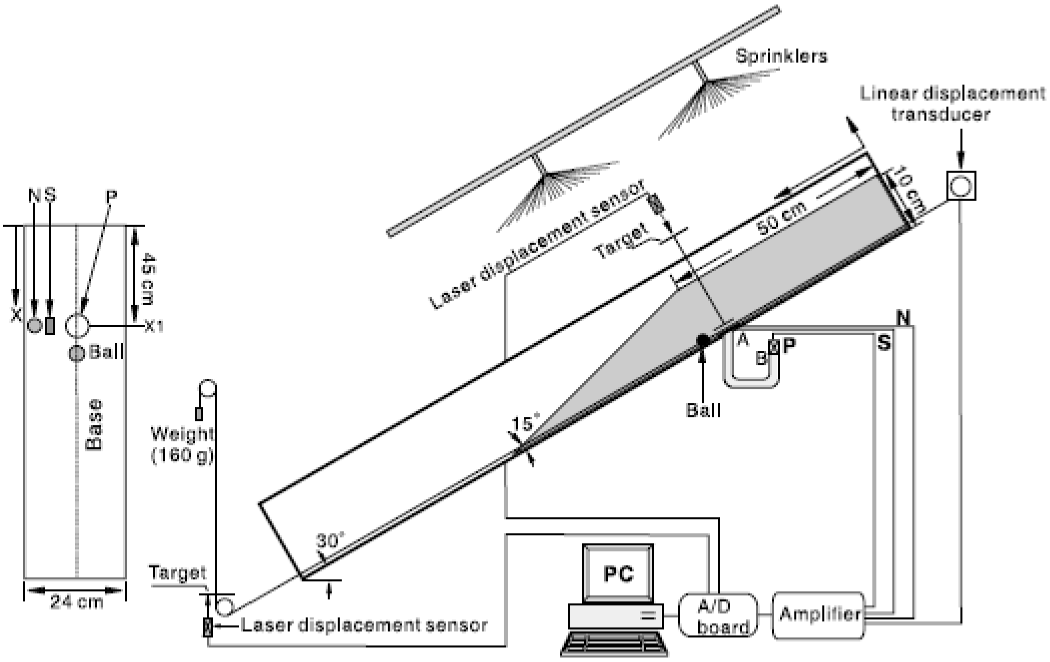

Figure 2-8 Flume test apparatus (Wang and Sassa 2003)

In the flume apparatus, silica-sand grains were being glued to the base of the flume apparatus as the bed roughness. Normal stress and shear stress were measured by transducers installed to keep track of the stresses in the debris. A styrene foam ball connected with a linear displacement transducer is buried inside the debris mass to measure the displacements. A laser displacement sensor is also installed to further correct the displacement. Two spray nozzles are placed above the flume apparatus. Rainfall is therefore simulated by supplying water constantly with a pump, and the distance to the nozzles is adjustable. All tests processes are also recorded by a video camera.

After proper set up of the samples, measurement starts as the spraying process begins. The spraying process mimics the rainfall process, and the sample begins to be saturated. The behavior of the debris is then recorded. The failure mode is analyzed and concluded as Figure 2-9.

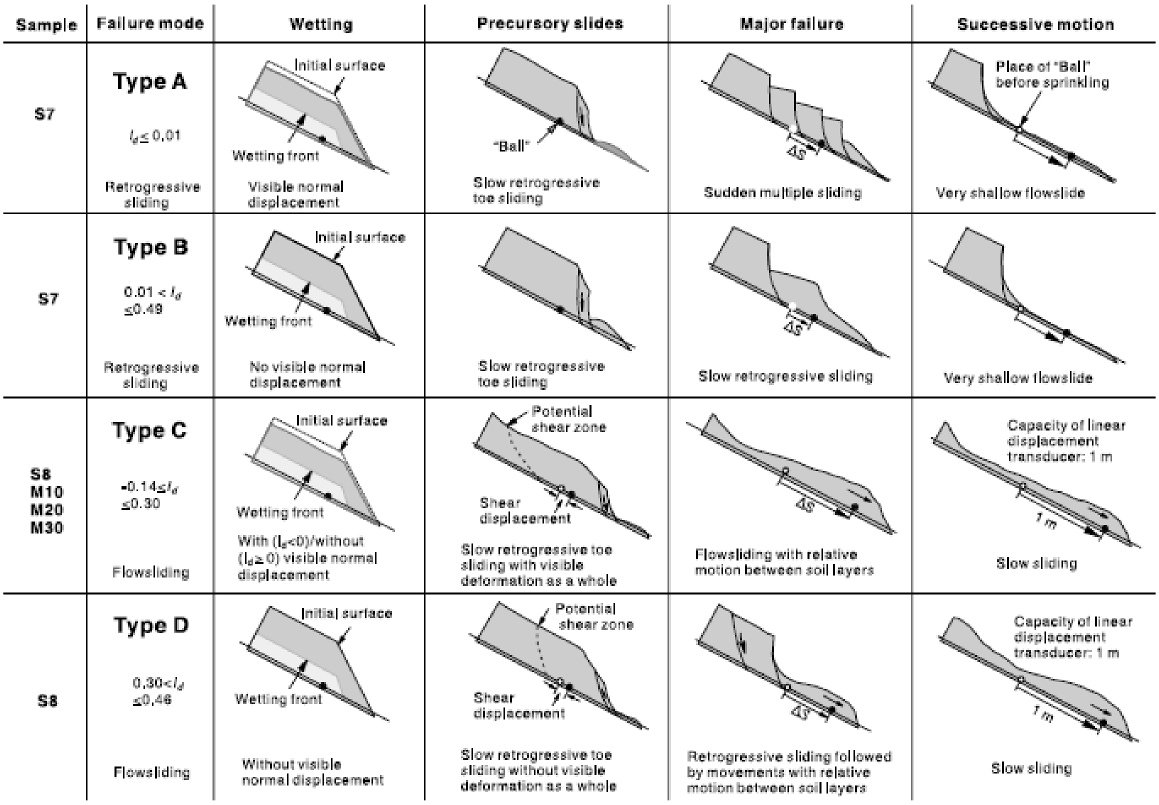

Sample	Failure mode	Wetting	Precursory slides	Major failure	Successive motion
S7	**Type A** $I_d \leq 0.01$ Retrogressive sliding	Visible normal displacement	Slow retrogressive toe sliding	Sudden multiple sliding	Very shallow flowslide
S7	**Type B** $0.01 < I_d \leq 0.49$ Retrogressive sliding	No visible normal displacement	Slow retrogressive toe sliding	Slow retrogressive sliding	Very shallow flowslide
S8 M10 M20 M30	**Type C** $-0.14 \leq I_d \leq 0.30$ Flowsliding	With (I_d<0)/without ($I_d \geq$ 0) visible normal displacement	Slow retrogressive toe sliding with visible deformation as a whole	Flowsliding with relative motion between soil layers	Slow sliding
S8	**Type D** $0.30 < I_d \leq 0.46$ Flowsliding	Without visible normal displacement	Slow retrogressive toe sliding without visible deformation as a whole	Retrogressive sliding followed by movements with relative motion between soil layers	Slow sliding

Figure 2-9 Summarized failure mode (Wang and Sassa 2003)

The result shows that the major failure and the successive motion of each test are unique, and the failure mode is closely related to the composites of the samples and the saturation process. Other test results show the maximum pore-pressure build-up after failure differed from samples of different grain size, and the failure mode was also observed to be depended greatly on the grain size of the samples. To further study the variation related to the excess pore pressure generation and grain size, a coaxial cylinder was invented. Figure 2-10 shows the apparatus. The coaxial cylinder has four rotating rods, and it can rotate samples consisting of soil and water while measuring the pore pressure with sensors installed in the base.

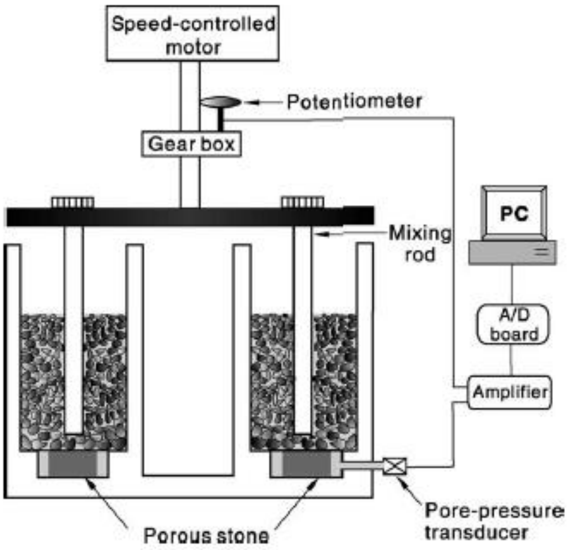

Figure 2-10 Coaxial rotating apparatus (Wang and Sassa 2003)

With the coaxial cylinder, samples of different grain size distribution are tested. Figure 2-11 shows part of the conclusion. For the sample naming, S7 is coarse silica-sand, S8 is finer silica-sand, and M10, M20 and M30 are combinations of S8 with 10%, 20% and 30% silt respectively. Results conclude that the pore-pressure increased with velocity due to the floating grains, and fine-grained content have considerable effects on the pore-pressure build-up process.

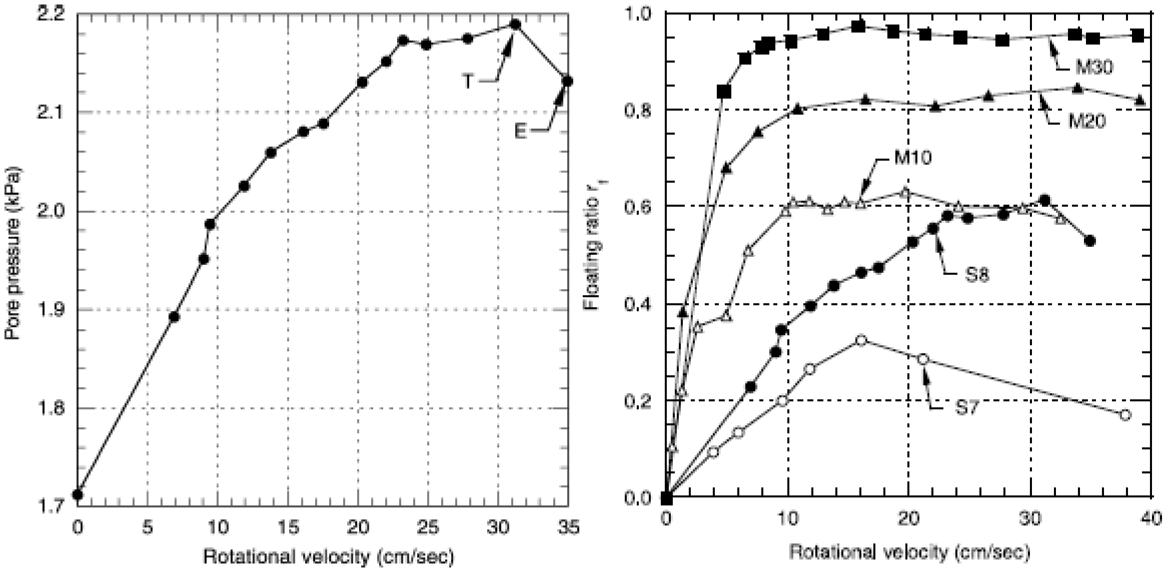

Figure 2-11 Pore pressure development (left) & Floating ratio (right) (Wang and Sassa 2003)

In summary, Sassa illustrated good examples of the factors that may influence the excess pore pressure build-up. However, the test program did not control all variables very well. All tests were performed by putting dry samples inside with 15cm height and filled the water to reach the same height. This do not necessary ensure all samples share the same volume or concentration, either by weight or by volume. Additionally, test samples are limited to the silica-sand with up to 30% silt content. The limited grain size does not necessary reveal the whole picture (especially the fine grain), and cannot be applied to all situations in Norway (Vegvesen 2014).

2.7.2. The work of Yu, Xiang

Based on the Sassa's coaxial cylinder concept, another coaxial cylinder was built up for similar purpose (Yu 2015). Two apparatuses are slightly different as Figure 2-12 bellowed. The main differences are the apparatus geometry and sensor placement.

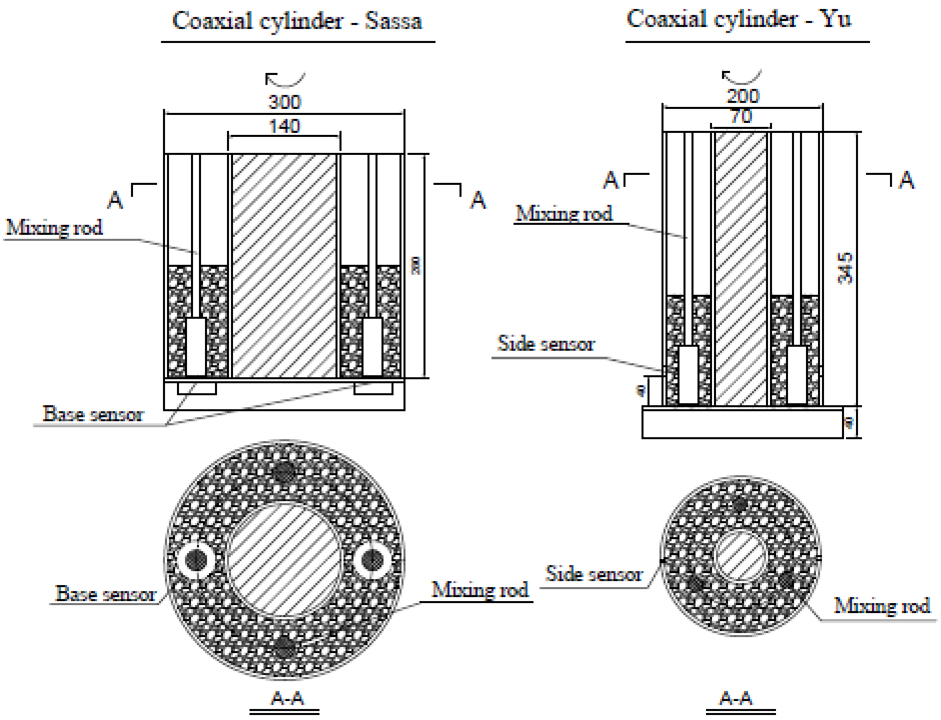

Figure 2-12 Coaxial cylinders, Sassa & Yu

In Yu's study, the test program is further improved with specified solid fraction concentration of samples and broader range of the grain size. More tests are performed with more clear indication of the influence of each parameter, and the program also runs with a higher velocity. Figure 2-13 shows the test program. Here *C* stands for the sediment concentration by volume, and *S* stands for the silt content percentage by the total weight of the grains.

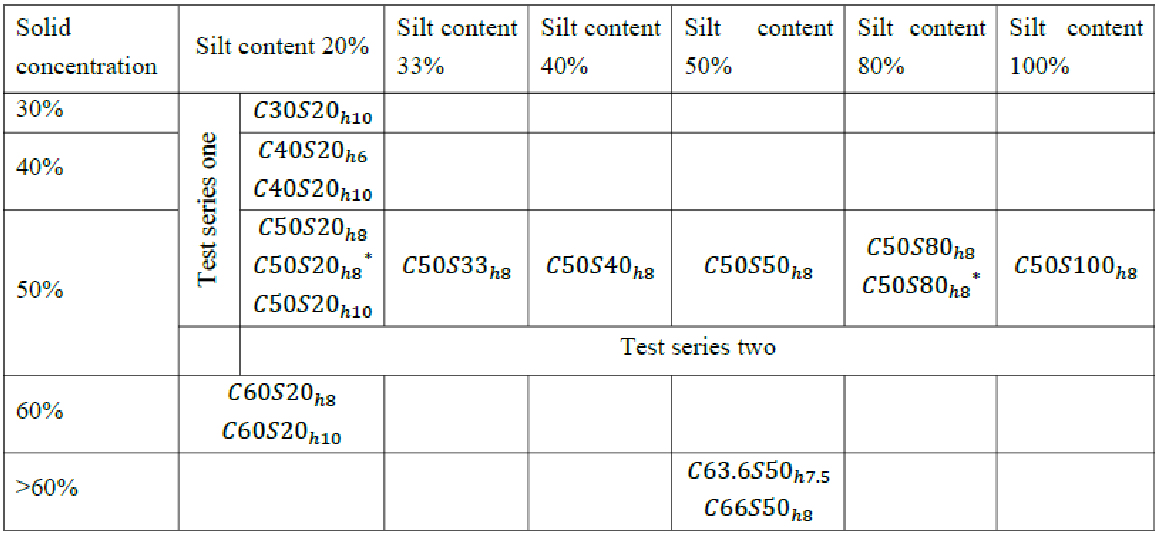

Solid concentration	Silt content 20%		Silt content 33%	Silt content 40%	Silt content 50%	Silt content 80%	Silt content 100%
30%	Test series one	$C30S20_{h10}$					
40%		$C40S20_{h6}$ $C40S20_{h10}$					
50%		$C50S20_{h8}$ $C50S20_{h8}{}^{*}$ $C50S20_{h10}$	$C50S33_{h8}$	$C50S40_{h8}$	$C50S50_{h8}$	$C50S80_{h8}$ $C50S80_{h8}{}^{*}$	$C50S100_{h8}$
		Test series two					
60%	$C60S20_{h8}$ $C60S20_{h10}$						
>60%					$C63.6S50_{h7.5}$ $C66S50_{h8}$		

Figure 2-13 Test samples, Yu(Yu 2015)

Although the test program becomes more comprehensive, the coaxial cylinder is inherent with two considerable defects. The first one is the centrifugal force. Although pure water test is performed beforehand as a reference, the centrifugal effects in the pure water should vary from the effect in the debris material. The centrifugal force also causes problems such as unstable vortex and the change of the flow height which significantly affect the results. Additionally, the horizontal rotating direction is also different from the real nature of the debris, that shearing the ground in vertical direction. As for these two major reasons, conclusions from coaxial cylinder are questionable and limited.

2.7.3. The work of Rickenmann, Dieter

The nature of debris flow can be viewed either as laminar or turbulent flow, which is illustrated in rheological viewpoints. To study the rheologic diameter of the debris material, a rotating drum apparatus was built up to generate stationary surges of debris materials (Kaitna and Rickenmann 2007). By testing the rheologic behavior of a homogeneous transparent liquid polymer, results are derived to estimate a Bingham model.

Rheologic behavior can be expressed as equation of many forms, and the Hershcel-Bulkley model is more inclusive. The concept can be illustrated as equation (2.19) (Bird, Dai et al. 1983, Johnson and Rodine 1984, Pierson and Costa 1987).

$$\tau = \tau_y + K\gamma^n \tag{2.19}$$

In which:

τ : shear stress;
γ : shear rate;
τ_y : yield stress;
K : Herschel-Bulkley coefficient;
n : Herschel-Bulkley exponent.

Different rheologic behavior can be distinguished by controlling the parameter of equation (2.19). A simple example is Newtonian fluid, where the yield stress τ_y and Herschel-Bulkley exponent n is 0, showing the shear stress depends on the linear function of $f(\gamma)$. The Bingham model is a simple form of equation (2.19). In the Bingham model, the Herschel-Bulkley exponent n is 1 and the K becomes the Bingham viscosity η.

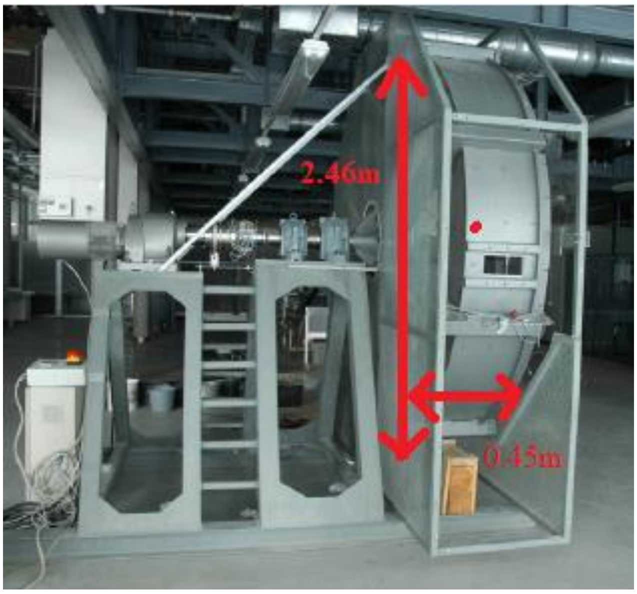

Figure 2-14 Rotating drum, Rickenmann (Kaitna, Rickenmann et al. 2007)

In the experiment, different mixtures of synthetic polymer and water were tested. The flow parameters of the Bingham model is measured, and results are further verified with the measurements performed with a conventional coaxial cylinder rheometer. Figure 2-14 shows the rotating drum apparatus. The apparatus has a diameter and width of 2.46m and 0.45m. Between the motor engine and the axis of the drum, a torque flange is installed to allow for torque measurement. The torque measurement can indicate the average shear stress the equipment applies, with an accuracy of 0.05%. Normal stress and shear stress measurement are also installed at two locations on the circumference by using single point load cells. Flow depth is measured by laser sensor in the middle of the channel section. For flow velocity measurement, the average flow velocity is assumed to be equal to the rotation speed of the drum at the bed, and surface velocity is derived from the analysis of video recording. Pore fluid pressure is measured by a pressure transducer attached to a reservoir. A filter plate of variable pore size is installed at the base of the drum, adjacent to the test material. The variable pore size of the filter is actually a tricky part. A ceramic filer of maximum 0.1mm pore size is chosen, while in fact it is difficult to determine the proper threshold value of the grain diameter separating particles(Davies 1986, Iverson 1997, Julien and O'Brien 1997, Yu 2015).

Figure 2-15 and Figure 2-16 show part of the measurement results. Figure 2-15 shows the shear thinning behavior of each sample, and Figure 2-16 illustrates the flow depth at different velocities.

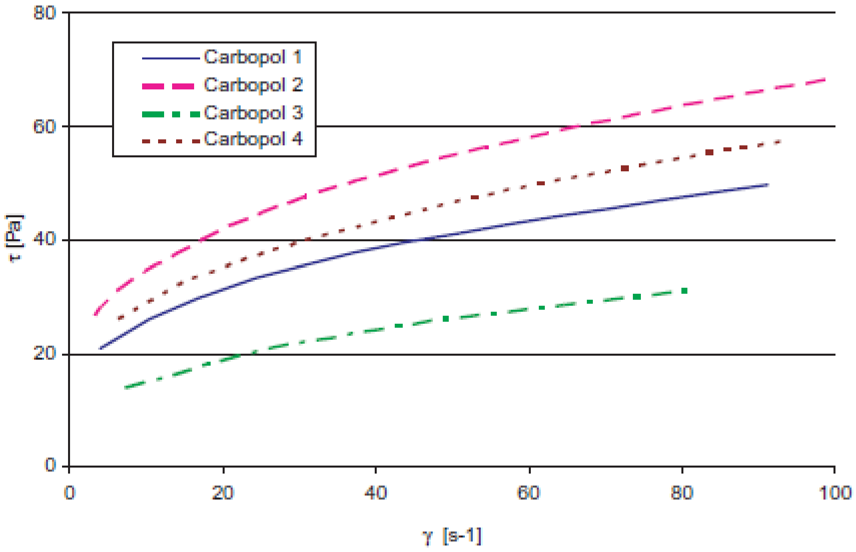

Figure 2-15 τ (Pa) — $\gamma(s^{-1})$ (Kaitna, Rickenmann et al. 2007)

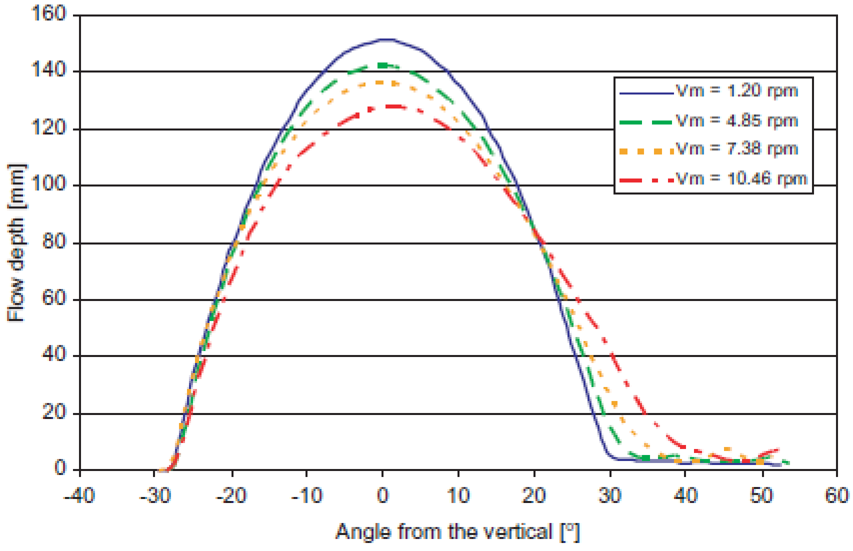

Figure 2-16 Flow depth (mm) — Angle from the vertical (°) (Kaitna, Rickenmann et al. 2007)

Based on estimations of iterative strain rate and depth averaged flow equation, two simple methods are proposed to be compared with the measurement value. Figure 2-17 shows part of the comparison. The analysis concludes that the Bingham model can be estimated with both simple approaches. The conclusion also indicates the rheologic models may be an appropriate tool to estimating the flow behavior of debris material.

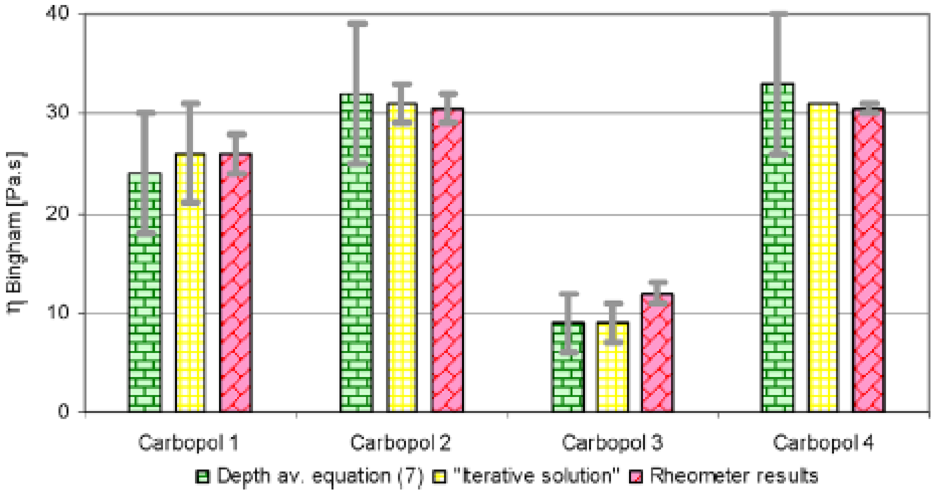

Figure 2-17 Comparison of results of two proposals and rheometer measurement (Kaitna, Rickenmann et al. 2007)

This study is successful as it achieves two goals. It builds up a rotating drum apparatus with well described experiment and measurement setup, and succeeds in measuring and evaluating the rheologic measurements with verified reference. Although it is not an aim to study the rheologic property of the debris material in this master thesis, measurements such as the flow velocity and shear stress can still be important. E.g., the excess pore pressure build-up is significantly related to the flow velocity profile.

2.7.4. The work of Hotta, Norifumi

By measuring the pore water pressure in simulated debris flow with a rotating mill apparatus, Hotta shows excess pore pressure exists in the laminar moving debris (Hotta and Ohta 2000, Hotta 2011). It indicates the traditionally assumed hydrostatic water pressure is not proper, and the excess pore pressure is an outcome of Reynolds stresses due to the shearing of interstitial water. The result was also verified by the constitutive equations as followed.

$$u = 3/5u_m\{1-(1-z/h)^{2/3}\} \tag{2.20}$$

$$\rho_f = k_f \rho d^2 (1-c)^{\frac{2}{3}} / c^{\frac{2}{3}} * 25{u_m}^2 / 4h^2 (1 - z/h) \tag{2.21}$$

In which:

u : velocity of the assumed depth;

ρ_f : pore pressure of the assumed depth;

u_m : mean velocity of the moving debris;

k_f : the ratio between shape parameters for the sediment particle and the pore space in the range of 0.16-0.25 (Ashida, Egashira et al. 1985, Egashira, Ashida et al. 1989);

c : sediment concentration by volume;

d : diameter of the sediment particle;

ρ : density of the pore water;

z : the depth of the point assumed;

h : the depth of the moving debris.

The constitutive equation is calculated from the impact of hydrostatic pore pressure and the Reynolds stresses from the turbulent mixing of the pore water. It shows the velocity and pore pressure profile in the cross section. The equation indicates that when the sediment concentration profile is uniform, the pore pressure distributes linearly from the flow surface to the bed, increasing in proportion to the square of the particle diameter and mean velocity.

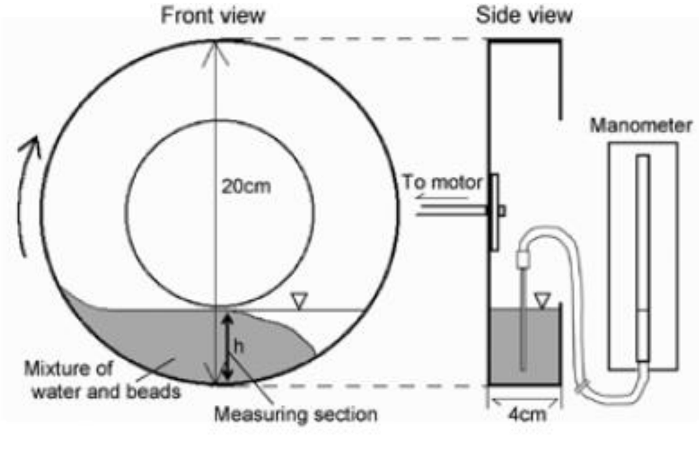

Figure 2-18 Hotta rotating mill (Hotta 2011)

Figure 2-18 shows the experiment apparatus. The rotating mill is 4 cm wide and 20 cm in diameter. 4mm diameter glass beads were glued in the base of the apparatus to simulate bed roughness. A pitot tube was placed into the rotating mill vertically with the opening facing perpendicular to the flow direction to measure the pore water pressure. Different diameters of glass beads (from 1mm to 6mm) and plastic beads (4mm and 6mm) were used as the granular debris material. The volume and initial concentration of the each test is controlled, as $50cm^3$ glass/plastic beads and $130cm^3$ water to form a mixture.

After the experiment, all measurement results were verified by the assumption from equations (2.20) and (2.21). Result shows all velocity measurements match the velocity assumption from constitutive equation (2.20), and pore pressure measurement from 6mm glass beads and 6mm plastic beads match the pore pressure assumption from constitutive equation (2.21).

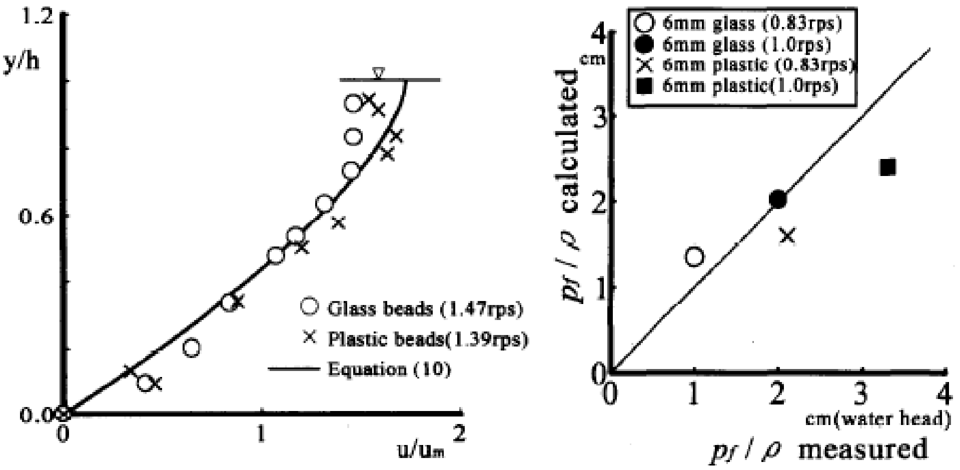

Figure 2-19 Velocity profile (left) & Pore pressure profile (right) (Hotta 2011)

As mentioned above, this conclusion does not reveal the whole picture. Not all pore pressure profiles match the expected assumption from constitutive equation (2.21). As for the diameters less than 6mm, pore pressure gradient was found to be higher than the calculate value. The reason is the flow lines of particles and interstitial water disagree during the motion, and particles were dragged above the water surface as temporary unsaturation. The effect due to the internal flow besides Reynolds stress increased the pore water pressure measured. And this effect was examined to be significant when the particle diameter is small, and can be neglectable when the diameter is larger (6mm).

Overall, results from Hotta are satisfactory as it succeeded in part of the verification of the constitutive equations, showing the excess pore pressure exists and so as the function ability of the rotating mill apparatus. However, the test program is limited with theoretical model, that only plastic/glass beads were tested instead of actual debris material. The constitutive equation is also limited by the theoretical assumption of uniform particle diameter and uniform concentration distribution of laminar flow. Further tests may be performed with real materials of a fine range of grain size which suits the condition in Norway, which becomes an issue in this thesis.

3. Rotating drum apparatus modeling

3.1. Introduction

A small-scale rotating drum apparatus was developed to perform the modeling of the moving debris. The original idea is from Kaitna & Rickenmann (details could be referred to *chapter 2.7.3 The work of Rickenmann)* to study the rheological behavior of debris flow. Figure 3-1 presents the overview of the apparatus system. The system includes the rotating drum, relevant motor and gear, data acquisition (DAQ) system, control program, amplifier and power supply.

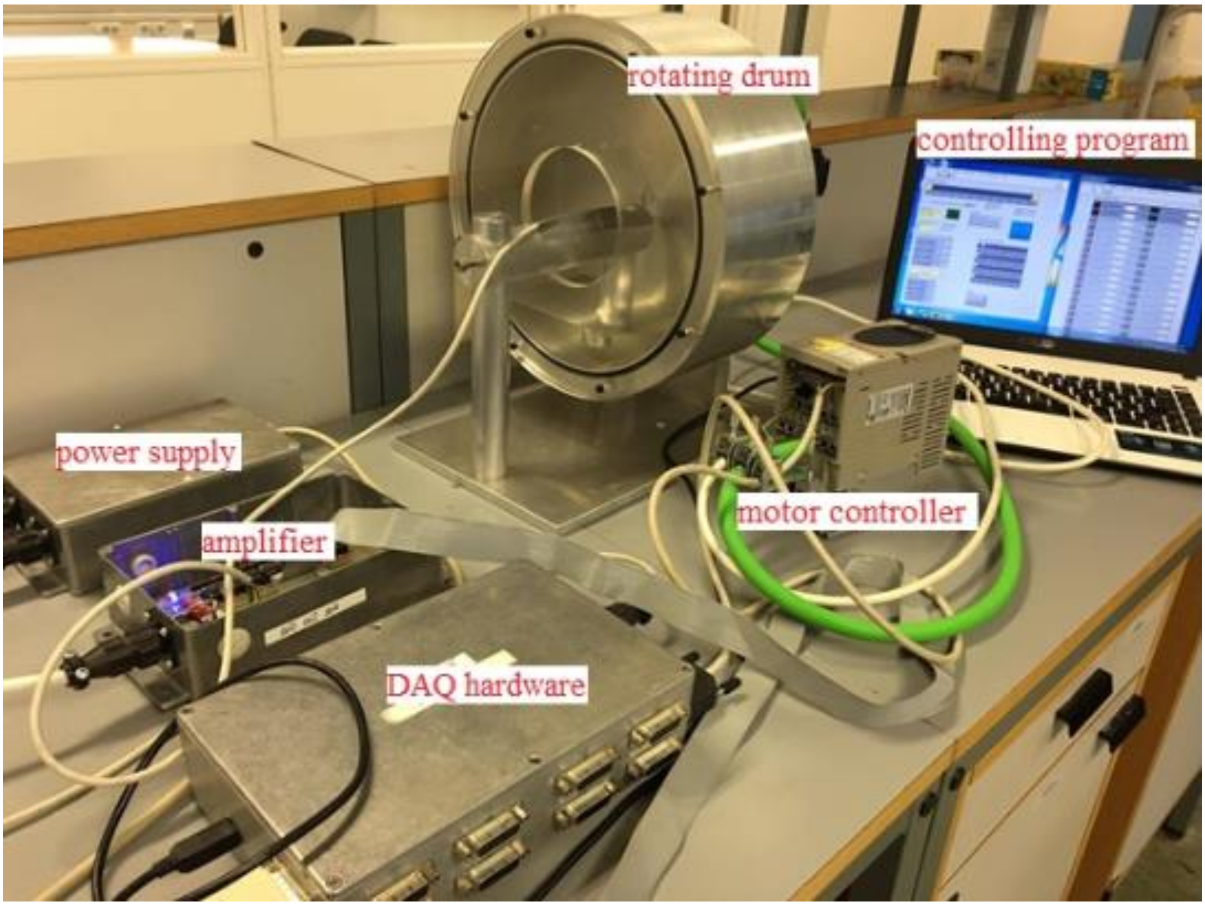

Figure 3-1 overview of the rotating drum system

The purpose of the apparatus design is to simulate the debris flow movement and to measure the pore pressure build-up during the motion. The rotating drum is able to rotate up to

200RPM which is fully available to provide all ranges of steady flow. Pore pressure sensor is installed in the base of the sensor bar to measure the pore pressure in the lower middle section of moving debris. The data acquisition system can transform the pore pressure data to the controlling program, and all data can be saved and analyzed.

3.2. Methodology

3.2.1. Floating ratio

Floating ratio is a term to describe the degree of excess pore pressure build-up of a sample during motion (Wang and Sassa 2003). Although all samples were formed to the same volume and concentration, the flow depth differs for different samples as the saturation settlements are different. Together with slightly different unit weight of different mixture, it is not proper to compare the value of excess pore pressure from different tests. The floating ratio is therefore introduced as a kind of the excess pore pressure built-up gradient, which normalize the excess pore pressure by the total normal stress:

$$r_f = (u - u_s)/(\sigma_t - u_s) \tag{3.1}$$

In which:

r_f : floating ratio;
u : pore pressure at the measured depth during motion;
u_s : hydrostatic pore pressure at the measured depth, $u_s = \gamma_w * h$;
σ_t : total normal stress, $\sigma_t = \gamma_s * h$
h : measured depth.
γ_w : unit weight of the water, $\gamma_w = 1.0\ gf/cm^3$
γ_s : unit weight of the saturated soil, $\gamma_s = \gamma_w * \frac{e}{1+e} + \gamma_d$.

The floating ratio r_f ranges from 0 (all grains are settled) to 1 (all grains are floating above the measured depth). It can be therefore indicated that the floating ratio also depends on the measured depth. The floating ratio at the basal layer should be the highest among all measured depths.

3.2.2. Viscosity

In the grain-inertia regime which applies for the granular debris flow, a constitutive relation was proposed by Bagnold that shear stress and normal stress depend on the square of the shear rate (Bagnold 1954). This constitutive relation becomes a fundamental part of the constitutive equations and other granular debris study (Schatzmann 2005, Takahashi 2014). Since the sandy material in this study fulfills the granular debris classification, this constitutive relation can be verified by measuring the shear rate and shear stress during the motion of different speed (or any other proportional parameters).

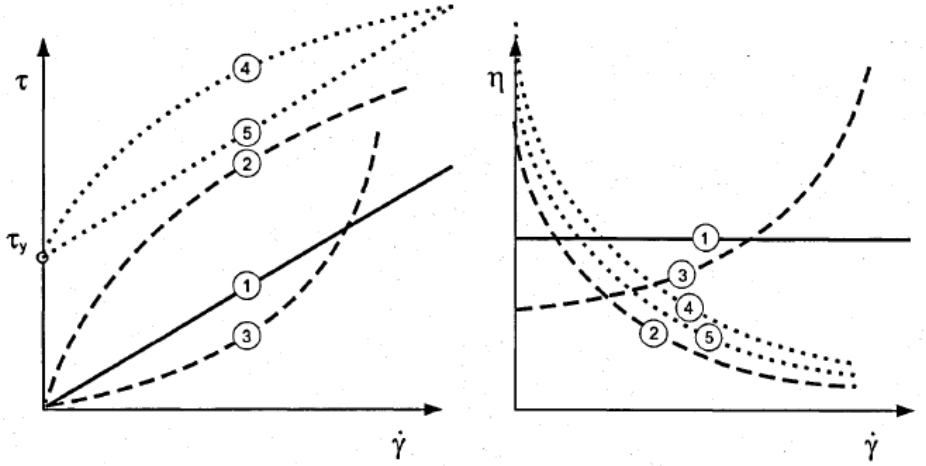

Figure 3-2 Common types of flow curves (left) & viscosity curve (right) (Schatzmann 2005)

Figure 3-2 shows the classification of flow behavior. 1 is Newtonian fluid, 2 is shear-thinning behavior, 3 is shear-thickening behavior 4 is shear-thinning behavior with yield stress and 5 is the Bingham model that is described in *chapter2.7.3 The work of Rickenmann.* Among these models, the shear-thickening behavior is the constitutive relation assumed (shear stress depends on the square of the shear rate) for the granular debris flow. The assumption was made based on a pioneer experiment (Bagnold 1954), and we would like to verify this behavior with the rotating drum apparatus.

A simple solution to indicate the shear stress is to derive the torque the motor applies during the motion. Taking it as a global behavior, the shear rate could also be assumed to be equal to the rotation speed of the drum at the channel bed. However, to measure the rheologic property of the moving debris was not the concern of this thesis when the apparatus was being constructed. Unfortunately, the torque measurement is not available without any torque flange installation. The attempt of using voltage or any other electronic signal as calibration also fails as the energy input of the step motor is not equal to the energy output of the rotating motion. Instead, two methods are proposed to derive the torque or shear stress based on indirect calculation as followed.

Method 1 – lever indication for the deviation of the center of gravity

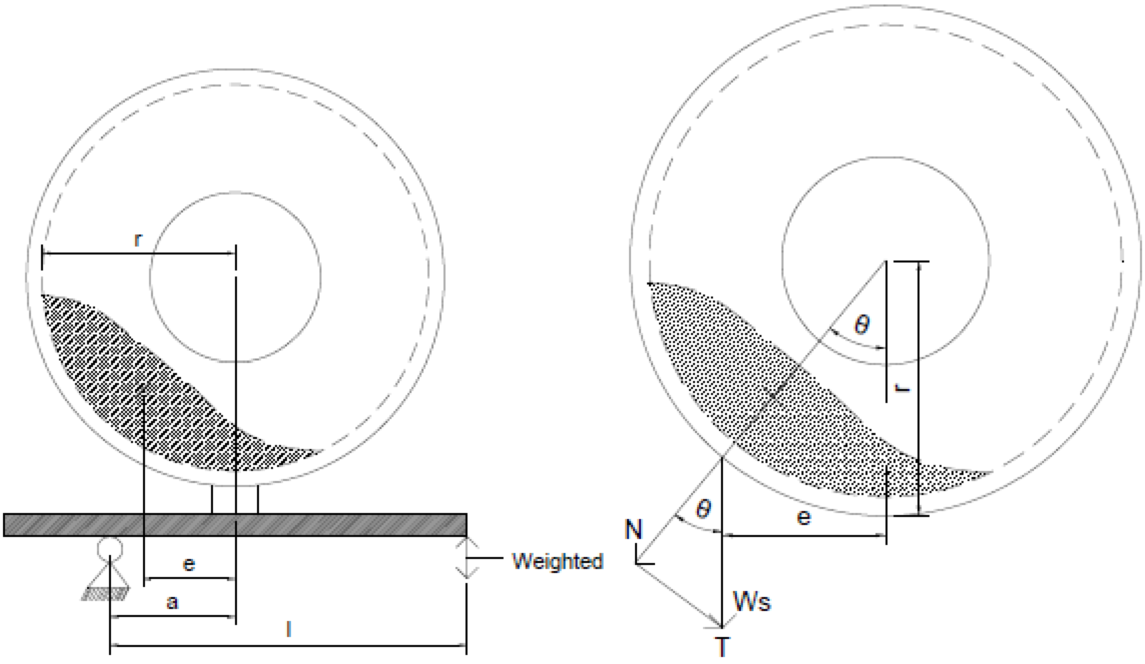

Figure 3-3 Simple illustration of method 1

The method1 is to derive the deviation of the center of gravity by measuring the change of the weight on the lever to fulfill the moment equilibrium. The apparatus was set on a firm plate, fixed as the Figure 3-3 illustrates. The horizontal distance between the fix point and the center of the apparatus is measured as *a*, and distance between the fix point and the end of the plate is measured as *l*. The radius of the apparatus is r, and the shift of the center of the gravity of the debris material is defined as e. The weight on the end of the plate was measured before and during the rotating moment as W_1 and W_2. The weight of the apparatus is M, and the weight of the debris material is W_s. The moment equilibriums before and during the rotation are:

$$M * a + W_s * a = W_1 * l \tag{3.2}$$

$$M * a + W_s * (a - e) = W_2 * l \tag{3.3}$$

The deviation of the center of the gravity can be therefore derived by substituting two equations as:

$$-W_s * e = (W_2 - W_1) * l$$

$$\Delta e = (W_2 - W_1) * l \tag{3.4}$$

After deriving the center deviation, based on the force analysis on the right graph of Figure 3-3, the shear force can therefore be calculated as:

$$\sin\theta = e/r \tag{3.5}$$

$$T = W_s * \sin\theta \tag{3.6}$$

In which T is the total shear force and θ is the deviation angle to the center.

Method 2 – sections calculation of the shear force

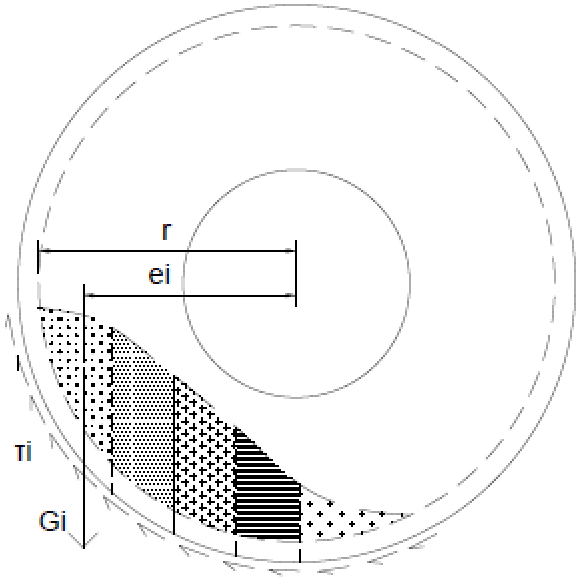

Figure 3-4 Simple illustration of method 2

An alternative method is presented as method2. The shear stress is no longer considered as a global behavior as method1, as the shear stress is considered to vary much from different points along the curve line. Several sections are determined as Figure 3-4. Based on video recording, the deviations of the center of gravity are defined as e_i, the deviation angle to the center as θ_i. Similar to method1, the force analysis can be summarized as:

$$\sum \tau_i = \mu \sum N_i \tag{3.7}$$

$$\sum N_i = \sum G_i * \cos\theta_i \tag{3.8}$$

In which N_i and G_i are the normal force and the gravity of each section, and μ is the coefficient of dynamic friction.

Methods evaluation

Based on moment equilibriums, method1 derives very accurate value of the total shear force on the basal layer. By comparison, method2 is more careful with calculating the shear stress in sections. But it is not necessary as the initial idea is taking the viscosity of the whole mass as a global behavior. In addition, the center deviation of the gravity in this method is derived from video images, while requiring additional test to measure the coefficient of dynamic friction. All these conditions add up inaccuracy of the result.

Both methods base on the assumption that the grains of the debris and the water form a continuous homogenous flow during the motion. This is, however, not the case in the experiment. The grading situation is highly considerable in this case, that two phases are distinguished. The sandy phase is partly apart from the water phase, that the deviation of the center of the gravity can no longer be taken as the one derived from method1 (the left graph of Figure 3-5). This is also the scene in the literature study *(chapter2.7.4 The work of Hotta),* that two phases are formed with the granular debris simulation (the right graph of Figure 3-5 (Hotta and Ohta 2000)).

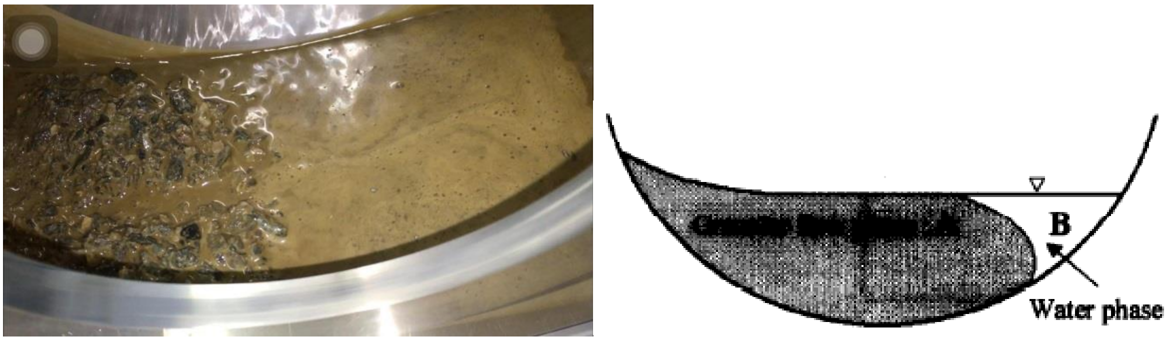

Figure 3-5 Two phases of granular flow

In conclusion, these two theoretical proposals miss the true nature of the granular flow, and therefore not being able to derive the indirect torque or shear stress measurement. A direct torque flange equipment is suggested be installed between the motor engine unit and the axis of the rotating drum for direct measurement in future study.

But still, a bold proposal is also stated here, if it is still valuable to measure the shear force in an indirect way. Although the two phases exist in the motion that the whole mixture cannot be viewed as a continuous homogeneous flow, the shear stress difference between the water phase and the particle phase is distinguished. The rotating shearing has a much stronger influence on the particle phase than the water phase. Taking the water phase as a kind of load effect on the particle phase, it may be possible to perform the measurement with only debris particle, and adding the load effect from the water phase in the evaluation.

3.2.3. Bernoulli's principle

Bernoulli's principle applies to incompressible and inviscid flow, telling that a steady flow follows the conservation of energy. That is, the total energy of every point in a fluid along a streamline should be the same. There are many forms of the equation, and one of them is:

$$\frac{1}{2}\rho v^2 + \rho g h + p = constant \tag{3.9}$$

In which,

ρ = the density of the fluid
v = the velocity at a point
g = acceleration due to gravity
h = the relevant elevation of the point
p = the water pressure at a point

To verify the applicability of the principle, it should be noted that the viscosity of any kind of debris flow should not be neglectable, as the friction between the grains and water exists in all kinds of debris flow. This is also the major difference between debris flow and other pure fluid. Therefore, it is not proper to apply this principle to debris flow study. However, Bernoulli's principle may work for the granular debris to some extent. In granular debris, since the void between grain particles is very large, the excess water pressure of the interstitial fluid is very short lived. That is, the granular debris can be viewed as an incompressible fluid. Although it still cannot satisfy the inviscid condition, the energy lost in the granular debris is considered to be only slightly different within a streamline.

For this reason, the Bernoulli’s principle was applied for a granular debris flow study (*2.7.4 The work of Hotta*). Inferring from the raw data Figure 3-6, the total energy of one test (rps=1.3 with 4mm glass beads) along the cross section is derived as Figure 3-7.

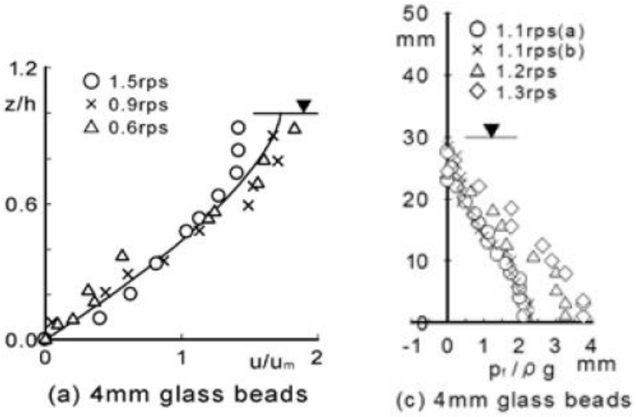

Figure 3-6 Raw data, velocity profile (left) and excess water pressure profile (right) (Hotta 2011)

The velocity profile of 1.3 rps is inferred from the data between 0.9rps and 1.5 rps.

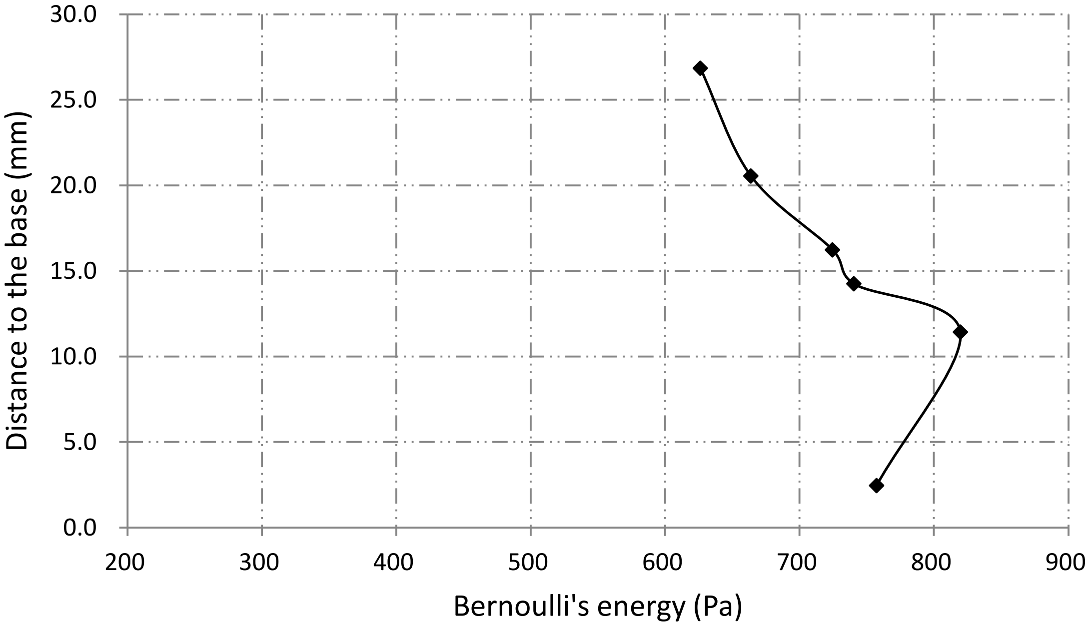

Figure 3-7 Bernoulli’s energy along the vertical cross section

Figure 3-7 shows the energy streamline along the vertical cross section of an experiment carried out with a rotating mill. The 30mm depth is the flow surface; the 0mm is the bottom of the rotating mill. Plugging in the raw data into equation 4-1, the total energy of different depth is derived as the curve line. As predicted, the energy does not vary much from different depth. Additionally, the figure indicates a trend that the energy is slightly decreasing from the bottom to the top.

Explanation to the decreasing trend would be that this measuring section is not a constant streamline of the flow. In the rotating mill apparatus, the energy is gained from the shearing of the bottom part (the shearing of the rotating apparatus' motion and the fluid), and due to the friction between the glass beads and water, the energy is decreasing from the bottom to the free surface.

Due to the unavailability to measure the velocity of the fluid with the apparatus in this thesis, the author does not perform further analysis on the performing tests. But still, the concept of the energy conservation may be a possible way to build connection of the flow velocity and water pressure for granular debris flow.

3.3. Apparatus configuration

3.3.1. Rotating drum

The rotating drum can be viewed as a flat cylinder as Figure 3-8. The cylinder has a radius of 25cm and 10cm width. A transparent wall was made in one side of the cylinder that the movement of debris simulation can be observed. In the middle of the wall, a hollow-carved circle with a radius of 11cm was made. This hollow circle allows for the simulation material to be put in or moved out. In addition, a movable bar with pore pressure sensor was set in the cross section.

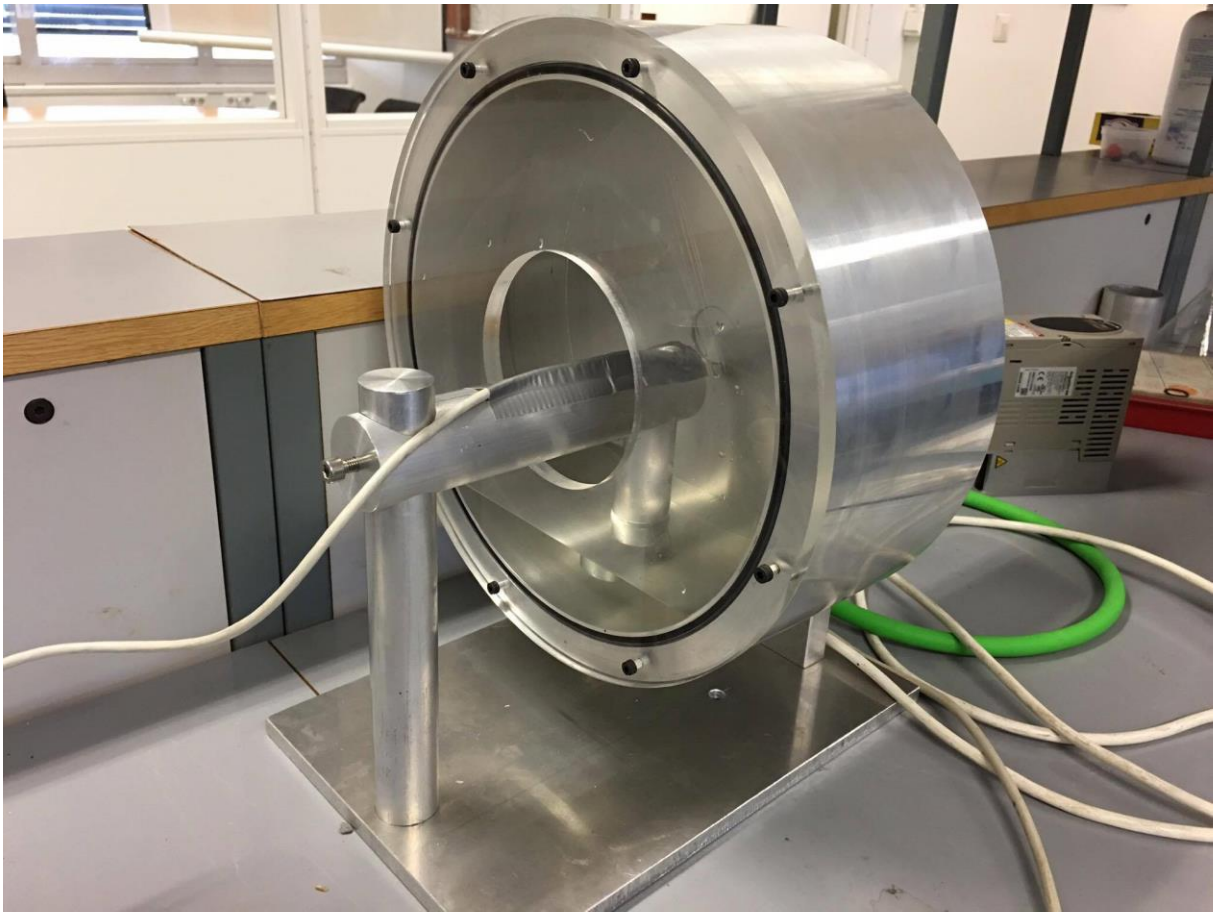

Figure 3-8 Rotating drum

3.3.2. Pore pressure measurement

The pore pressure measurement system is a movable water-proof metal bar with a sensor installed inside the base of the bar. This design replaces another design that the bar is equipped with four sensors installed at the sides. In a trial test those sensors were under influence of direct impact of the flow and particles, giving poor measurement result.

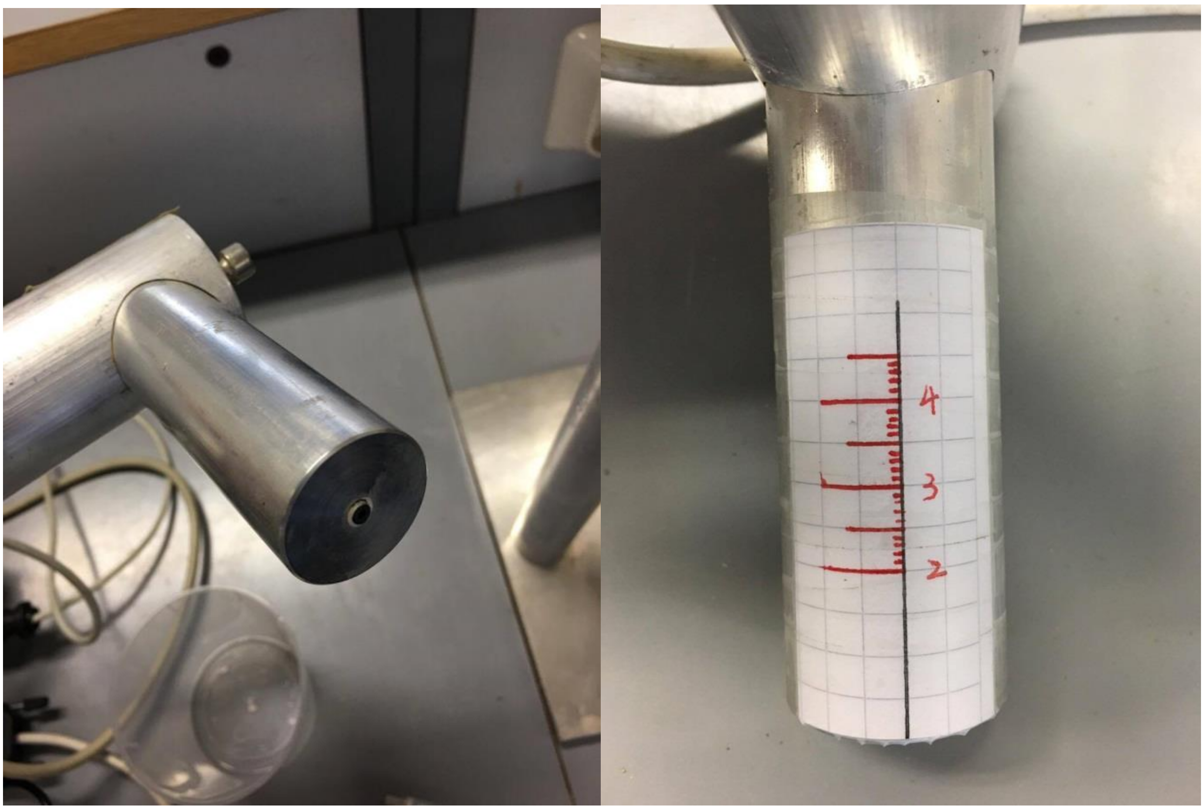

Figure 3-9 Pore pressure measurement system

Figure 3-9 shows the sensor installed in the base of the bar. A manually made calibration was pasted on the bar for a rough verification of the flow depth. The calibration is suggested to be improved by using the laser measurement in the future study. The pore pressure measurement needs to be corrected twice with this equipment. Once the controlling program starts, the measurement needs to be set to zero. In the measurement, the sensor gives a value that is 100~150Pa greater than the actual value. Depends on the estimation of the initial pure water flow depth the deviation can be corrected in the analysis.

3.3.3. Controlling program

The controlling program is working on the Labview2014. The program is used to control the motor and the pore pressure measurement. To perform the experiment in this thesis, the auto mode is first written with increasing velocity to produce the steady flow, and pore pressure is recorded during the motion.

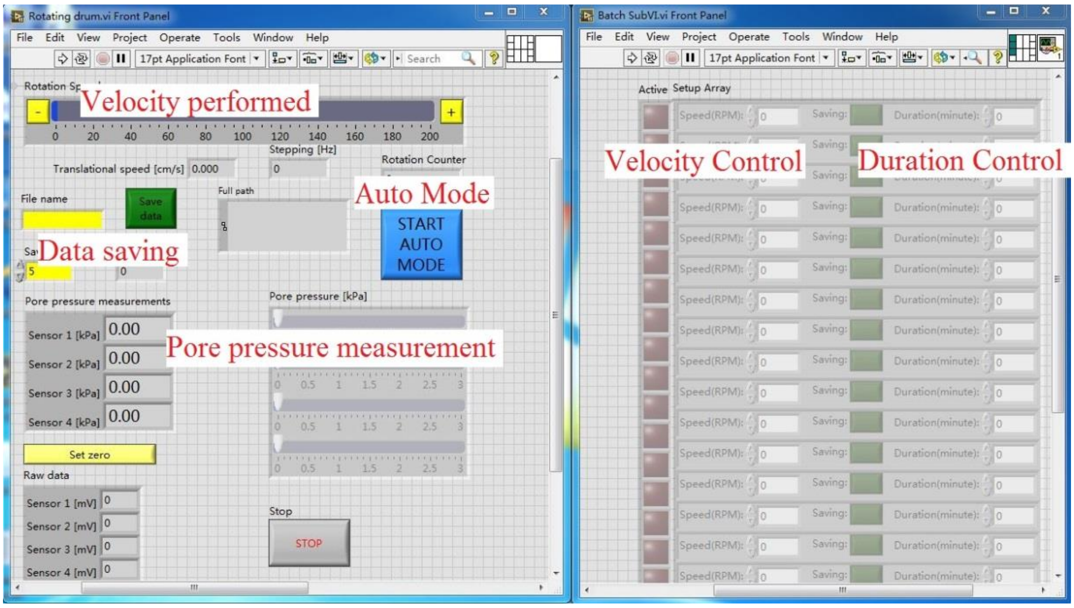

Figure 3-10 Controlling program

The collected data can be collected and analyzed by using Excel. The program is initially for the four sensors measurement bar and therefore records four sets of data. In this experiment, only the data from sensor 1 is analyzed. The water pressure is initially recorded in kPa.

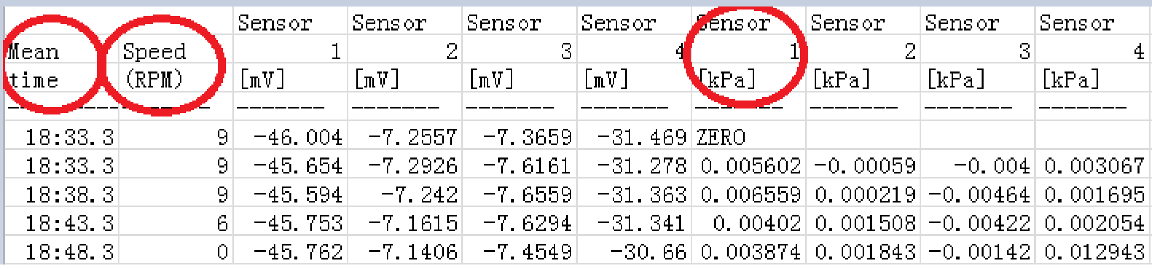

Mean time	Speed (RPM)	Sensor 1 [mV]	Sensor 2 [mV]	Sensor 3 [mV]	Sensor 4 [mV]	Sensor 1 [kPa]	Sensor 2 [kPa]	Sensor 3 [kPa]	Sensor 4 [kPa]
--------	--------	--------	--------	--------	--------	--------	--------	--------	--------
18:33.3	9	-46.004	-7.2557	-7.3659	-31.469	ZERO			
18:33.3	9	-45.654	-7.2926	-7.6161	-31.278	0.005602	-0.00059	-0.004	0.003067
18:38.3	9	-45.594	-7.242	-7.6559	-31.363	0.006559	0.000219	-0.00464	0.001695
18:43.3	6	-45.753	-7.1615	-7.6294	-31.341	0.00402	0.001508	-0.00422	0.002054
18:48.3	0	-45.762	-7.1406	-7.4549	-30.66	0.003874	0.001843	-0.00142	0.012943

Figure 3-11 Data recording

3.4. Test material

A mixture of sands and moraine silt is taken as the test material. The sand sample is from a master student who is also performing debris flow experiment by performing miniature flume tests (Laache 2016). Same material is chosen for the future possibility to build connection for both studies. The grain density was derived by using a calibrated pycnometer.

Figure 3-12 Test resource, sand (left) and moraine silt (right)

The test samples are mixture of the above material with ranging silt content. The naming of the tests is S0, S20, S33, S40, S50, S80 and S100. The number indicates the percentage of the weight of silt content in the total weight of the grains. E.g., S80 means the weight of the silt is 80% of the weight of total grains. All test samples are saturated with the same volume of water, namely with a concentration of 50%.

Test sample calculation

The goal of the test sample calculation is to control all samples with the same appropriate volume that can be properly set in the apparatus, producing a steady flow and preventing any mass spilling over during the motion. Based on the apparatus geometry, it is decided to have the sample reach around 4.5cm depth in the channel. The estimated area and volume of the mixture is thereafter calculated and summarized as the Table 3-1 bellow. Additionally, the specific density of the sand and silt are also involved.

Table 3-1 Geometry and specific density

Depth (h, cm)	4.5
Area (A, mm^2)	5066
Width (d, mm)	100
Total volume (V, cm^3)	500
Sand density (ρ_1, g/cm^3)	2.71
Silt density (ρ_2, g/cm^3)	2.65
Water density (ρ_w, g/cm^3)	1

With a total volume V and sediment concentration by volume of 50%, the volume of soil V_s and the volume of water V_w can be derived as:

$$V_s = V * 50\% \tag{3.10}$$

$$V_w = V * (1 - 50\%) \tag{3.11}$$

Define the weight of the sand and the weight of the silt as W_1 and W_2, with respective density ρ_1, ρ_2 and the total weiht W_s.

$$W_s = W_1 + W_2 \tag{3.12}$$

$$W_i = \rho_i * V_i, \tag{3.13}$$

$$V_s = V_1 + V_2 \tag{3.14}$$

Depends on the silt content percentage of the sample:

$$W_2 = (W_1 + W_2) * silt\% \tag{3.15}$$

The weight of the sand and silt can be further derived as:

$$W_1 = V_s * \rho_1 * \rho_2 * (1 - silt\%) / \{\rho_2(1 - silt\%) + \rho_1 * silt\%\} \tag{3.16}$$

$$W_2 = (W_1 * silt\%)/(1 - \mathrm{silt}\%) \tag{3.17}$$

The density of the mixture ρ_t can be therefore described as:

$$\rho_t = (W_1 + W_2 + W_w)/\mathrm{V} \tag{3.18}$$

Based on the solution above, the test samples are summarized as Table 3-2, and the grain size distribution is summarized as Figure 3-13.

Table 3-2 Summary of the test sample calculation

	S0	S20	S33	S40	S50	S80	S100
Sediment concentration (C,%)	50	50	50	50	50	50	50
Volume of Soil (Vs,cm3)	250	250	250	250	250	250	250
Volume of Water (Vw,cm3)	250	250	250	250	250	250	250
Silt content by weight (%)	0	20	33	40	50	80	100
Ratio of the weight of Silt/Sand	0.00	0.25	0.49	0.67	1.00	4.00	/
Weight of Sand (W1,g)	677.5	539.6	450.6	402.9	335.0	133.1	0.0
Weight of Silt (W2,g)	0.0	134.9	221.9	268.6	335.0	532.4	662.5
Weight of Soils (Ws,g)	677.5	674.4	672.5	671.4	669.9	665.4	662.5
Weight of Water (Ww,g)	250.0	250.0	250.0	250.0	250.0	250.0	250.0
Total weight of the mixture (Wt, g)	927.5	924.4	922.5	921.4	919.9	915.4	912.5
Density of the mixture (ρ, g/cm3)	1.86	1.85	1.84	1.84	1.84	1.83	1.83

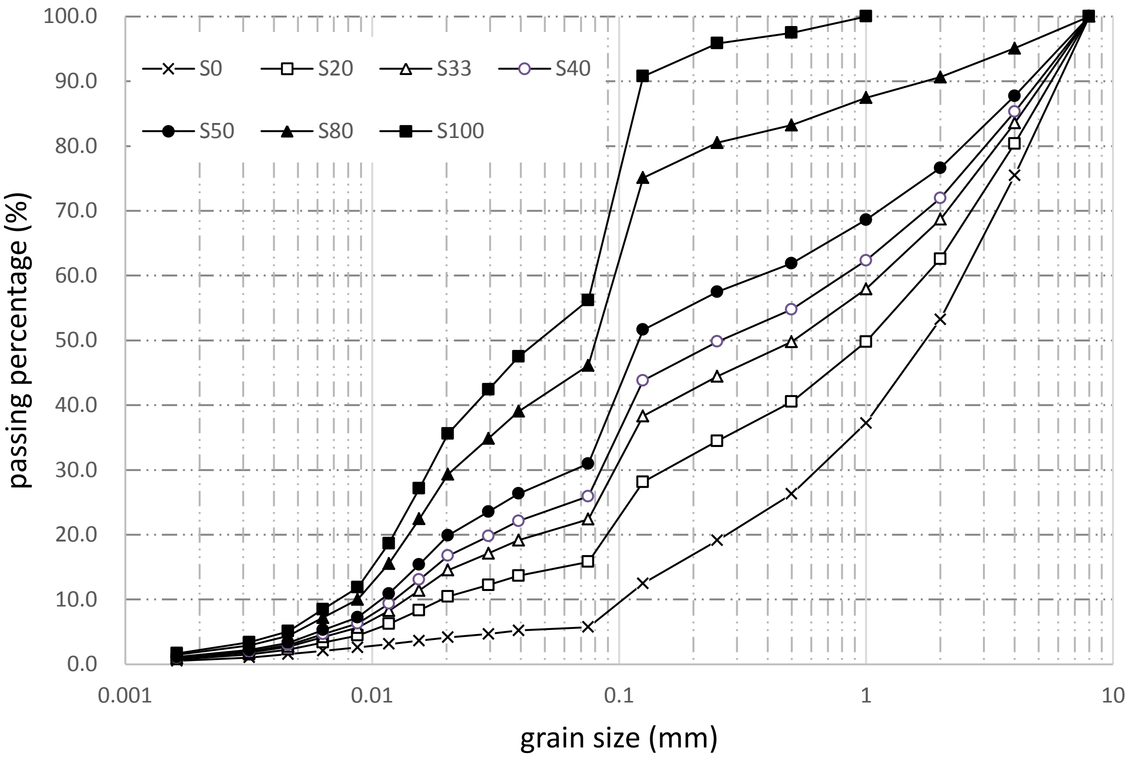

Figure 3-13 Grain size distribution of test sample

3.5. Experiment’s procedure

For the purpose of measuring the pore pressure in the moving debris with the rotating drum apparatus, the following experiment procedure is proposed to perform the test:

- Calculate the needed weight of the soil grains (sand and silt respectively) and water according to 50% solid fraction concentration by volume and different silt content.
- Put the soil grains and distilled water in the apparatus. Turn on the apparatus and run it on 60 RPM. This is to ensure the sample is saturated and being homogenous.
- The saturation process lasts for 10 minutes.
- Perform sensor calibration. Put the sensor bar in the proper vertical direction and set the pore pressure value as 0 as the initial value.
- Stop the motor and insert the sensor bar into the shear zone of the debris. Being aware of the danger that the sensor bar cannot get in touch with the apparatus or being stuck with the sand if it is inserted too deep, it is suggested to insert to a depth of 2.5cm.
- Record and observe the pore pressure change. The insertion of the sensor bar would bring up the disturbance. Wait until the water pressure does not change anymore, that it is close to the hydrostatic value.
- Start testing. The auto mode (Figure 4-6, *chapter 4.1.4 Rotating inertia and auto mode program*) will gradually increase the speed and record the pore pressure for each velocity. The rotating velocity is controlled to run to maximum 60rpm. Otherwise the flow is no longer steady and fails to reproduce the true nature of the debris movement.
- After all profile is recorded, turn off the motor by decreasing the rotating speed in a few seconds and continue to record the dissipation process.
- Stop the recording when the pore pressure value does not change with time.
- Turn off the power supply of whole system. Move away the sensor bar, take out the debris material and clean up the apparatus.

4. Results and discussions

4.1. Apparatus evaluation

Before evaluating any test results, it is important to examine first whether or under which conditions can the apparatus reproduce the actual nature of the moving debris. This chapter involves the following issues that are most concerned from the observation.

4.1.1. Steady flow

The experiment aims to measure the pore pressure under different velocities in a steady flow, and a steady flow means the moving debris should flow in a steady laminar motion. To ensure the steady flow, there should be a rotating speed limit for the test program.

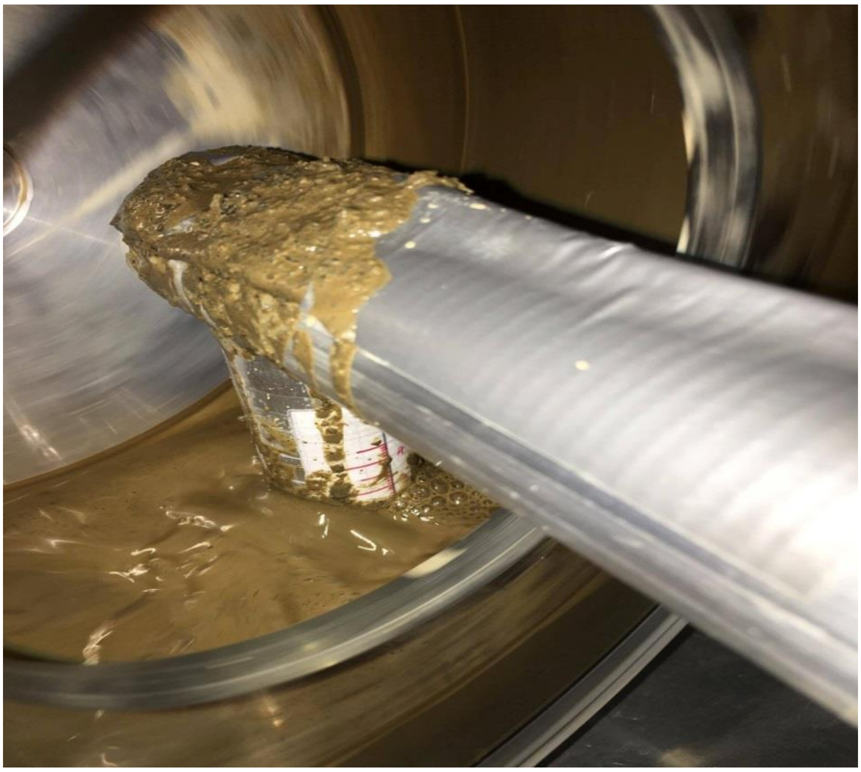

Figure 4-1 Unsteady flow – turn over and bubbles

Figure 4-1 shows the unsteady flow when the rotating speed is 70rpm. It has been observed that when the rotating speed is over 60rpm, part of the debris material will flow over, and air bubbles begin to take place around the sensor bar. Additionally, evaluation from *chapter 4.1.5 Sensor disturbance and sensitivity* indicates these air bubbles do not only take place around the upper part of the sensor bar, but also fill up the sensor opening and disturb the measurement.

Therefore, a speed limit of 60rpm (79cm/s) is determined based on observation on the flow property. This speed limit becomes the maximum speed in the auto mode program in *chapter 4.1.4 Rotating inertia and auto mode program*.

4.1.2. Debris grain size grading

It should be pointed out the simulation is on the shear zone of the moving debris. The mixture is simulated as a shear element of the shear zone, rather than a miniature moving debris. Therefore, the grading situation here is not the grading of the whole moving debris' profile, and it is not appropriate to compare this one with the grading profile of the whole debris (*Figure 2-2, chapter 2.3 Composite*).

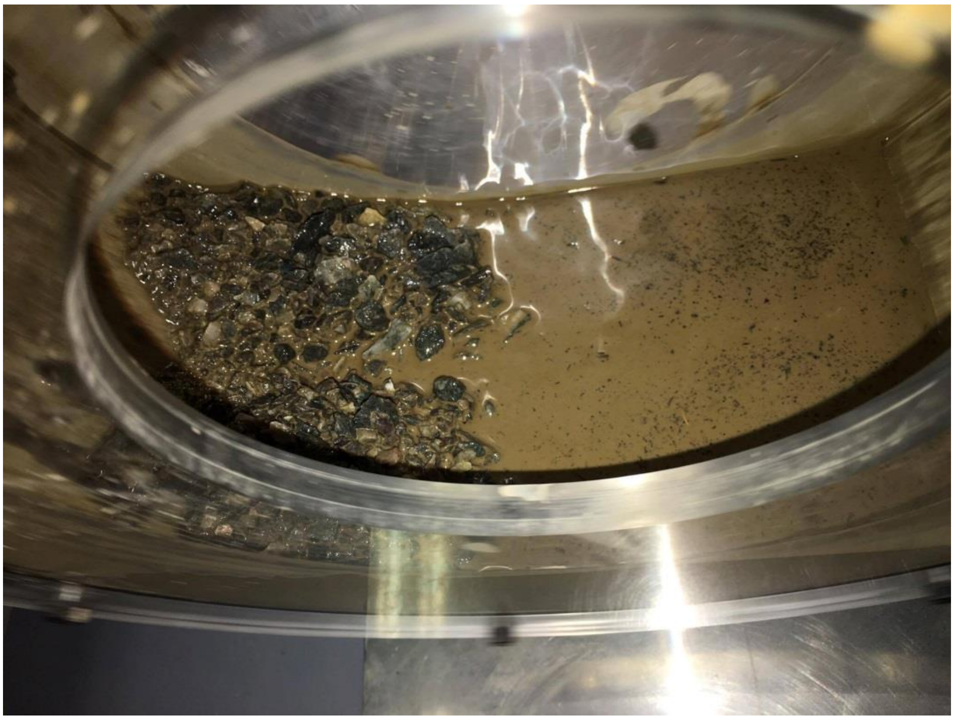

Figure 4-2 Debris material grading

Figure 4-2 shows a grading situation of test S40. Two phases can be observed, the coarse grain phase and the fine grain phase. The coarse grains were dragged to the back of the flow, because of the friction between the coarse grains and the apparatus. The measuring section is in the fine grain phase. This grading situation can be compared with the literature study *(chapter 2.7.4 The work of Hotta).*

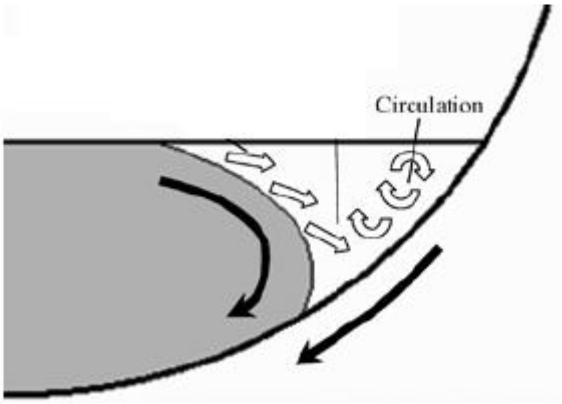

Figure 4-3 The grading situation of granular debris flow simulation (Hotta 2011)

Figure 4-3 shows the grading situation in the Hotta's experiment. In this experiment, the test material is plastic/glass balls (1~6mm) and water. The plastic/glass balls are taken as granular debris material, and two phases were observed during the motion. The granular phase (in black) and the water phase (in white) were observed to be clearly separated, with opposite directions of circulation.

The grading situation is therefore similar to the situation in the literature study. Here the water phase is not only pure water, but also with fine grains involved. Based on this grading situation, the pore pressure measurement bar is inserted in the fine grains phase (a little deviated from the center line). This prevents the collision of sandy particle with the sensor, yielding more reliable measurement result.

4.1.3. Roughness on the side walls

The flowing channel of the apparatus has a width of 100mm, and the confined wall has considerable roughness during the debris motion. Besides the flow circulation in the flow direction as Figure 4-3, two circulations also exist near the side channel walls.

Figure 4-4 Two circulations caused by the roughness of the side wall

This is different from the actual debris flow. Considering a short moment that the actual debris flow flows down in a short time, there should not be such a confinement and circulations as the Figure 4-4. However, the roughness of the side wall should have a less significant influence on the fine grains phase, where the solid to solid contact is less crucial. Based on observation, no obvious circulation can be observed in the fine grains part. Therefore, it can be assumed that influence of the roughness of the side wall on the shear zone is less significant.

4.1.4. Rotating inertia and auto mode program

Because of inertia, the measurement of the pore pressure will be disturbed for a time period when the rotation speed is changed. This disturbance could be crucial especially when the velocity level is low (e.g., from 0 to 2rpm). The dissipation process is also disturbed when the rotating speed decreases from 60rpm to 0 in a short time. To arrange the correct auto mode program to measure the water pressure with increasing speed, it is a practical issue to know how long it takes before the pore pressure measured is the correct water pressure under different speed.

For the change of low speeds (0-2rpm, 0-4rpm and 4-6rpm), a test was performed to measure the pore pressure in a sufficient period after the speed was changed. For 0-2rpm and 2-4rpm, the test was performed for 600 seconds, and 120 seconds for 4-6rpm. The test sample is S33.

Figure 4-5 shows the result. It coincides with the assumption that the inertia disturbance is significant in the change of low speed. For 0-2rpm change, the disturbance lasts for around 400s. The measurement shows great disturbance in the beginning 200 seconds, that the pore pressure is measured up to 60Pa higher than the stable value. For 2-4rpm change the disturbance lasts for about 50 seconds, and for 4-6rpm change the disturbance only takes place in the first few seconds.

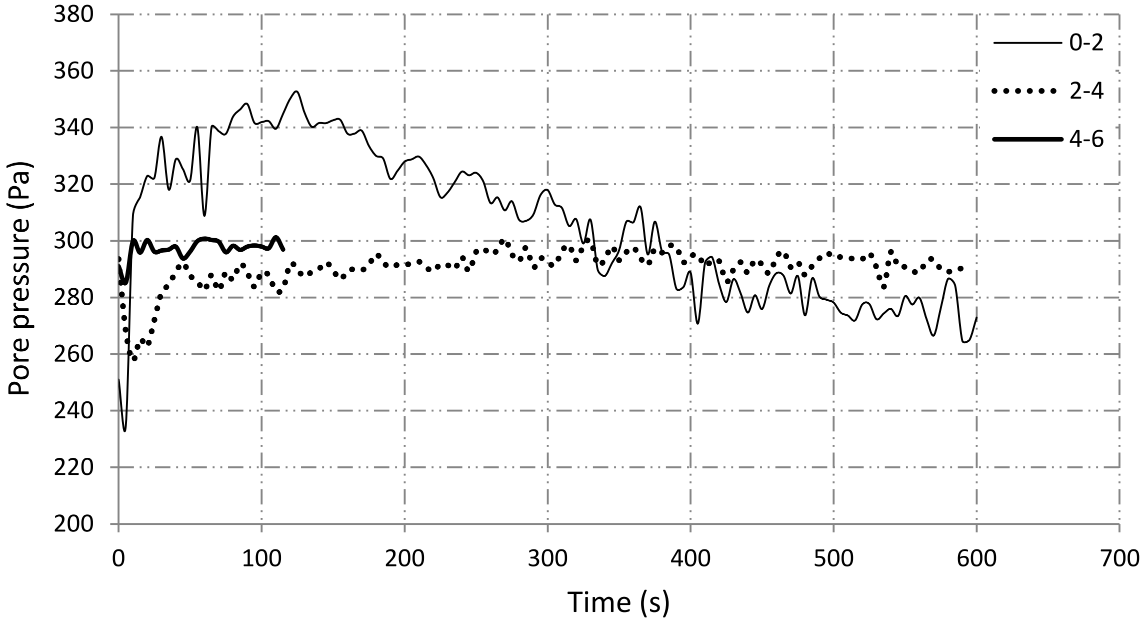

Figure 4-5 Test of inertia influence on low speed

An auto mode program is thereby determined based on the inertia disturbance test result as Figure 4-6. All measure periods sufficiently cover the useful data after the inertia disturbance, ensuring the analysis can be based on correct results.

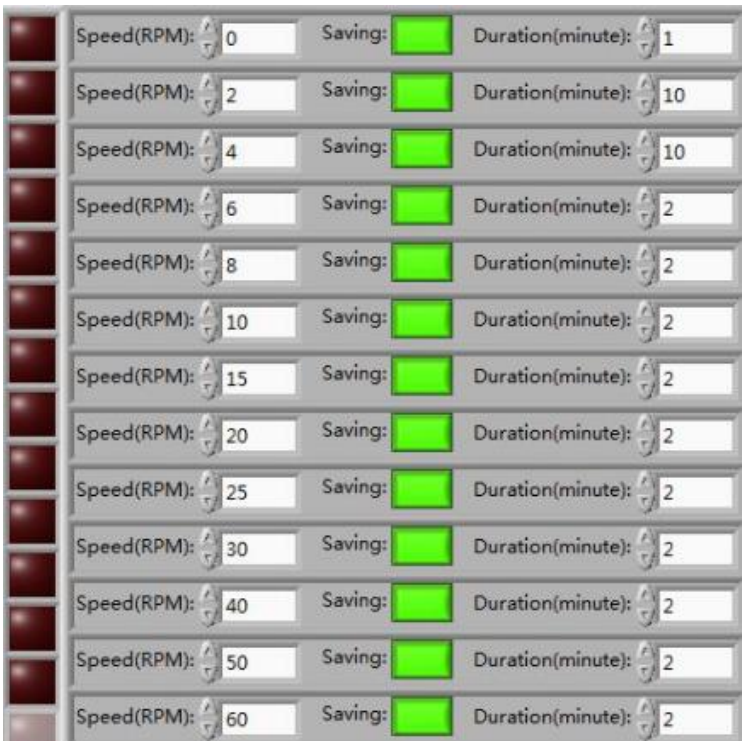

Speed(RPM): 0 Saving: 🟩 Duration(minute): 1
Speed(RPM): 2 Saving: 🟩 Duration(minute): 10
Speed(RPM): 4 Saving: 🟩 Duration(minute): 10
Speed(RPM): 6 Saving: 🟩 Duration(minute): 2
Speed(RPM): 8 Saving: 🟩 Duration(minute): 2
Speed(RPM): 10 Saving: 🟩 Duration(minute): 2
Speed(RPM): 15 Saving: 🟩 Duration(minute): 2
Speed(RPM): 20 Saving: 🟩 Duration(minute): 2
Speed(RPM): 25 Saving: 🟩 Duration(minute): 2
Speed(RPM): 30 Saving: 🟩 Duration(minute): 2
Speed(RPM): 40 Saving: 🟩 Duration(minute): 2
Speed(RPM): 50 Saving: 🟩 Duration(minute): 2
Speed(RPM): 60 Saving: 🟩 Duration(minute): 2

Figure 4-6 Auto mode program

4.1.5. Sensor disturbance and sensitivity

It is important to evaluate how much disturbance of the insertion of the sensor bar. The sensor bar has a diameter approximately of 25mm, which is very considerable in the 100m width channel. In the literature study *(chapter 2.7.4 The work of Hotta)*, a pitot tube of 1.5mm was used in a width of 40mm channel.

Figure 4-7 The sensor bar and its insertion

The sensor bar design in this apparatus is obviously too large. In fact, the wires connected to the sensor are very small in diameter (1~2mm), and it is not necessary to use the large water-proof metal material to cover it. But due to the time and experience limit in the workshop, this design was practiced in the experiment. The main influence of the large size of the sensor bar are splitting the continuous flow into two side flows aside the sensor bar, and arouse the turbulent condition around the sensor placement (in the bottom of the sensor bar). The negative effect of these is not further analyzed, though the results from the experiment still yield a good match with the literature study.

Bubbles are found to appear around the sensor when velocity is over 60rpm. These bubbles are formed because of the sharp angle of the corner. When bubbles are formed, they cause serious disturbance to the pore pressure measurement. They disturb the proper contact between the sensor and the flow fluid, and cause suction during the dissipation process. The suction is so significant that the measured pore pressure value can even be lower than the hydrostatic pore pressure. Therefore, as stated in *chapter 4.1.1 Steady flow*, a steady flow is necessary to prevent the bubble appearance. All tests are performed in relatively low rotating speeds, ensuring proper measurements of the sensor.

Figure 4-8 Bubbles around the sensor (left)

The sensitivity of the sensor is up to 15Pa. It is a result from the pure water test (*chapter4.2 Pure water test*). Additionally, the sensor also has a reading correction from 100~150Pa. E.g., in a depth of 2cm water, the original reading may vary from 300~350Pa. Therefore, a calibration value is made in every test according to the variation of the initial pore pressure measurement value and the height of the insertion depth.

4.1.6. The change of flow depth during motion

In theory, the flow depth is changing in different rotating speeds. In a steady flow, the flow depth decreases with increasing flow distance due to increasing shear rate. But in practice, the flow depth is not changing significantly from physical observation. In addition, a pure water test was performed to see the indication of the change of flow depth by measuring pore pressure in different speeds. The result (*chapter4.2 Pure water test*) only shows a few Pascal difference.

Although the result from the pure water test shows the change of flow depth is very limited, it cannot prove the change of flow depth may be neglectable in this study. Since the flow behavior varies much from the pure water when the flow becomes more viscous (with more silt content), the flow depth in viscous flow can be significant. But since flow depth measurement is not available in this thesis, it is still taken as a constant value in the calculation. Be that as it may, the changing of the flow depth should be considered in future study.

Another factor that influences the flow depth is the grain size distribution of the test samples. The flow depth may change much when the sample consists of more coarse grains. During the motion, coarse grains gather in the back part of the flow, and some may rise above the water level. This will significantly decrease the flow depth with increasing velocity.

4.2. Pure water test

A pure water test was performed before the main test program. The speed level of pure water test is according to the auto mode (Figure 4-6, *chapter 4.1.4 Rotating inertia and auto mode program*). Because of rotating inertia disturbance in the beginning part of each speed level, the analyzed pore pressure data was chosen from the last one minute data.

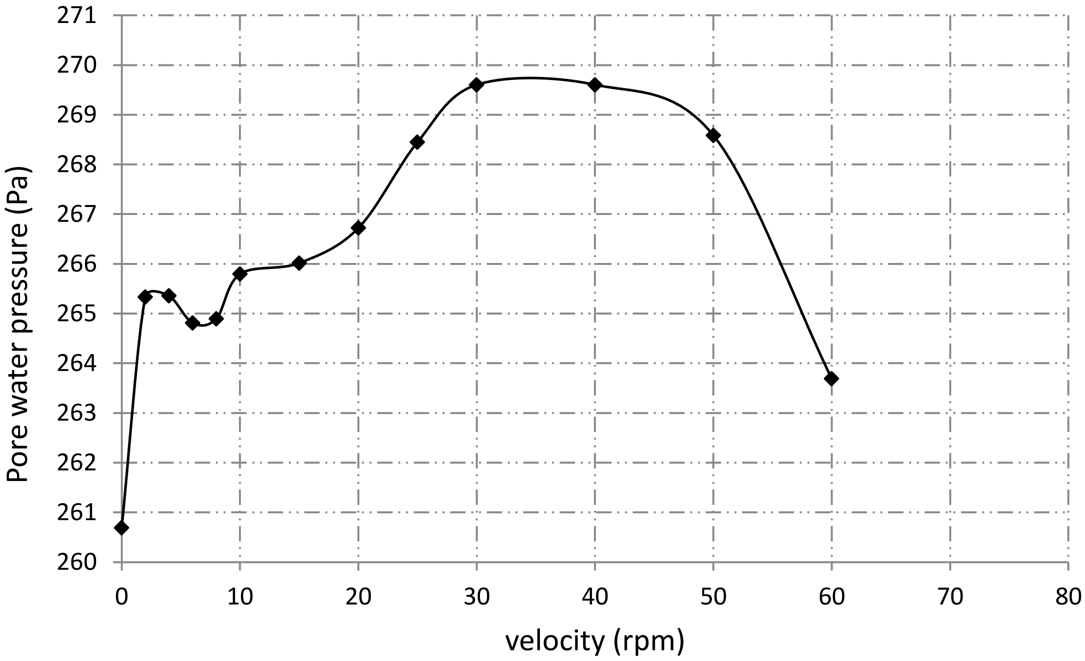

Figure 4-9 Pure water test

Figure 4-9 shows the results of pure water test. The insertion depth is approximately 2.6cm, a very common insertion depth in the test program. The figure shows the change of the pore pressure during motion is very limited. Since the data is taken from the last one minute, the flow is steady without much pressure change. The change of the pore pressure can therefore be viewed as an indication of the change of flow depth. Approximately 10 Pa change shows 1mm change of the flow depth.

The result of the pure water test gives a rough verification that the apparatus and pore water sensor are working properly. The change of pore pressure in different velocity, however, cannot be used as a flow depth correction for different speeds in the test program. Since different sample have different grain size grading, the change of the flow depth should be different from the pure water test.

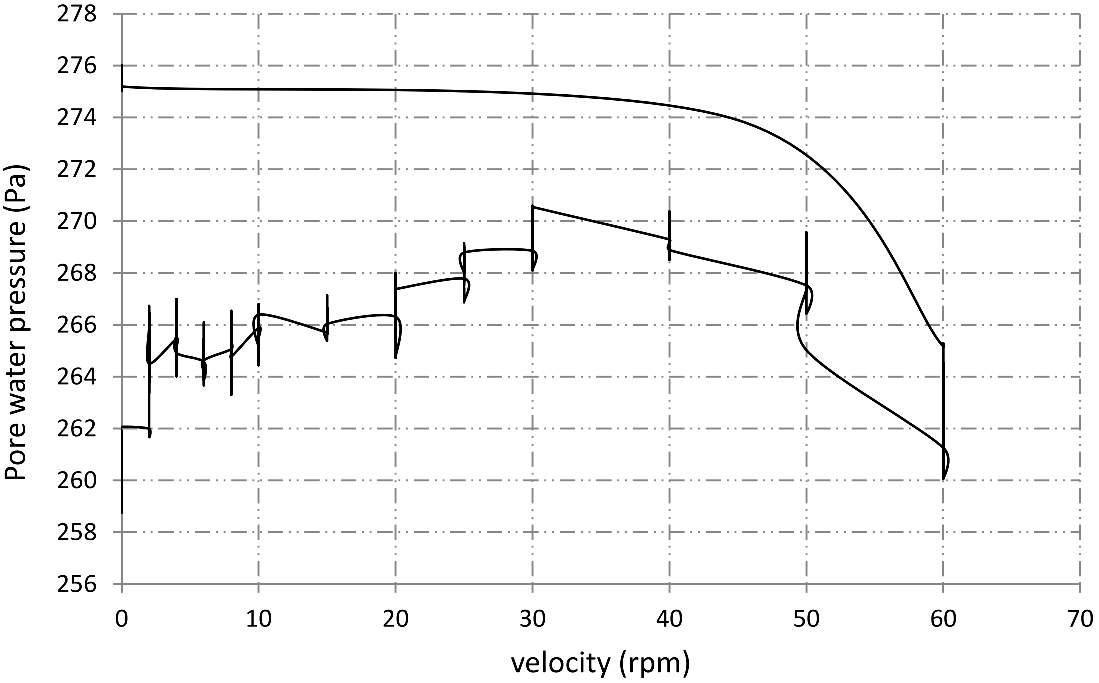

Figure 4-10 Raw data, pure water test

Figure 4-10 shows the raw data of the pure water test. Inertia disturbance can be observed in every change of the speed level. The most important result of the raw data tells the sensor does not give the same pore pressure value of the initial flow depth, after the test was finished. The test started with 259Pa and ends in 275Pa. The deviation gives approximately 15Pa sensitivity of the pore pressure measurement.

The accuracy of the sensor is considered to be not too bad. 15Pa deviation is similar to the hydrostatic value of 1.5mm flow depth. The measuring flow depth is 25mm in general; the 5% sensitivity is acceptable. Besides, the excess pore pressure built-up value is much higher than this sensitivity value. Results show that the excess pore-pressure can be up to 150Pa and even more in some tests, proving the sensitivity of the sensor is less significant.

This sensor sensitivity problem also occurs in some tests of the main test program. In those cases, the floating ratio would be ended around 10%, which is further corrected by taking the final measurement as the initial hydrostatic water pressure into calculation.

4.3. Excess pore pressure build-up

Figure 4-11 summarizes the excess pore pressure build-up of all tests. The figure gives a general idea of how the excess pore pressure is generating in each test, but it is not appropriate to compare the results within different tests. The insertion depth of the sensor bar (flow depth) is different in different tests because of different grading situations (*Chapter 4.1.6 The change of flow depth during motion*), and the excess pore pressure measured is at different flow depth in different tests.

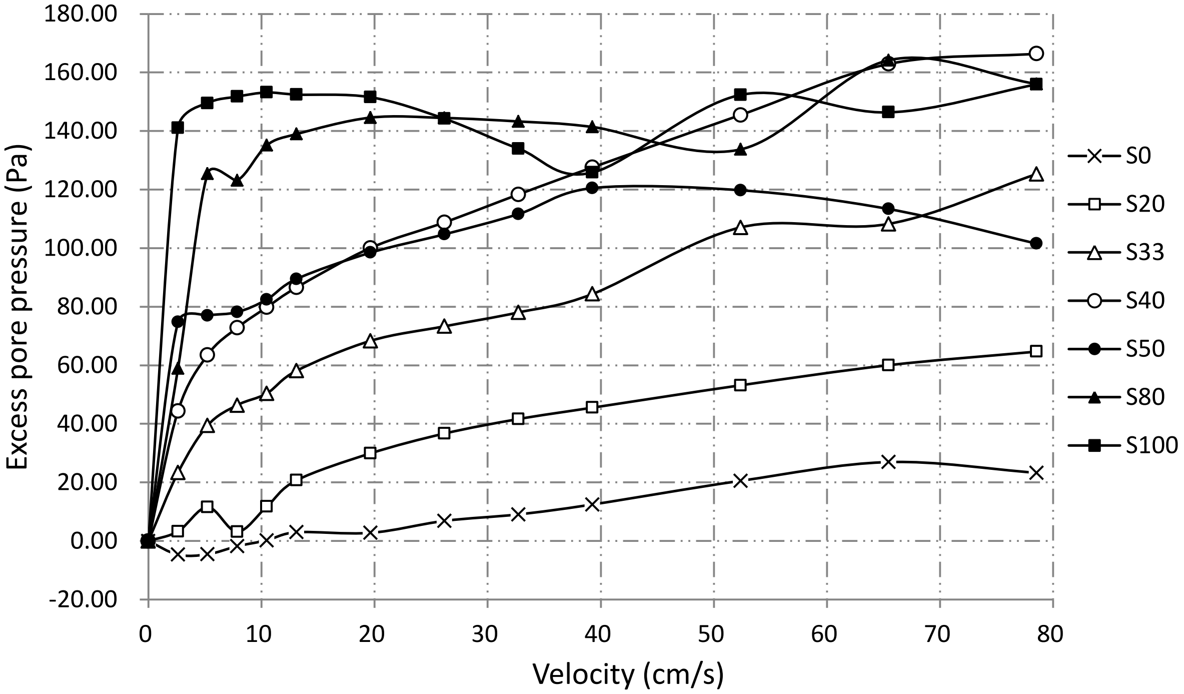

Figure 4-11 Excess pore pressure

The negative value of S0 can be explained as the result of decreasing flow depth. S0 is the sample with barely silt content, and result shows very limited excess pore-pressure even in very high speed. The negative pore pressure value here is actually not because of suction, but the decreasing hydrostatic value due to the decreasing flow depth. During the motion, the coarse material tends to gather in the back of the flow, lowering the water table in the measuring section. *Chapter 4.1.6 The change of flow depth during motion* explains the decreasing flow depth is neglectable in most of the tests, as the value is very small compared with the excess pore-pressure triggered by the floating fine grains.

The situation for S0 is unique. First, because excess pore pressure is barely built up, the change of the flow depth (the change of the hydrostatic pressure) relatively becomes more significant. Second, because S0 consists of much coarse grains, the grading situation is very considerable and the change of the flow depth can no longer be neglectable. Due to these two reasons, the calculation based on the unchanged flow depth is of the least accuracy for S0.

For samples with considerable silt content, S80 and S100 shows a fluctuate part in a higher speed. Explanation would be that the grain size of these two samples is too fine, and the floating fine grains are not being able to move with the relatively high velocity any further. For fine grains, a very considerable floating state is achieved in a relatively low speed.

In high speed, the actual flow velocity cannot follow the rotating speed of the apparatus. This situation is similar to the literature study (*Chapter 2.7.1 The work of Sassa*, Kyoji). In the coaxial cylinder study, the point E shows the mixture is not able to move with the rotating rods, being subjected to shear and the pore pressure decreases(Wang and Sassa 2003).

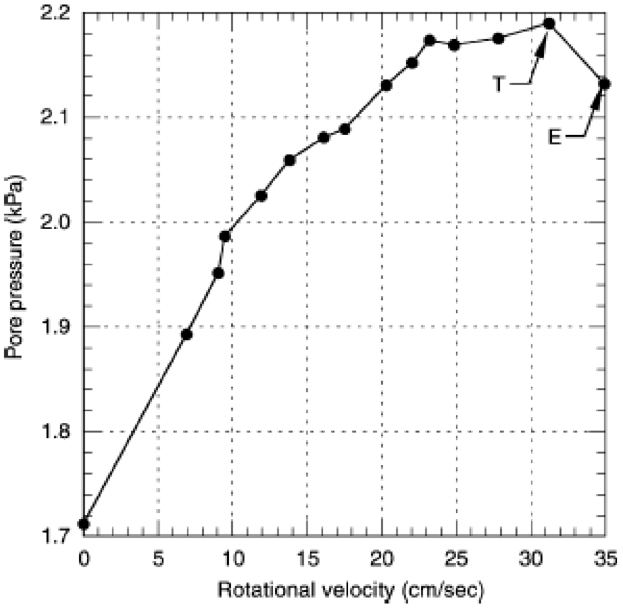

Figure 4-12 Decreasing point E (Wang and Sassa 2003)

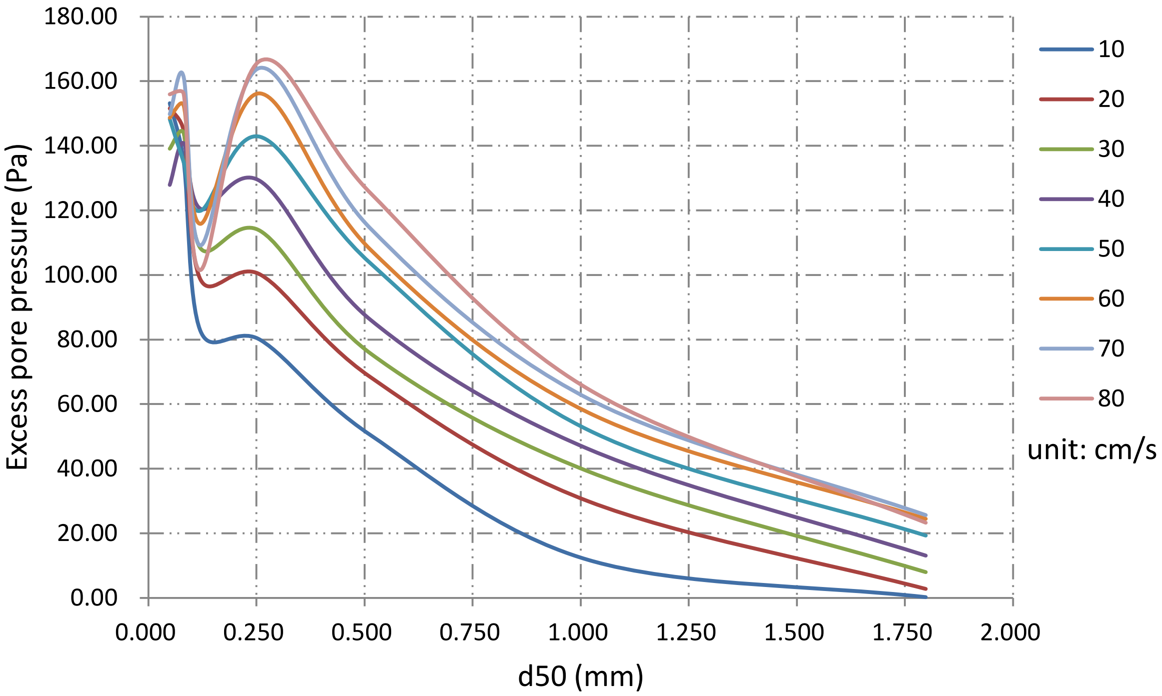

Figure 4-13 Excess pore pressure – d50

Figure 4-13 concludes the empirical result of the excess pore pressure built up in relates to the d50 under different rotating speeds. The development of the excess pore pressure is found to be significant dependent on the grain size. A decreasing trend of the excess pore pressure build-up is clearly shown with the increasing d50. The fluctuated beginning part is from S50 (d0.121), S80 (d0.082) and S100 (d0.050), the tests that cannot be considered to have a flow velocity the same as the rotating speed as stated above. Therefore, the velocity influence on the grain size smaller than S50 (d0.121) cannot be derived from the figure.

4.4. Floating ratio

Having derived the excess pore pressure, the floating ratio is calculated based on the theory in *chapter3.2.1 Floating ratio*. The floating ratio presents as a degree of the excess pore pressure built-up in the sample, and therefore it is appropriate to compare within different tests. Figure 4-14 shows the result.

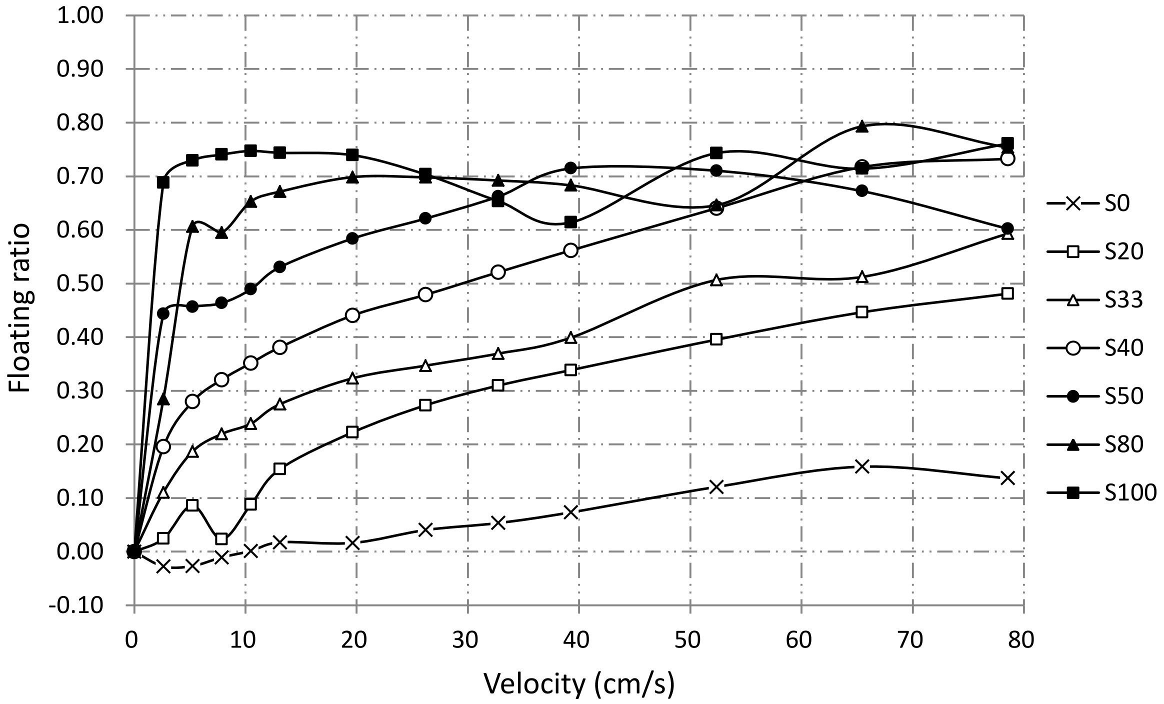

Figure 4-14 Floating ratio

Overall the patterns of all tests show a good match with each other. S0 develops the least excess pore pressure. Considering the decreasing flow depth it only generates around 10% excess pore pressure in the total stress. The silt sample S100 reaches the maximum around 75% floating ratio. The beginning part of the S50 is questionable, as the floating ratio develops even faster than the S80. The part remains to be further scrutinized.

The reason for the limited maximum floating ratio is the pore pressure sensor is inserted in the middle of the flow (2.5cm out of 4.5cm). Considering some content of fine grains are not available to float in the shallow part of the flow, the maximum floating ratio is therefore limited. Further comparison with literature study which measured the pore pressure in a lower part confirms this explanation. In theory, if the pore pressure sensor was installed near the bottom part of the flow, the floating ratio should be able to reach 1 for very fine-grained samples.

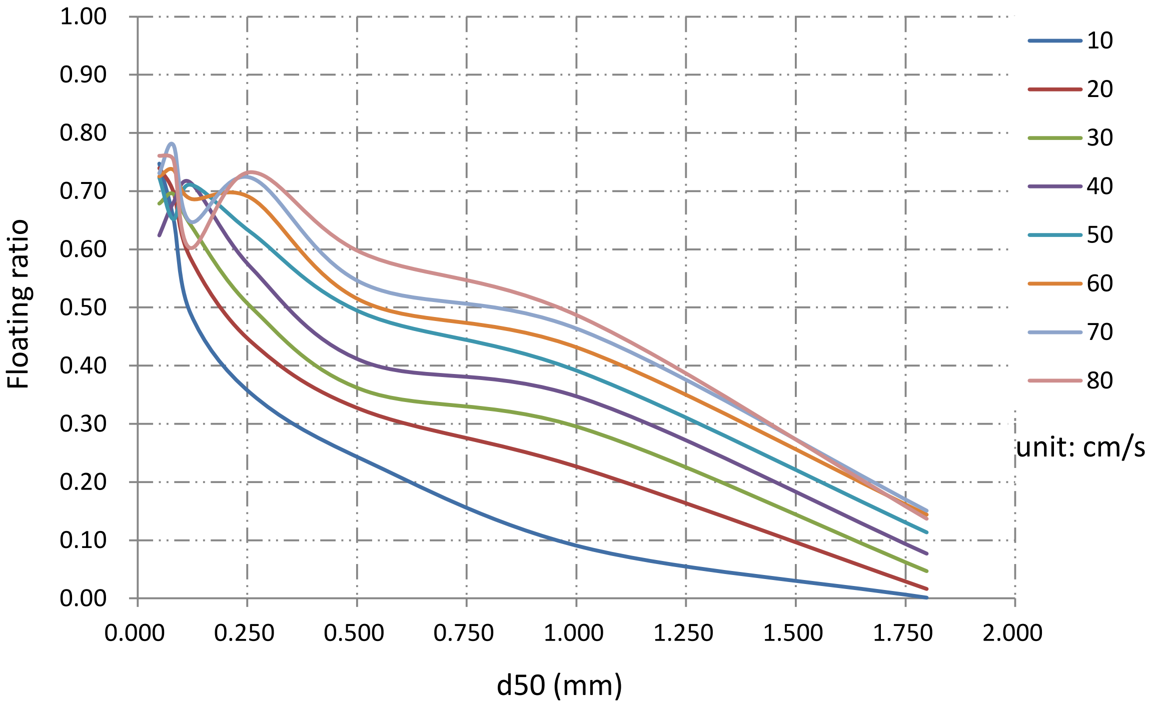

Figure 4-15 Floating ratio – d50

Figure 4-15 summarizes the floating ratio in relates to the d50 under different rotating speeds. Invalid result is observed for d50 in the fine range the same as Figure 4-13. The significance of the grain size is clearly revealed. For coarse d50, the floating ratio is limited and does not matter much in regards to the velocity. Although the finer d50 part is invalid, indication can still be that the sediment can reach a very high floating ratio in a very low speed. Considering this is the result of the middle part of the flow, the inclination of the curves could be steeper for the whole profile (measured in the basal layer).

4.5. Dissipation

The dissipation process begins after the rotation stops. The rotation was stopped manually in a few seconds to prevent the inertia disturbance to a great extent. Figure 4-16 shows the dissipation result.

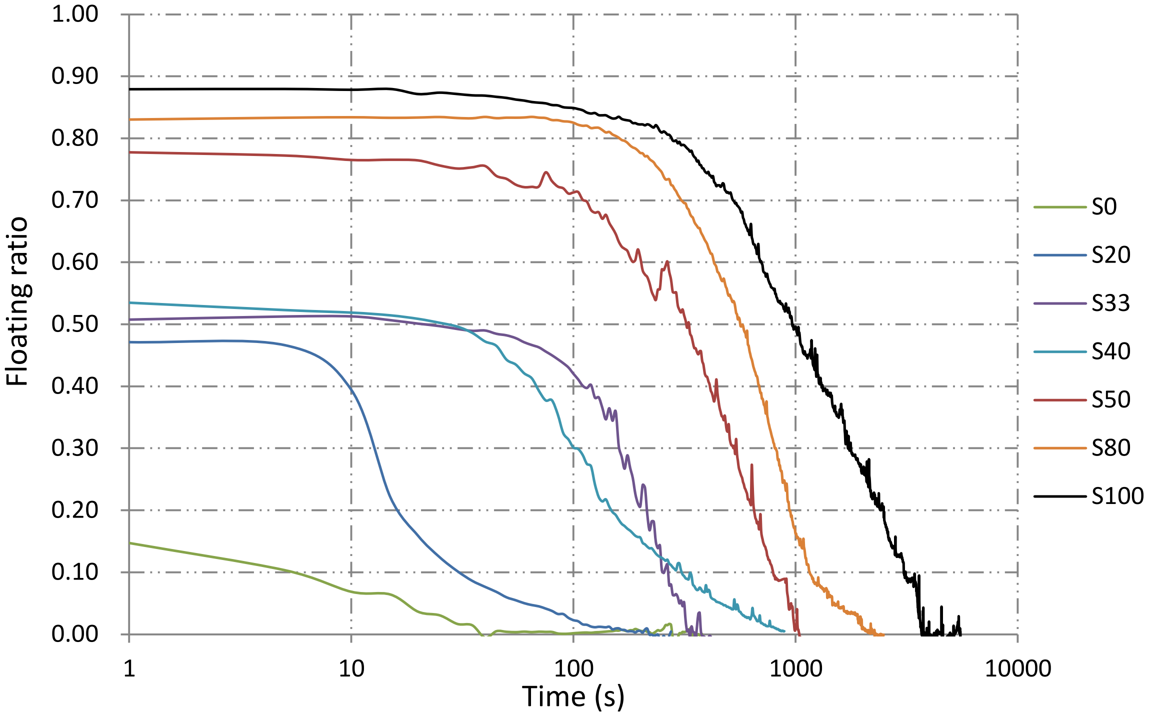

Figure 4-16 Dissipation – Floating ratio

Comparing within all tests performed, the results make sense as the final dissipation time and the dissipation pattern show a good similarity. For S40 and S33, the dissipation curves across each other, this may remain further scrutinized. But considering S40 and S33 are very similar in the grain size distribution, the result can be explained as a kind of deviation of sensitivity or accuracy of the measurement result.

The maximum floating ratio was maintained for some time for all tests besides S0, and the time increases with the silt content of the test sample. For S0, a typical granular sample that does not develop much excess pore pressure, the dissipation went very quickly in a few seconds.

The dissipation time is further illustrated in Figure 4-17 and Figure 4-18. They reveal the relationship between the dissipation time and the silt content/ median size diameter of the grain size.

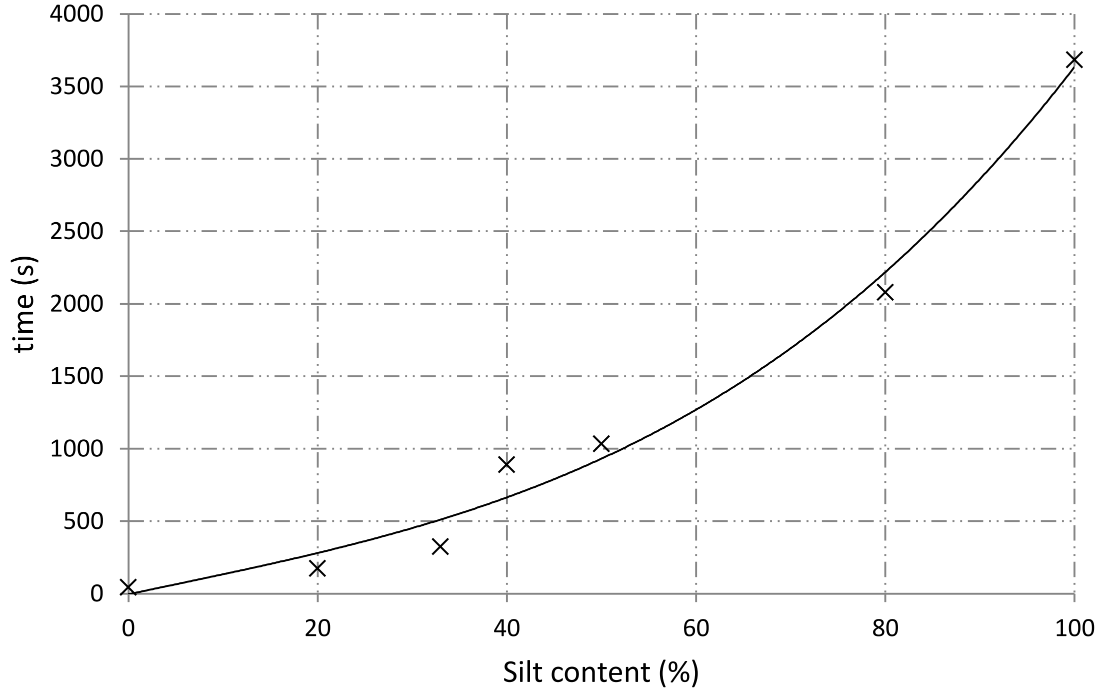

Figure 4-17 Dissipation – Silt content

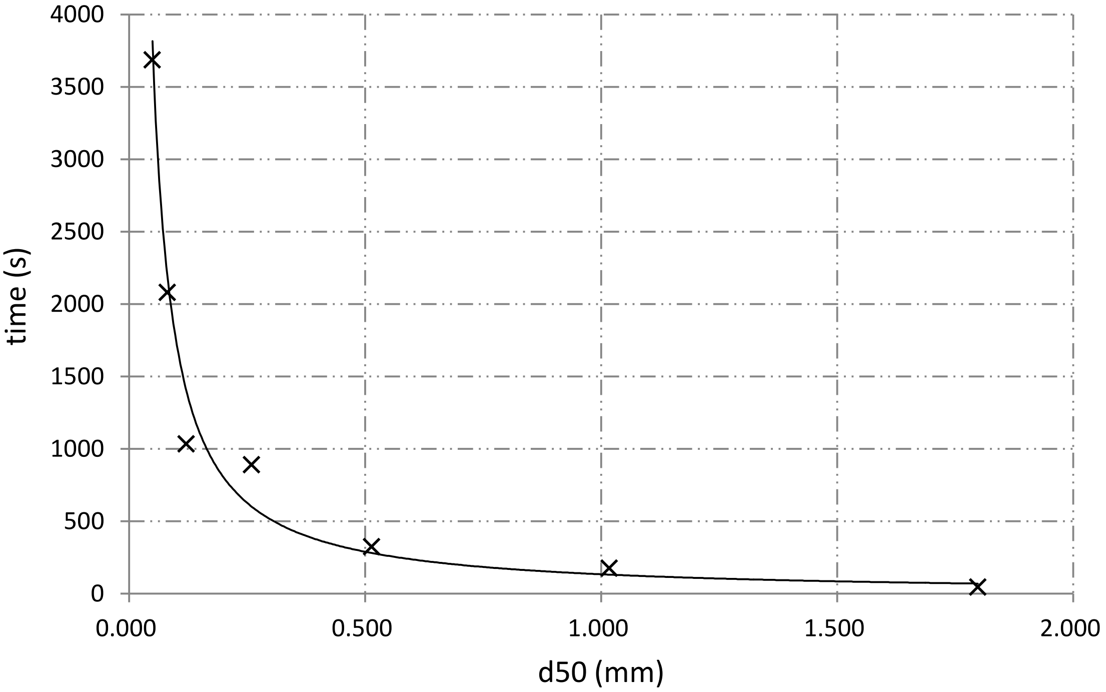

Figure 4-18 Dissipation – d50

Figure 4-18 clearly reveals that the fine grains are the key to the excess pore pressure dissipation. From S50 (d0.121) to S100 (d0.050), the dissipation time increases significantly. By comparison, the coarser d50 value shows the dissipation time is very short.

4.6. Comparison with literature study

The result of this study is further compared with literature studies (*2.7.1 The work of Sassa, Kyoji* , *2.7.2 The work of Yu, Xiang*).

4.6.1. Test program comparison

Before comparing the results, the difference of these three experiments should be introduced. Figure 4-19 shows the apparatus comparison (a full profile can be viewed in *Appendix*).

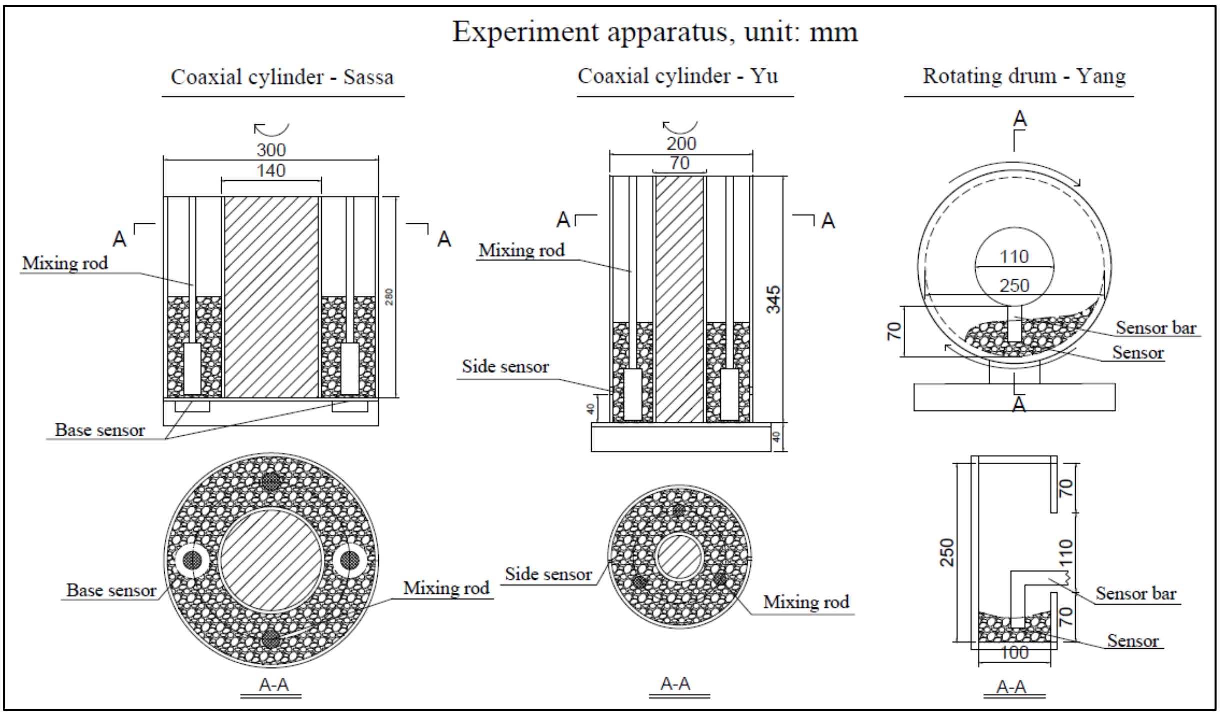

Figure 4-19 Apparatus comparison

The literature studies (Wang and Sassa 2003, Yu 2015) perform the experiment with coaxial cylinders. The cylinders are similar in size. The difference of the number of rotating rods does not matter much, since the function of the rods is to provide the flow with the same shear rate. An important part is the placement of the pore pressure sensor. In Sassa's study, the sensor was installed in the base. In Yu's study, sensors were placed both in the base and at the sides, but due to some reason only the data from the side sensors are in a good quality. In this study, the sensor is placed in the middle part of the flow. Due to the placement of the pore pressure at different flow depths (Sassa>Yu>Yang), it can be inferred that the result from Sassa should yield the highest maximum floating ratio for the same degree of fine grains.

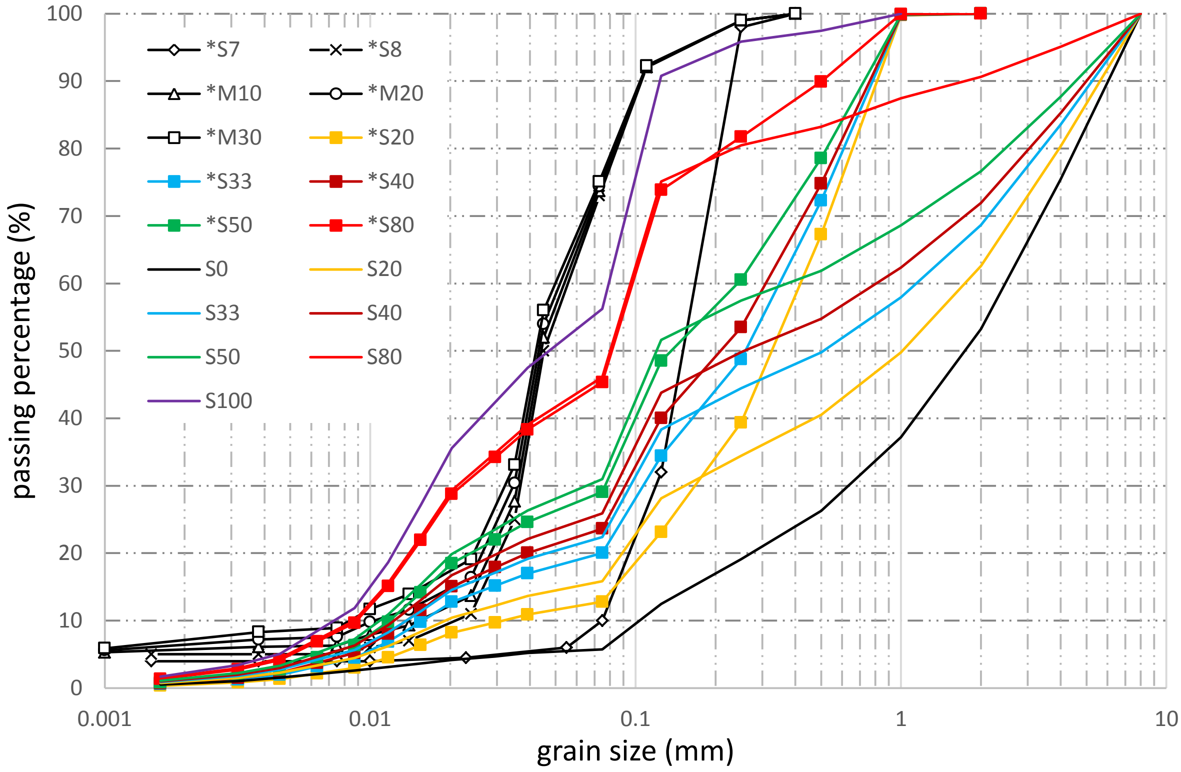

Figure 4-20 Grain size distribution comparison
(S0 - S100: Rotating drum – Yang; *S20 - *S80: Coaxial cylinder – Yu; *S7/ *S8/ *M10/20/30: Coaxial cylinder- Sassa)

For test samples, Figure 4-20 shows the summary of grain size distribution. The S series (S0 – S100) is the rotating drum apparatus in this thesis, the *S series (*S20 - *S80) is from Yu's study and the rest (*S7/ *S8/ *M10-30) are from Sassa's. While S and *S series have the concentration of 50%, the concentration performed in Sassa's study is much higher without detail specification. Samples from Sassa are formed by filling the water to the same height as the soil during the saturation. Two figures are also made to compare the test sample with two literature studies separately as bellow, and a full profile can be referred to *Appendix*.

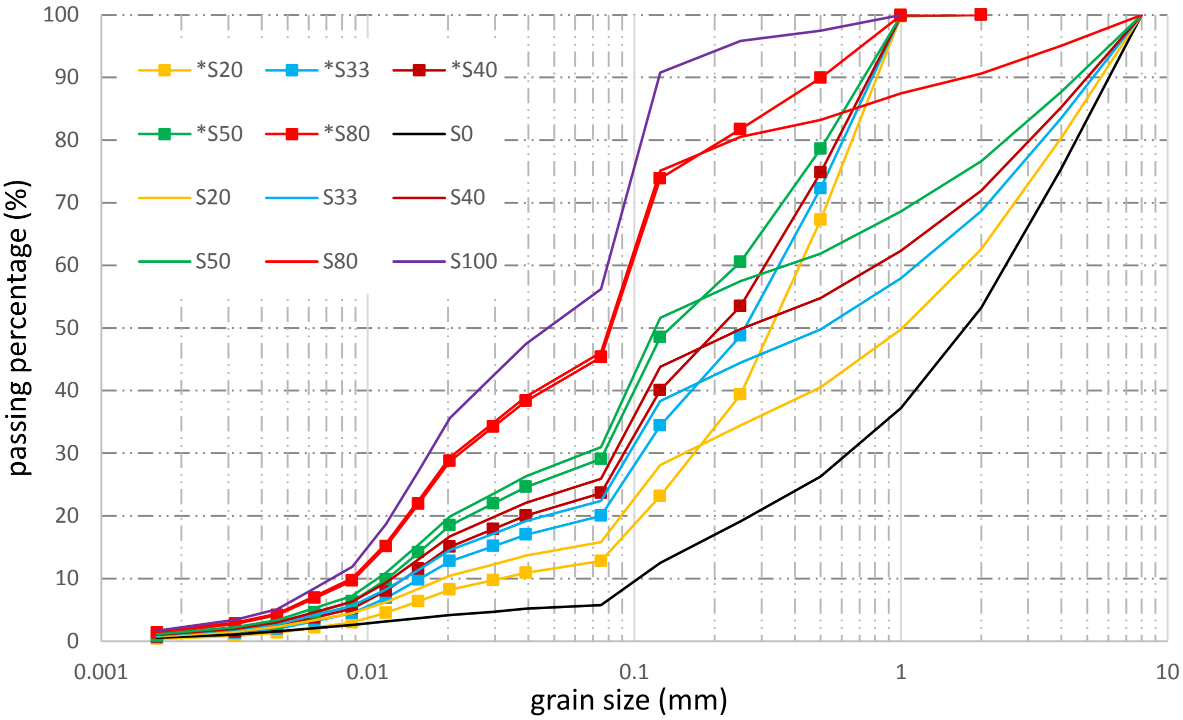

Figure 4-21 Grain size distribution comparison, Yang & Yu

(S20 - S80: Rotating drum – Yang; *S20 - *S80: Coaxial cylinder– Yu)

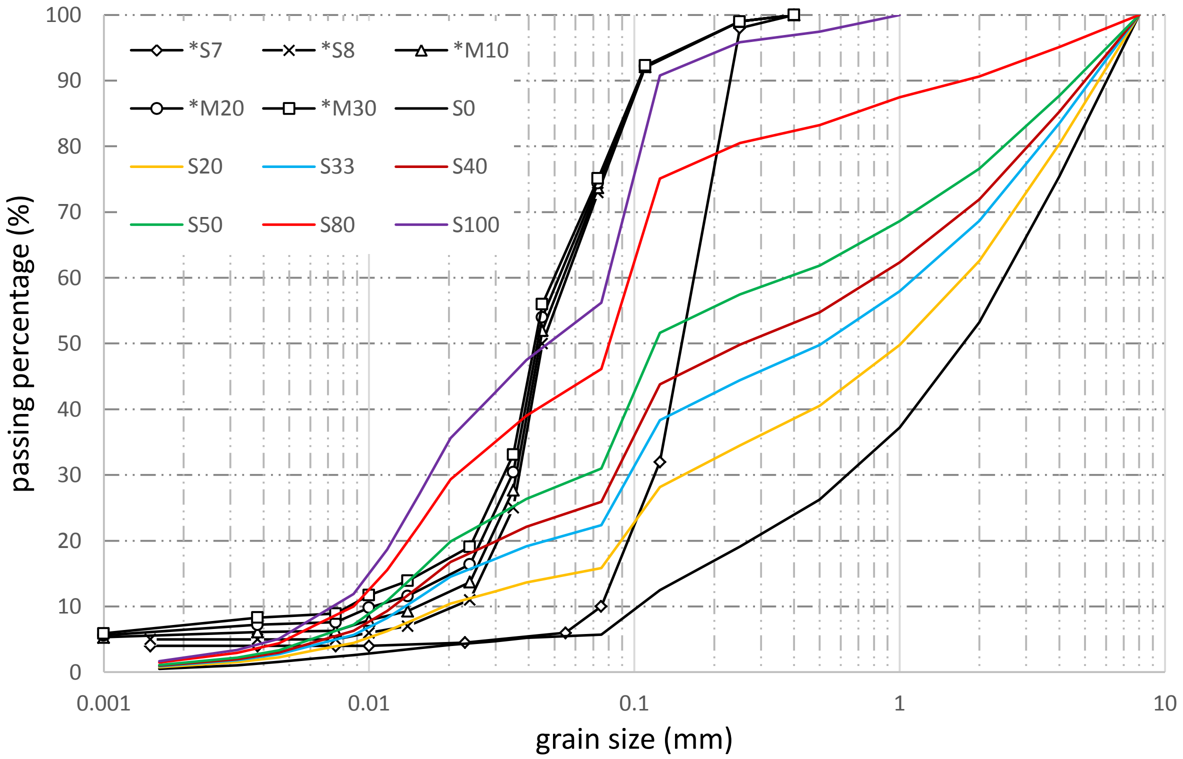

Figure 4-22 Grain size distribution comparison, Yang & Sassa

(S0 - S100: Rotating drum – Yang; *S7/ *S8/ *M10/20/30: Coaxial cylinder- Sassa)

In addition, a d50 table was made to summarize the test samples:

Table 4-1 d50 comparison

Sample (Yang)	d50	Sample (Yu)	d50	Sample (Sassa)	d50
S100	0.050	*S100	0.050	*M30	0.042
S80	0.082	*S80	0.083	*M20	0.043
S50	0.121	*S50	0.218	*M10	0.044
S40	0.260	*S40	0.260	*S8	0.045
S33	0.514	*S33	0.050	*S7	0.159
S20	1.017	*S20	0.345		

It should be stated the d50 is not used to illustrate the comparison study, as it fails to explain the fine grained content for some coarse samples. Figure 4-23 show the grain size of S20 and *S20. The fine grains are very similar in both curves, which indicate that they should have very similar patterns (floating ratio, dissipation) in the comparison. However, the d50 of S20 and *S20 vary much. Table 4-1 tells the d50 of S20 is 1.017, while the d50 of *S20 is only 0.345. Therefore, d50 is not used to illustrate any result of the comparison study, though it can be applied for some very fine samples.

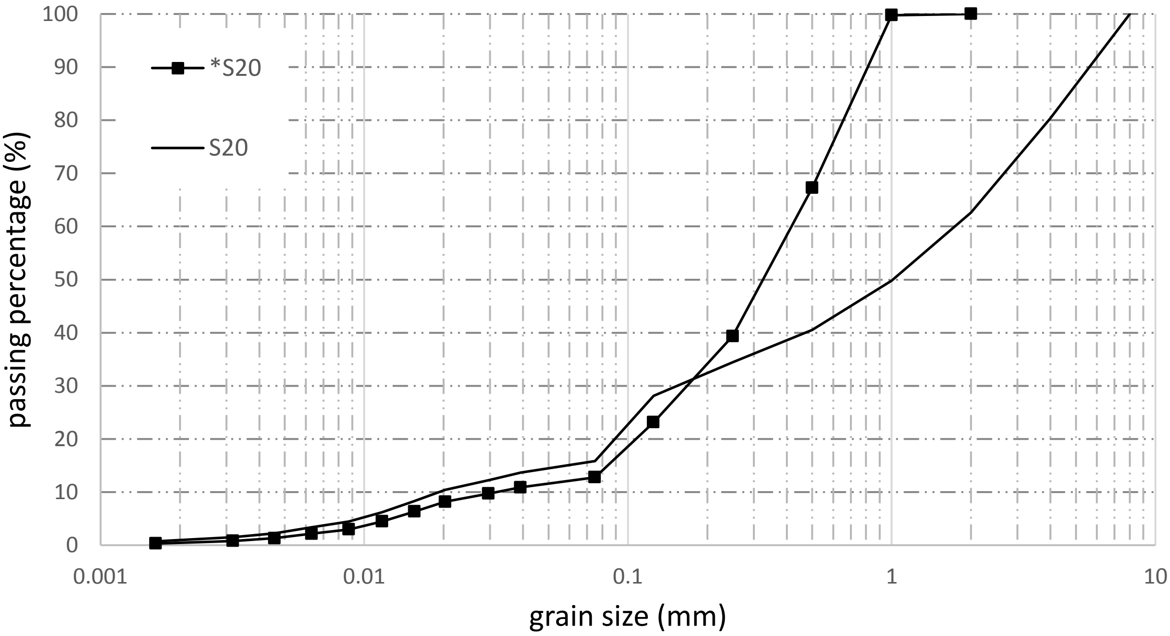

Figure 4-23 d50 of S20 & *S20

4.6.2. Floating ratio comparison

The floating ratio is compared in four groups: the low and high silt content comparison with Yu's and Sassa's study respectively. Figure 4-24 shows the first group – the low silt content floating ratio comparison with Yu's study.

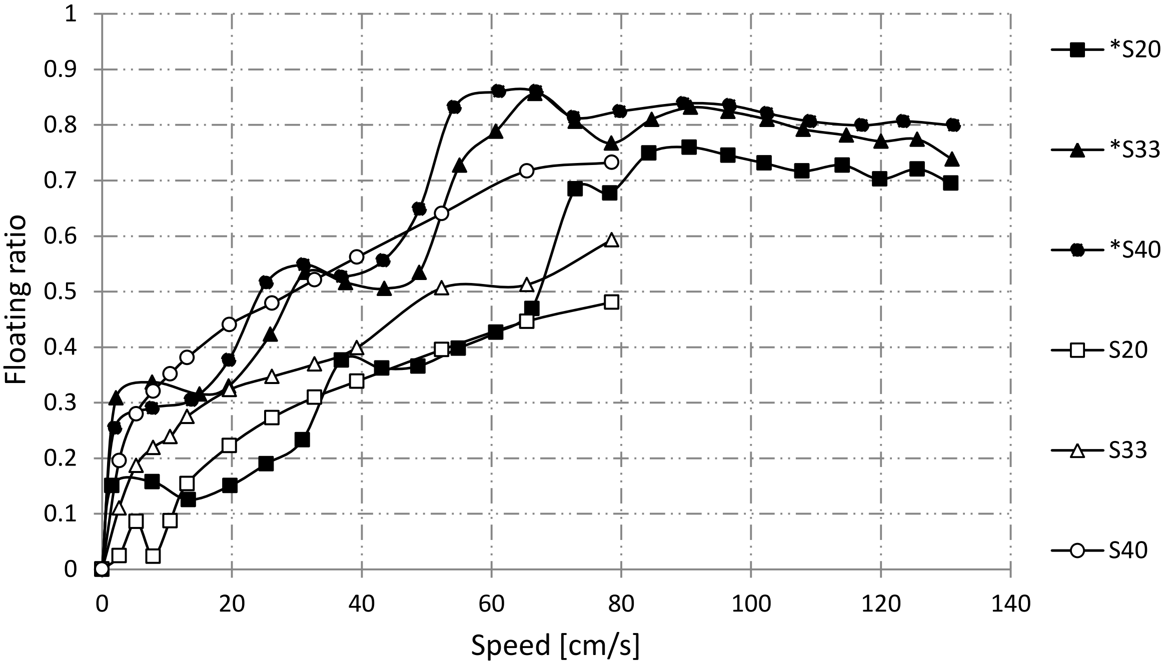

Figure 4-24 Low silt content floating ratio comparison, Yang & Yu
(S20/S33/S40: Rotating drum – Yang; *S20/*S33/*S40: Coaxial cylinder – Yu)

The relatively low silt content includes 20%, 33% and 40%. As stated in previous chapter, the fine grains content are very similar in both S and *S series. Therefore they yield very similar pattern. The *S series render a higher floating ratio than the S series, which proves the deduction in *Chapter 4.6.1 Test program comparison*. *S series measured the pore pressure in the lower part of the debris flow, and the S series measured the middle part. As a result, the lower part has more floating grains above its flow depth, resulting in a higher floating ratio.

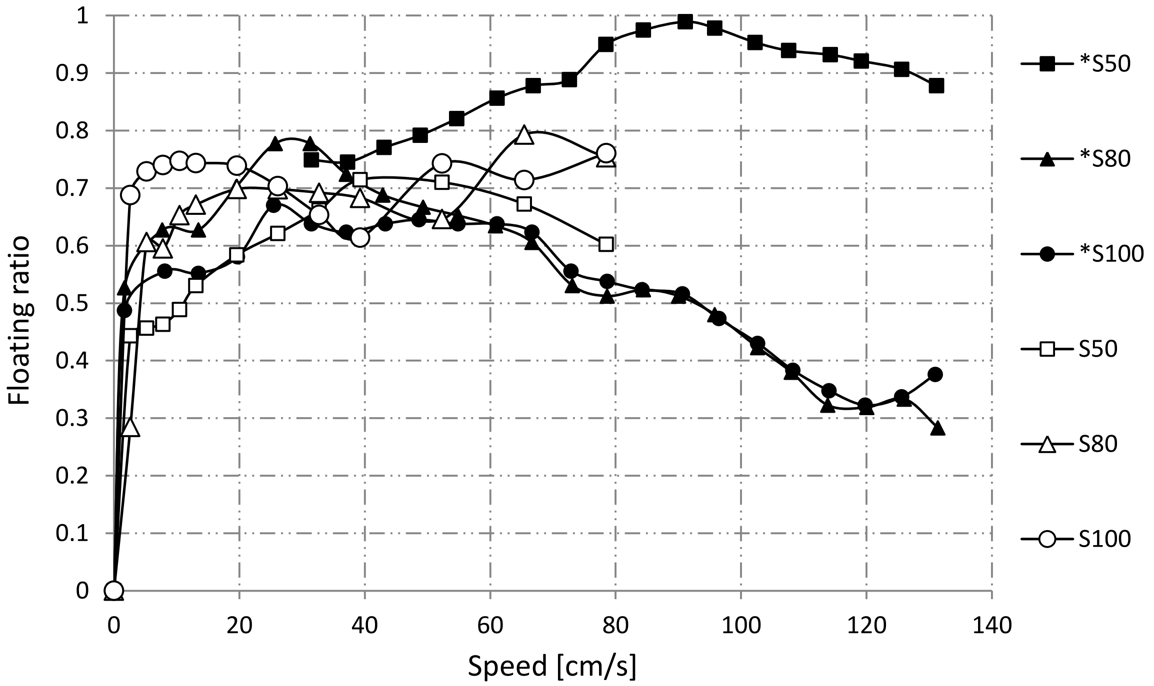

Figure 4-25 High silt content floating ratio comparison, Yang & Yu
(S50/S80/S100: Rotating drum – Yang; *S50/*S80/*S100: Coaxial cylinder – Yu)

Figure 4-25 shows the high silt content floating ratio comparison of Yu's study. It is noticeable that *S80 and *S100 from the coaxial cylinder failed to follow the rotating rods in high speed, while the rotating drum can still maintain the floating ratio at high speed. This indicates that the rotating drum apparatus provides more steady flow than the coaxial cylinder. Because of the failure at the high speed, the high silt content sample from Yu also fails to derive a good result for the dissipation test.

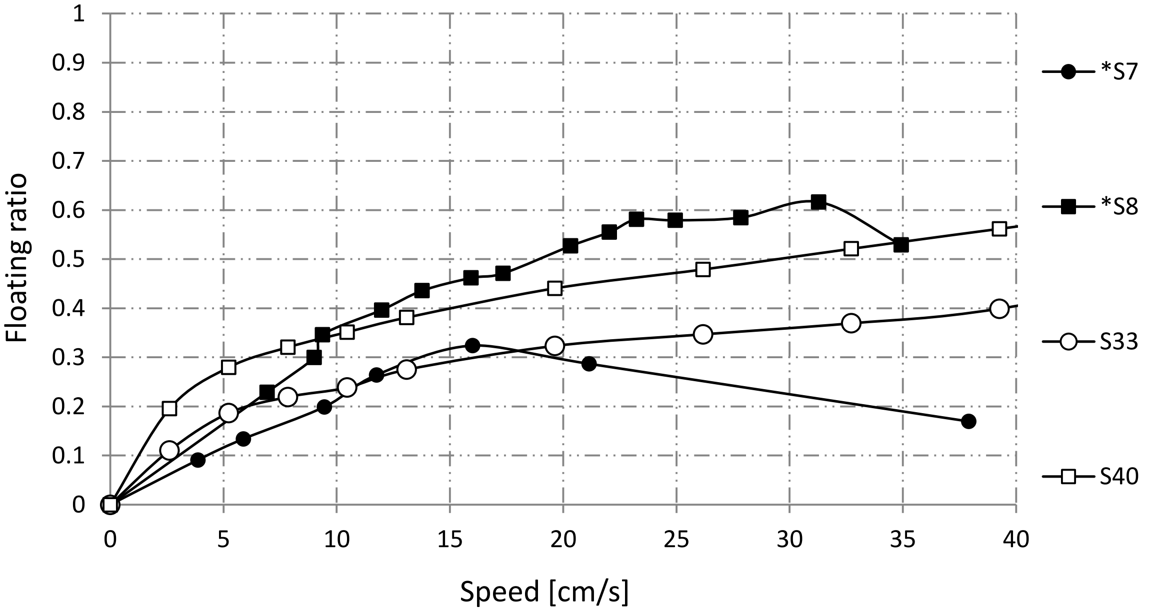

Figure 4-26 Low silt content floating ratio comparison, Sassa & Yang
(S33/S40: Rotating drum – Yang; *S7/*S8: Coaxial cylinder – Sassa)

Figure 4-26 shows the low silt content floating ratio comparison with Sassa's study. The *S7 and *S8 are coarse and fine silica-sand samples, and the result shows these two materials behave quite similar to the 33% and 40% silt content mixture in this study.

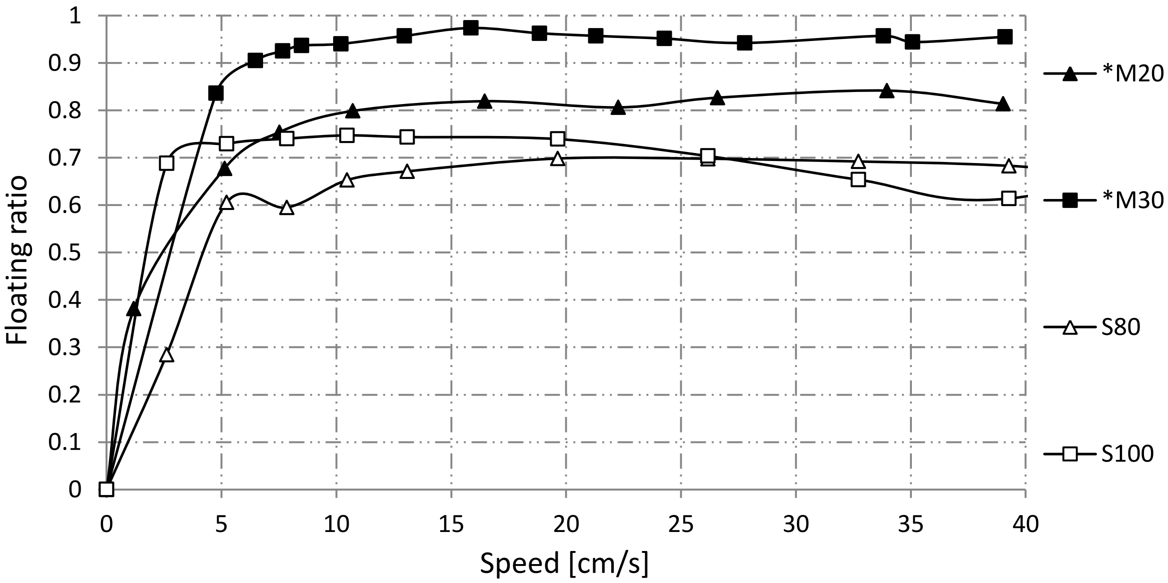

Figure 4-27 High silt content floating ratio comparison, Sassa & Yang
(S80/S100: Rotating drum – Yang; *M20/*M30: Coaxial cylinder – Sassa)

Figure 4-27 shows the comparison of high silt content. The comparison was made within 40cm/s. It indicates Sassa has a better velocity control than Yu. Compared with Figure 4-25, Yu's test program runs the test up to 130cm/s. The velocity is too high for the coaxial cylinder and do not promise a steady flow. The behavior of *M20 and *M30 are considered to be very similar to S80 and S100. Since the measurements of S80 and S100 are from the middle depth of the flow and *M20 and *M30 are the measurements from the base, the lower floating ratio of the S series make a good match with the *Series.

4.6.3. Dissipation comparison

Similarly, the dissipation comparison is also made in four groups. Figure 4-28 shows the low silt content comparison between the S and *S series.

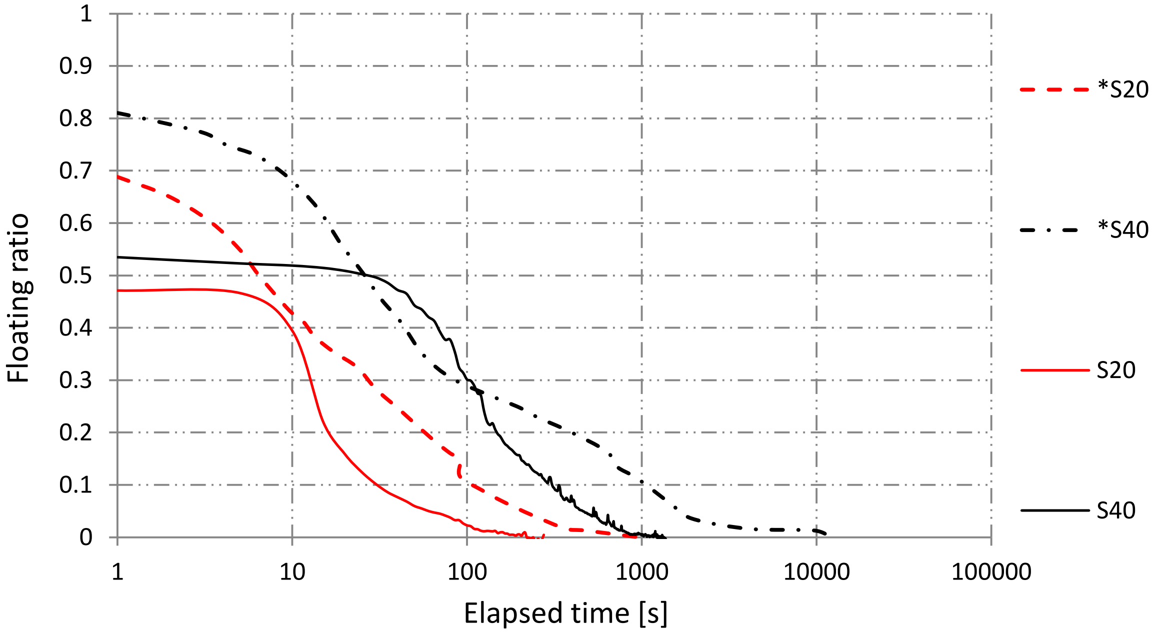

Figure 4-28 Low silt content dissipation comparison, Yang & Yu
(S20/S40: Rotating drum – Yang; *S20/*S40: Coaxial cylinder – Yu)

Since the measurement was taken in the middle part of the flow, the S series starts with a lower floating ratio in the dissipation. Result shows a good match that tests with lower floating ratio end up in a shorter dissipation time. However, the floating ratio does not maintain much in the beginning part of the *S series. Further scrutinizing shows most of the result from *S series do not maintain much. There are two explanations for this.

The first explanation is the experiment of *S series stops the rotating state too quickly, in a way that fastens the initial dissipation. The *S series stops the test out of a sudden, causing great initial disturbance and kind of ‘shaking’ the mixture, that the beginning part of the dissipation is disturbed and fastened. Another explanation may be that the analysis data of *S series has over-removed the inertia disturbance of the raw data. In this scenario, part of the valid data was also removed mistakenly, resulting in less time to maintain the maximum floating ratio.

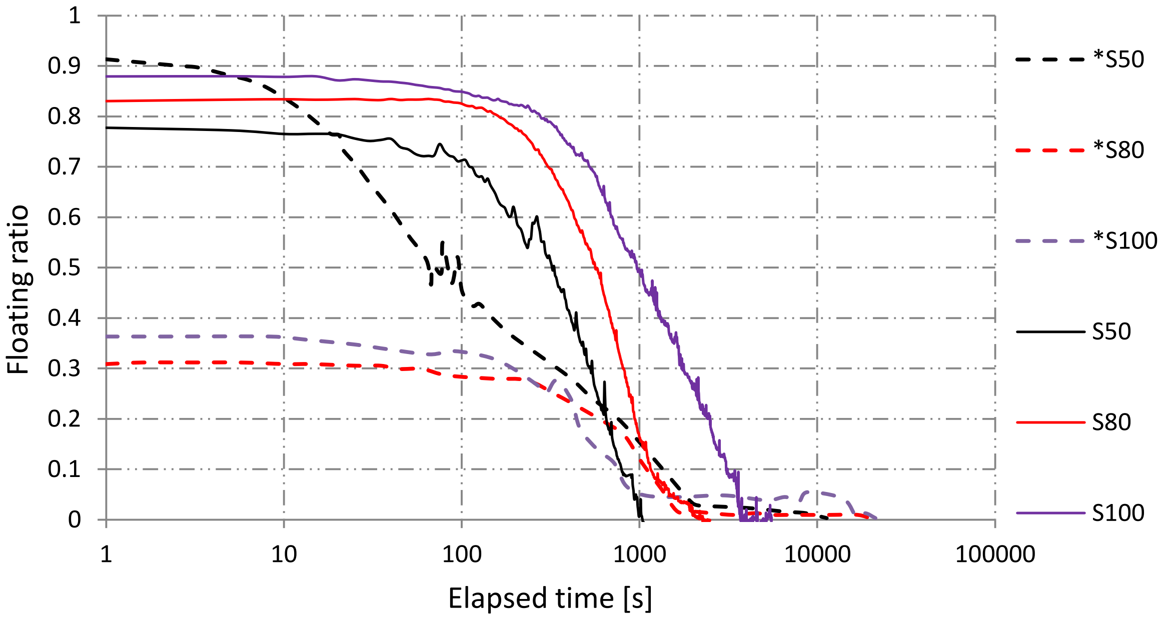

Figure 4-29 High silt content dissipation comparison, Yang & Yu
(S50/S80/S100: Rotating drum – Yang; *S50/*S80/*S100: Coaxial cylinder – Yu)

Figure 4-29 shows the high silt content dissipation comparison with the *S series. Unfortunately the *S80 and *S100 started from false floating ratios (unsteady flow), and results are hard to compare. The *S50 is also in bad quality, with the floating ratio maintaining part ended too quickly.

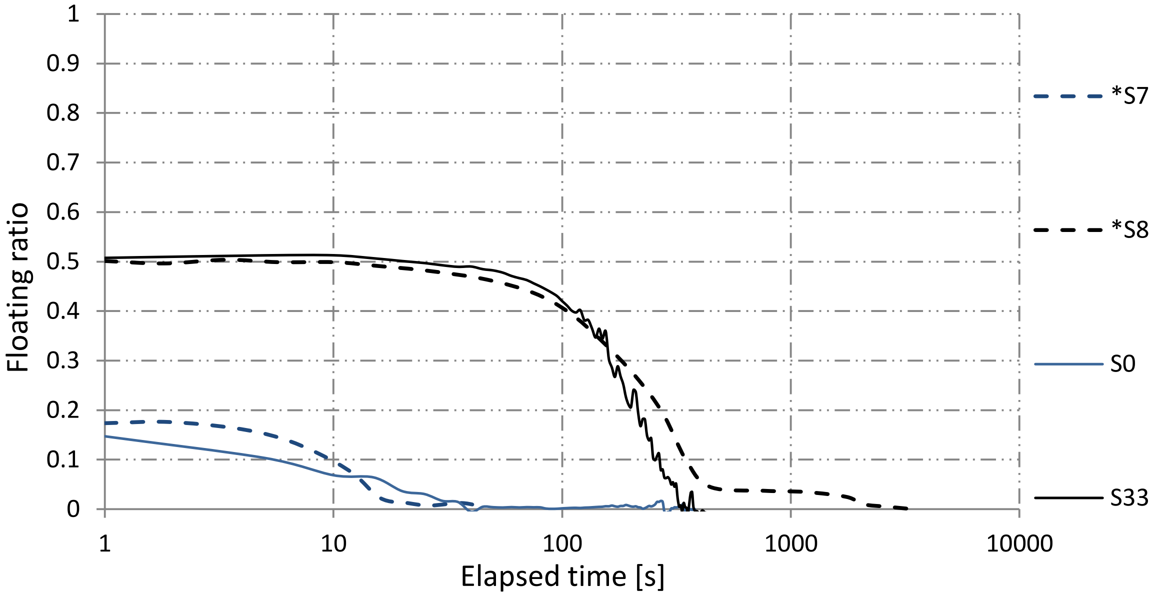

Figure 4-30 Low silt content dissipation comparison, Sassa & Yang
(S0/S33: Rotating drum – Yang; *S7/*S8: Coaxial cylinder – Sassa)

Figure 4-30 shows the low silt content dissipation comparison has a very good match with Sassa’s study. The coarse material S0 and *S7 both finished dissipation in 40~50 seconds, and the finer pairs also share a similar pattern. *S8 has a considerable prolonged part at a very low floating ratio (0~0.1), this part remains to be further scrutinized.

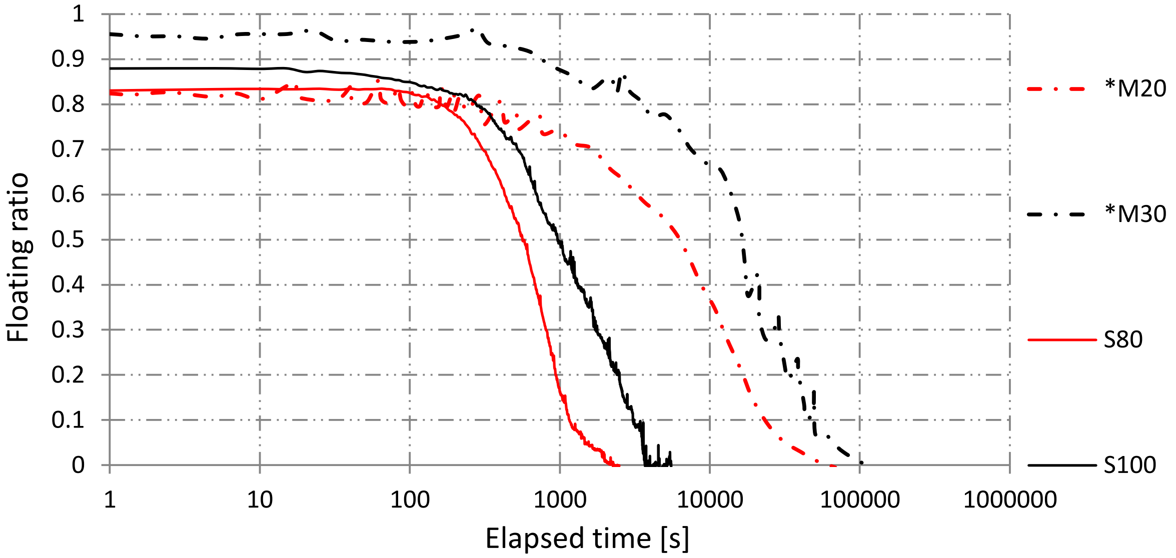

Figure 4-31 High silt content dissipation comparison, Sassa & Yang
(S80/S100: Rotating drum – Yang; *M20/*M30: Coaxial cylinder – Sassa)

Figure 4-31shows the high silt content comparison with Sassa's study. All results show the common situation that these fine-grained materials can maintain a very high floating ratio for over 100 seconds. In addition, the series from Sassa also last for a relatively much longer period. This is because of the higher concentration of the samples and finer grain size distribution. Compared with the low silt content samples, the fine grain is proved to be very considerable in both excess pore pressure generation process and dissipation process.

5. Conclusions and recommendations

The rotating drum apparatus has yield satisfactory results for the aim of this study. Empirical results of the excess pore pressure build-up in samples of different silt content are achieved. Results show the excess pore pressure build-up is closely related to fine-grained content. In the comparison study, most of the results show a very similar pattern with literature studies. The rotating drum apparatus is also proved to be able to provide more steady flow than the coaxial cylinder in relatively high velocity (40~80cm/s).

However, some issues remain to be further securitized with the apparatus. The influence of the disturbance caused by the sensor bar insertion on the debris flow is unclear. The floating ratio calculating is based on the assumption that the flow depth is unchanged during the motion, which should be further corrected if the change of flow depth is considerable.

A list of recommendations is made for the apparatus improvement and debris flow modeling respectively.

For apparatus improvement:

1. A light water-proof cover for the pore pressure sensor wires is suggested to replace the sensor bar. The sensor bar is made to protect the wires from water, but the current size of the bar is too large and cause disturbance to the flow. Alternatively, other pore pressure measurement methods are recommended to use if they bring less disturbance.

2. Laser measurement is suggested to be installed at the channel cross section to measure the flow depth. The result of pure water test performed in this thesis does not prove the flow depth can be neglectable in debris flow simulation. Especially, the flow depth can be changing a lot due to the grading behavior in granular debris flow. Shear stress and normal stress sensor could also be installed together with the laser installation for rheologic study.

3. A torque flange is suggested to be installed between the engine transmission unit and the axis of the rotating drum. This thesis has proved torque value is very hard to derive by indirect measurement.
4. The rim of the transparent part of the apparatus could be softened. Currently the rim is too sharp for manually cleaning of the apparatus.

For debris flow modeling:

1. Measure the pore pressure at different flow depth. It is assumed and to be verified that the floating ratio decreases from the bottom to the flow surface. Additionally, if flow velocity can also be measured, the pore pressure measurement can also be verified with the constitutive equations.
2. Simulate the flow with confined stress (normal stress). It may be possible to simulate this by shaping the flow channel with something inserted into the flow, causing a normal stress due to shape factor. The reason to do this is because in actual event the shear zone is confined by the weight of upper layer material.
3. Evaluate the influence of concentration of the debris flow on the generation of the excess pore pressure. In this thesis, the concentration is taken as 50% which is considered as a common concentration value for debris flow. It may be taken as a variable for further study to study its influence.

Reference

Ashida, K., S. Egashira, H. Kamiya and H. Sasaki (1985). "The friction law and moving velocity of a soil block on slopes." Annals of the Disaster Prevention Research Institute, Kyoto University **28**: 297-307.

Bagnold, R. A. (1954). Experiments on a gravity-free dispersion of large solid spheres in a Newtonian fluid under shear. Proceedings of the Royal Society of London A: Mathematical, Physical and Engineering Sciences, The Royal Society.

Beverage, J. P. and J. K. Culbertson (1964). "Hyperconcentrations of suspended sediment." Journal of the Hydraulics Division **90**(6): 117-128.

Bird, R. B., G. Dai and B. J. Yarusso (1983). "The rheology and flow of viscoplastic materials." Rev. Chem. Eng **1**(1): 1-70.

Coussot, P. and M. Meunier (1996). "Recognition, classification and mechanical description of debris flows." Earth-Science Reviews **40**(3): 209-227.

Cruden, D. and D. Varnes (1996). "Landslides: investigation and Mitigation. Special Report 247." Transportation Research Board, Us National Research Council, chap Landslides Types and Processes: 36-75.

Davies, T. (1986). "Large debris flows: a macro-viscous phenomenon." Acta Mechanica **63**(1-4): 161-178.

Devoli, G. (2013). Debris flow hazard mapping procedures. Seminar in snow, slush- and debris flows: Hazard analysis and protection measures.

Egashira, S. (1997). Constitutive equations of debris flow and their applicability. 1st Int. Conf. on Dbris-Flow Hazards Mitigation, ASCE.

Egashira, S. and K. Ashida (1992). "Unified view of the mechanics of debris flow and bed-load." Advances in micromechanics of granular materials: 391-400.

Egashira, S., K. Ashida, H. Yajima and J. Takahama (1989). "Constitutive equations of debris flow." Annals of the Disaster Prevention Research Institute, Kyoto University **32**(B-2): 487-501.

Guzzetti, F., S. Peruccacci, M. Rossi and C. P. Stark (2008). "The rainfall intensity–duration control of shallow landslides and debris flows: an update." Landslides **5**(1): 3-17.

Highland, L., S. D. Ellen, S. B. Christian and W. M. Brown III (1997). Debris-flow hazards in the United States, US Department of the Interior, US Geological Survey Denver, CO, USA.

Hotta, N. (2011). "Pore water pressure distributions of granular mixture flow in a rotating mill." Debris-Flow Hazards Mitigation: Mechanics, Prediction and Assessment, edited by: Genevois, R., Hamilton, DL, and Prestininzi, A., Casa Editrice Universita La Sapienza, Roma: 319-330.

Hotta, N. and T. Ohta (2000). "Pore-water pressure of debris flows." Physics and Chemistry of the Earth, Part B: Hydrology, Oceans and Atmosphere **25**(4): 381-385.

Hungr, O., S. Evans, M. Bovis and J. Hutchinson (2001). "A review of the classification of landslides of the flow type." Environmental & Engineering Geoscience **7**(3): 221-238.

Hutchinson, G. O. (1988). Hellenistic poetry, Oxford University Press on Demand.

Iverson, R. M. (1997). "The physics of debris flows." Reviews of geophysics **35**(3): 245-296.

Iverson, R. M. (2014). "Debris flows: behaviour and hazard assessment." Geology Today **30**(1): 15-20.

Johnson, A. and J. Rodine (1984). "Debris flow." Slope instability: 257-361.

Julien, P. and J. O'Brien (1997). Selected notes on debris flow dynamics. Recent developments on debris flows, Springer**:** 144-162.

Kaitna, R. and D. Rickenmann (2007). "A new experimental facility for laboratory debris flow investigation." Journal of Hydraulic Research **45**(6): 797-810.

Kaitna, R., D. Rickenmann and M. Schatzmann (2007). "Experimental study on rheologic behaviour of debris flow material." Acta Geotechnica **2**(2): 71-85.

Laache, E. (2016). Effectiveness of Debris Flow Breakers. Master, NTNU.

Leonardi, A. (2015). Numerical simulation of debris flow and interaction between flow and obstacle via DEM, Diss., Eidgenössische Technische Hochschule ETH Zürich, Nr. 22893.

Li, Y., B.-l. Wang, X.-j. Zhou and W.-c. Gou (2015). "Variation in grain size distribution in debris flow." Journal of Mountain Science **12**(3): 682-688.

Mark, D. B., C. L. Nelson, R. M. Califf, F. Harrell, K. L. Lee, R. H. Jones, D. F. Fortin, R. S. Stack, D. D. Glower and L. R. Smith (1994). "Continuing evolution of therapy for coronary artery disease. Initial results from the era of coronary angioplasty." Circulation **89**(5): 2015-2025.

Miyamoto, K. (1985). "Mechanics of grain flows in Newtonian fluid." Ph. D.-thesis presented to Ritsumeikan Univ.

Nettleton, I., S. Martin, S. Hencher and R. Moore (2005). "4 DEBRIS FLOW TYPES AND MECHANISMS."

NIFS. (2014) "Sammenligning av risikoakseptkriterier for skred og flom.".

NVE. (2011). Auka tal jordskred, flaumskred, sørpeskred?

NVE. (2014). Aktsomhetskart for Jord- og Flomskred.

Pierson, T. C. and J. E. Costa (1987). "A rheologic classification of subaerial sediment-water flows." Reviews in Engineering Geology **7**: 1-12.

Schatzmann, M. (2005). Rheometry for large particle fluids and debris flows, Diss., Eidgenössische Technische Hochschule ETH Zürich, Nr. 16093, 2005.

Stiny, J. (1910). Die Muren: Versuch einer Monographie mit besonderer Berücksichtigung der Verhältnisse in den Tiroler Alpen, Wagner.

Takahashi, T. (1981). "Debris flow." Annual review of fluid mechanics **13**(1): 57-77.

Takahashi, T. (2009). "A review of Japanese debris flow research." International Journal of Erosion Control Engineering **2**(1): 1-14.

Takahashi, T. (2014). Debris flow: mechanics, prediction and countermeasures, CRC press.

Taurisano/NVE., A. (2011). Flaumskred, Manndalen i Kåfjord 2010., NVE.

Vegvesen, S. (2014). Håndbok 139.

Wang, G. and K. Sassa (2003). "Pore-pressure generation and movement of rainfall-induced landslides: effects of grain size and fine-particle content." Engineering geology **69**(1): 109-125.

Winter, M., F. Macgregor and L. Shackman (2005). "Scottish road network landslides study summary report."

Yu, X. (2015). Laboratory investigation of the pore pressure built-up in moving debris. Master, NTNU.

Appendix

Appendix 1 - Apparatus comparison

(Rotating drum – Yang; Coaxial cylinder – Sassa (Wang and Sassa 2003); Coaxial cylinder – Yu (Yu 2015))

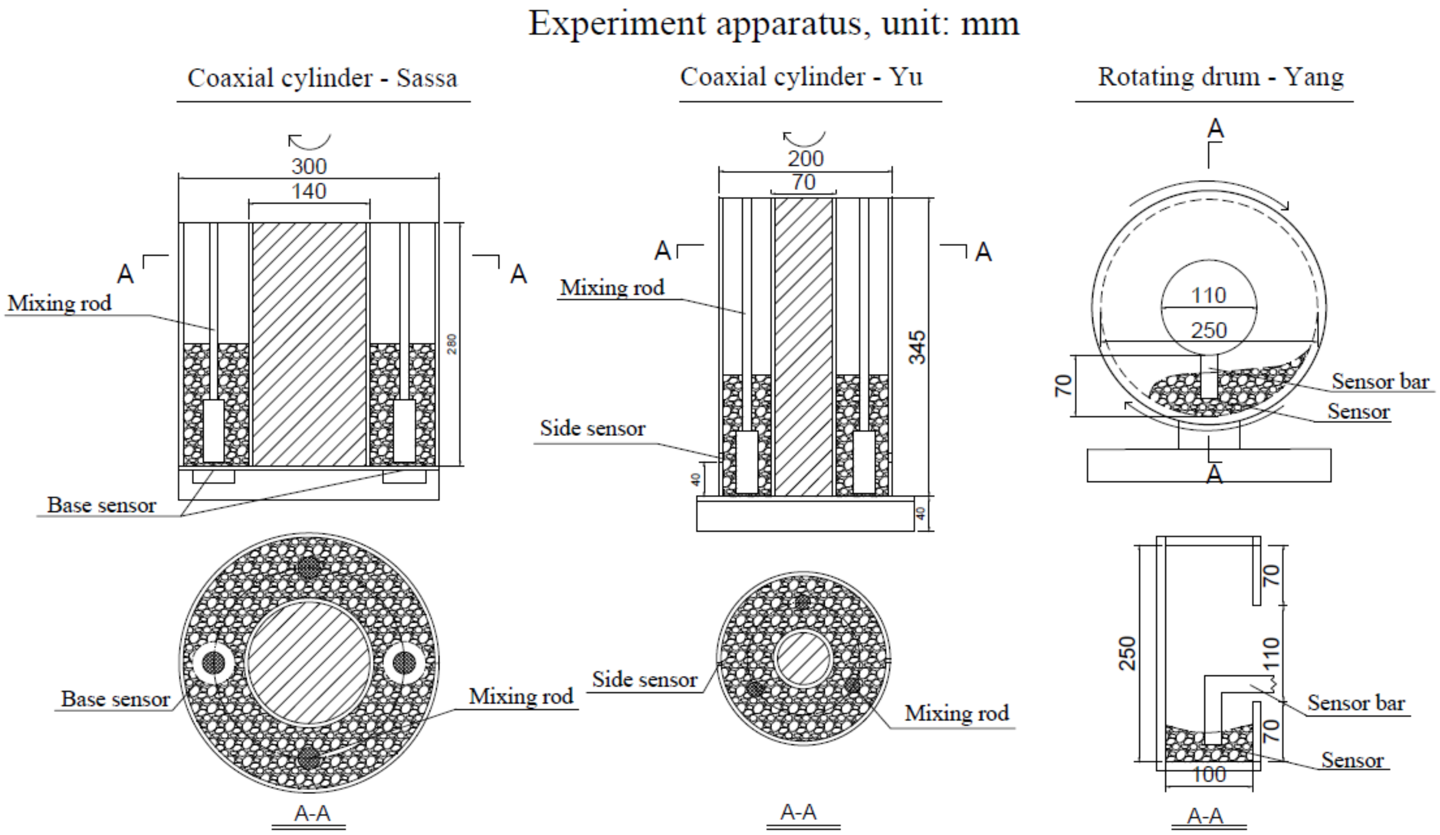

Appendix 2 – Grain size distribution

(S0 - S100: Rotating drum – Yang; *S20 - *S80: Coaxial cylinder – Yu (Yu 2015); *S7/ *S8/ *M10/20/30: Coaxial cylinder- Sassa (Wang and Sassa 2003))

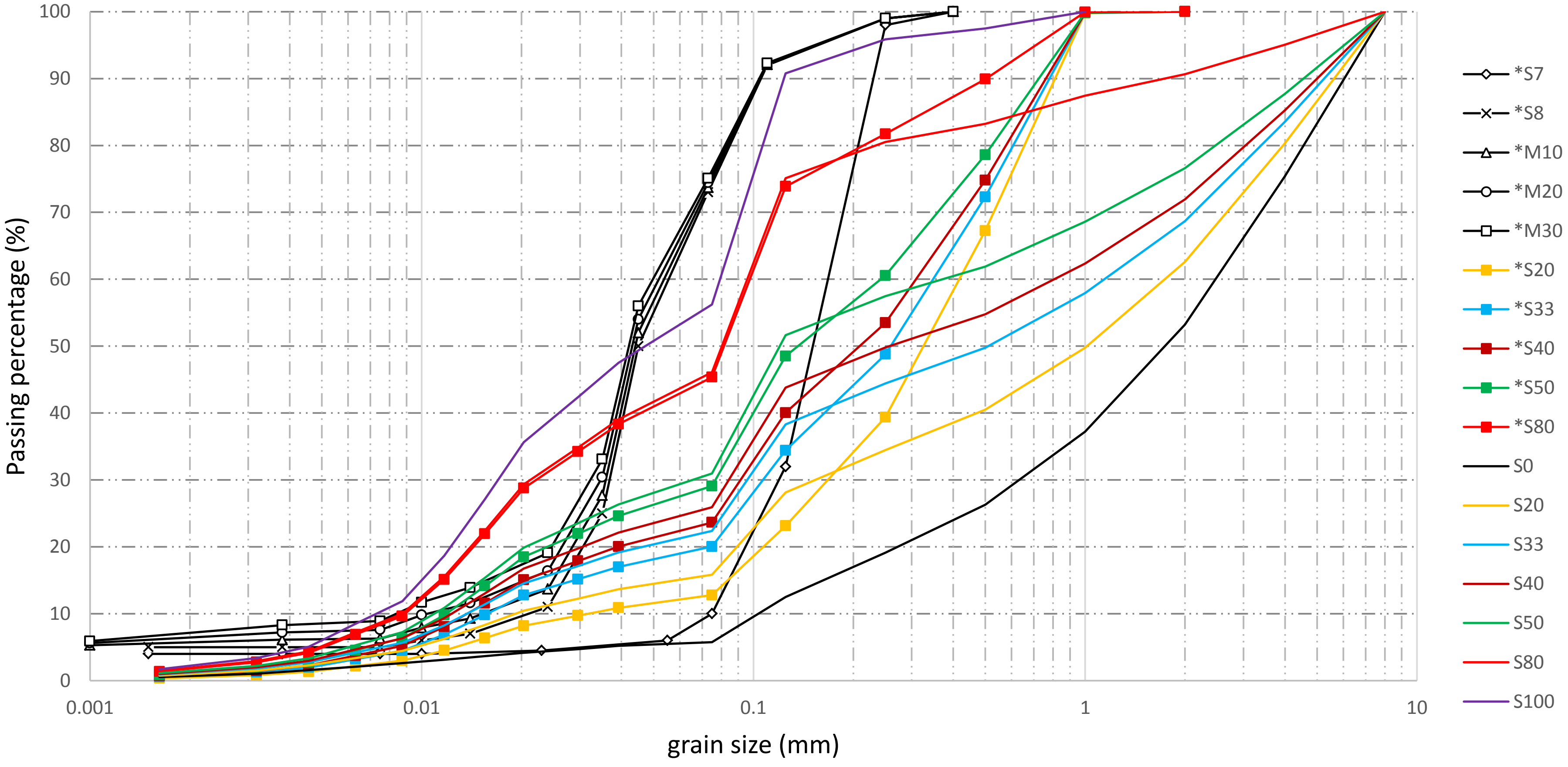

Appendix 3 – Floating ratio

(S0 - S100: Rotating drum – Yang; *S20 - *S100: Coaxial cylinder – Yu (Yu 2015); *S7/ *S8/ *M10/20/30: Coaxial cylinder- Sassa (Wang and Sassa 2003))

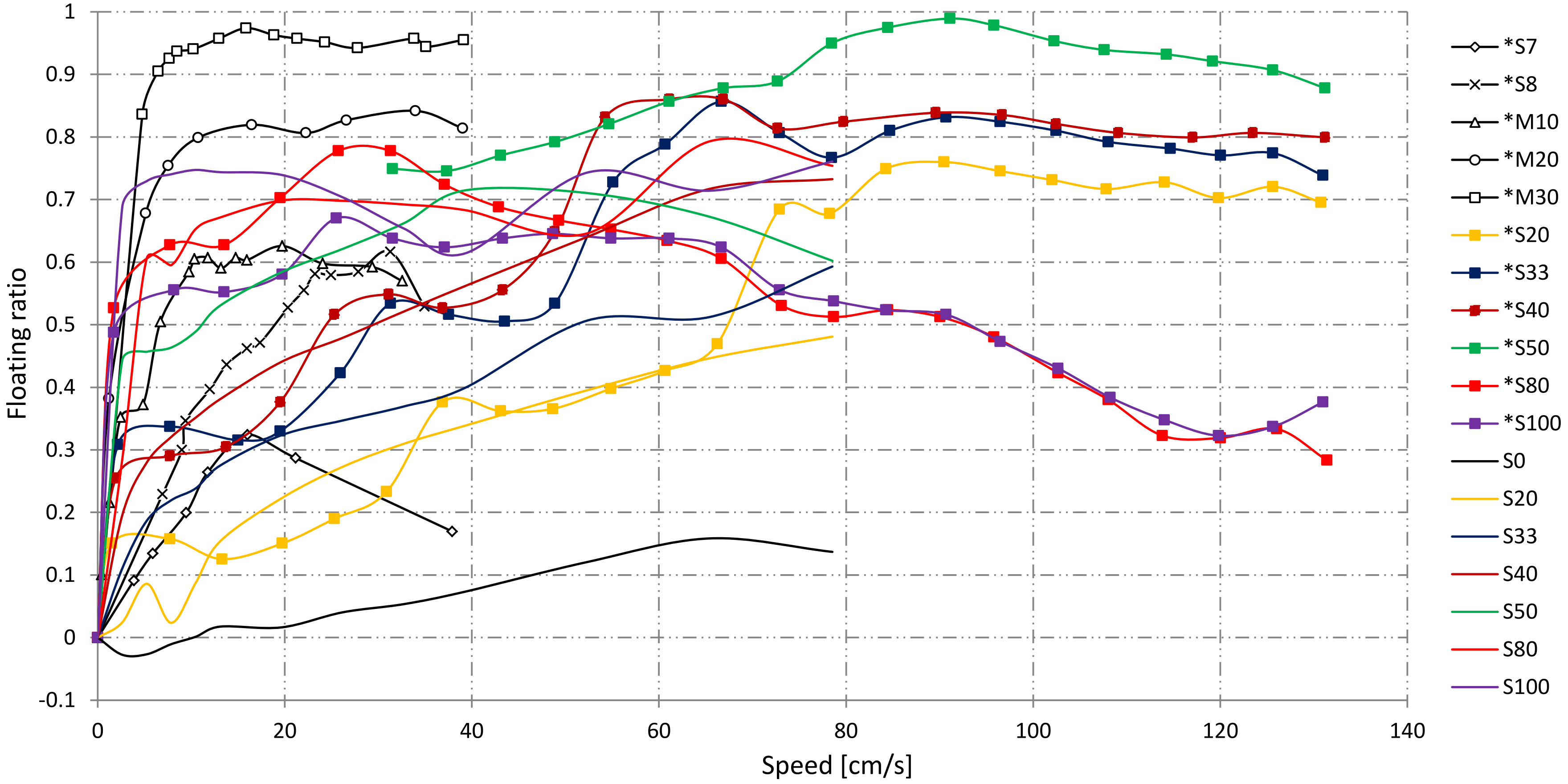

Appendix 4 – Dissipation

(S0 - S100: Rotating drum – Yang; *S20 - *S100: Coaxial cylinder – Yu (Yu 2015); *S7/ *S8/ *M10/20/30: Coaxial cylinder- Sassa (Wang and Sassa 2003))